Nanoscale Modification of Key Surface Parameters to Augment Pool Boiling Heat Transfer and Critical Heat Flux in Water and Dielectric Fluids

by

Eric Christopher Forrest

SUBMITTED TO THE DEPARTMENT OF NUCLEAR SCIENCE AND ENGINEERING IN PARTIAL FULFILLMENT OF THE REQUIREMENTS FOR THE DEGREES OF

BACHELOR OF SCIENCE IN NUCLEAR SCIENCE AND ENGINEERING
and
MASTER OF SCIENCE IN NUCLEAR SCIENCE AND ENGINEERING
AT THE
MASSACHUSETTS INSTITUTE OF TECHNOLOGY

JUNE 2009

Signature of Author:_____
Department of Nuclear Science and Engineering
May 8, 2009

Certified by:_____
Lin-Wen Hu
Associate Director, MIT Nuclear Reactor Laboratory
Thesis Supervisor

Certified by:_____
Jacopo Buongiorno
Associate Professor of Nuclear Science and Engineering
Thesis Supervisor

Accepted by:_____
Jacquelyn C. Yanch
Professor of Nuclear Science and Engineering
Chair, Department Committee on Graduate Students

Nanoscale Modification of Key Surface Parameters to Augment Pool Boiling Heat Transfer and Critical Heat Flux in Water and Dielectric Fluids

by

Eric Christopher Forrest

Submitted to the Department of Nuclear Science and Engineering on May 8, 2009 in partial fulfillment for the requirements of the degrees of

BACHELOR OF SCIENCE and MASTER OF SCIENCE
in NUCLEAR SCIENCE AND ENGINEERING

ABSTRACT

Surface effects on pool boiling heat transfer and the critical heat flux are well documented but poorly understood. This study investigates the pool boiling characteristics of various fluids, and demonstrates that surface effects can drastically alter the nucleate boiling heat transfer coefficient as well as the critical heat flux. Changes in surface morphology and surface chemistry are suspected to be the primary factors influencing pool boiling heat transfer. The relative impact of surface properties is shown to depend strongly upon the working fluid.

To evaluate the effects of chemical constituency and surface texture on the pool boiling of water, nanoparticle thin-film coatings are applied to nickel and stainless steel substrates using the layer-by-layer assembly method. This study shows that such coatings, with thicknesses on the order of one micron or less, are capable of enhancing the critical heat flux of water up to 100%, and enhancing the nucleate boiling heat transfer coefficient over 100%. Through the use of thin-film coatings, the importance of nanoscale surface texture, porosity, and chemical constituency on boiling mechanisms is revealed.

Low surface tension dielectric fluids, including a recently developed fluorinated ketone with a low global warming potential, are tested to determine their pool boiling heat transfer capabilities. The potential for nanoparticle-based pool boiling enhancement in well-wetting dielectric fluids is investigated. The role of surface wettability and adhesion tension on the incipience of boiling, nucleate boiling, and critical heat flux are considered. Results indicate that the low global warming potential fluorinated ketone may be a viable alternative in the cooling of electronic devices. Additionally, results demonstrate that enhancement of boiling heat transfer is possible for well-wetting dielectric fluids, with 40% enhancement in the critical heat flux using dilute suspensions of aluminum or silica nanoparticles in the fluorinated ketone.

THESIS SUPERVISOR: Lin-Wen Hu, Ph.D., PE
TITLE: Associate Director and Principal Research Scientist, MIT Nuclear Reactor Laboratory

THESIS SUPERVISOR: Jacopo Buongiorno, Ph.D.
TITLE: Associate Professor of Nuclear Science and Engineering

ACKNOWLEDGEMENTS

I wish to extend my gratitude and thanks to my thesis supervisor Dr. Lin-Wen Hu for her guidance throughout these projects. I would also like to thank my thesis supervisor Professor Jacopo Buongiorno for his guidance on these projects, and also for his kind advice and support as my advisor during my undergraduate years at the Institute. The time and care invested by my thesis advisors has been greatly appreciated.

I owe my special thanks to Dr. Thomas McKrell for his contributions to these projects, especially with regard to the research in Section II, and to Erik Williamson for his contributions to the research in Section I. Professor M. Rubner of the Department of Materials Science and Engineering, Professor Robert E. Cohen of the Department of Chemical Science and Engineering, and Professor A. Hatton of the Department of Chemical Engineering are kindly recognized for the use of their facilities and equipment. I am also grateful to a number of other people for their advice and input over the years, helping me to hone my experimental and analytical skills. In this regard, I would like to thank Dr. Phil Sharpe, Mr. Mike Curry, Wesley Williams, Hyung Dae Kim, Bao Truong, Craig Gerardi, Sung Joong Kim, and In-Cheol Bang, among others.

ABB Corporate Research is gratefully acknowledged for sponsoring the research in Section II of this thesis. 3M Electronics Markets Materials Division is acknowledged for provided the fluorinated ketone test fluid used in Section II of this study, along with valuable supporting information.

Lastly, I would like to thank my family and friends for their patience and support throughout my years at MIT.

TABLE OF CONTENTS

4. THEORETICAL ASPECTS OF THE EFFECT OF THIN-FILM COATINGS ON NUCLEATE BOILING HEAT TRANSFER AND CRITICAL HEAT FLUX.................. 74
  4.1. Review of Effects of Surface Structure and Chemical Constituency on Wettability.. 74
  4.2. Wettability and Bubble Nucleation.. 76
  4.3. Critical Heat Flux.. 78
    4.3.1. Review of Existing Theories.. 78
    4.3.2. Importance of the Dynamic Receding Contact Angle on CHF 80

>><<<<<<<<<<<<<<<<<<<<<<<<<<<<<<<<<<<<<<<<<<<

SECTION II: NANOPARTICLE-BASED ENHANCEMENT OF POOL BOILING HEAT TRANSFER IN LOW GLOBAL WARMING POTENTIAL DIELECTRIC FLUIDS.. 83
5. BACKGROUND ON LOW GLOBAL WARMING POTENTIAL DIELECTRIC FLUIDS FOR ELECTRONICS COOLING.. 84
  5.1. Two-phase Cooling of Electronic Devices 84
  5.2. Greenhouse Gases and the Kyoto Protocol.. 86
6. PREPARATION OF COLLOIDAL DISPERSIONS IN DIELECTRIC FLUIDS 88
  6.1. Theoretical Aspects of Dispersing and Stabilizing Nanopowders in Liquids 88
  6.2. Colloidal Dispersions of Nanoparticles in a Fluorinated Ketone 90
    6.2.1. SiO_2 Nanoparticles.. 90
    6.2.2. Aluminum Nanoparticles.. 92
7. WIRE BOILING TESTS IN DIELECTRIC FLUIDS.. 94
  7.1. Experimental Apparatus... 94
  7.2. Property Measurements of Pure $C_2F_5C(O)CF(CF_3)_2$.. 96
  7.3. Results of Wire Boiling Experiments 97
    7.3.1. Nickel Wire in Pure FC-72 98
    7.3.2. Nickel Wire in Pure $C_2F_5C(O)CF(CF_3)_2$... 102
    7.3.3. Effect of Dispersant on Boiling Heat Transfer 105
    7.3.4. Nickel Wire in $SiO_2/C_2F_5C(O)CF(CF_3)_2$ Colloid with Dispersant.................. 108
    7.3.5. Nickel Wire in $Al/C_2F_5C(O)CF(CF_3)_2$ Colloid... 111
9. THEORETICAL ASPECTS OF BOILING IN WELL-WETTING DIELECTRIC FLUIDS…... 114
  9.1. Incipience of Boiling... 114
  9.2. Critical Heat Flux.. 115

>><<<<<<<<<<<<<<<<<<<<<<<<<<<<<<<<

LIST OF FIGURES

LIST OF TABLES

NOMENCLATURE

Symbol		Units
A_{121}	Hamaker constant	J
A_s	surface area	m^2
C	constant	-
D	wire diameter	m
D	diffusion coefficient	m^2/sec
D_c	cavity diameter	m
d	particle diameter	m
d_{br}	breakthrough bubble diameter	m
g	gravitational acceleration	m/s^2
h_{eff}	effective heat transfer coefficient	$W/(m^2\ K)$
h_{fg}	heat of vaporization	J/kg
I	current	A
I	scattered intensity	W/St
I_0	nominal intensity	W/St
K	Zuber constant	-
k	Boltzmann constant	J/K
k_{eff}	effective thermal conductivity	W/(m K)
k_f	fluid thermal conductivity	W/(m K)
k_s	solid thermal conductivity	W/(m K)
L	wire length	m

l	separation distance	m
L_c	characteristic length	m
N_A	active nucleation site density	m^{-2}
n	refractive index	-
q''	heat flux	W/m^2
q''_{CHF}	critical heat flux	W/m^2
R	electrical resistance	Ω
R_a	surface roughness	m
R_c	critical bubble radius	m
R^*	dimensionless heater radius	-
r	Wire radius	m
r_c	cavity radius	m
r	roughness factor	-
T	temperature	ºC or K
T_0	nominal temperature	ºC
T_{sat}	saturation temperature	ºC
T_w	wall temperature	ºC
t_0	Critical polymer layer thickness	m
V	volume	m^3
ΔT	temperature difference	ºC
α	temperature coefficient of resistance	K^{-1}
β	dynamic receding contact angle	degrees

γ	groove angle	degrees
γ_{sv}	solid-vapor interfacial tension	N/m
γ_{sl}	solid-liquid interfacial tension	N/m
δ_e	equivalent macrolayer thickness	m
ε	porosity	-
ζ	deviation ratio	-
η	dynamic viscosity	kg/(m sec)
θ	scattered intensity angle	degrees
θ	contact angle, apparent contact angle	degrees
θ_A	static advancing (advanced) contact angle	degrees
θ_{eq}	static equilibrium contact angle	degrees
θ_I	intrinsic contact angle	degrees
θ_R	static receding (receded) contact angle	degrees
κ	hot/dry spot constant	-
λ	wavelength	m
υ_{fg}	liquid-vapor specific volume change	m^3/kg
ρ_f	liquid density	kg/m^3
ρ_g	vapor density	kg/m^3
σ	surface tension	N/m
$\pm\sigma$	uncertainty	-
φ	heater inclination angle	degrees

Abbreviation

Bi	Biot number
CFC	Chlorofluorocarbon
CHF	Critical heat flux
CVD	Chemical vapor deposition
EXPSAM	Exponential sampling
FC	Fluorocarbon
GWP	Global warming potential
HCFC	Hydrochlorofluorocarbon
HFC	Hydrofluorocarbon
HFE	Hydrofluoroether
IGBT	Insulated-Gate bipolar junction transistor
LbL	Layer-by-Layer
PAH	Poly(allylamine) hydrochloride
PTFE	Poly-tetrafluoroethylene
SEM	Scanning electron microscope
SPS	Sodium poly(styrene sulfonate)

1. INTRODUCTION

1.1. Motivation

Pool boiling is characterized by several regimes with distinguishable heat transfer and hydrodynamic properties. Free convection is the primary heat transfer mechanism for surface temperatures just above the saturation temperature of a liquid, prior to boiling incipience. As the surface temperature increase, the onset of nucleate boiling occurs. Nucleate boiling is a very effective heat transfer mechanism due to the high heat transfer associated with the latent heat of vaporization and the increase in convection due to bubble motion. Therefore, it is desirable to operate thermal-fluid systems in the nucleate boiling regime.

Heat transfer systems that operate in the nucleate boiling regime are limited by a critical heat flux (CHF), at which a vapor film envelopes the heated surface, severely inhibiting heat transfer. In film boiling, which results from exceeding the CHF, a thin film of vapor forms at the boiling surface, preventing the re-wetting of the surface. As a result, there is typically very poor heat transfer since the primary modes of heat transfer from the surface are conduction and radiative heat transfer through the vapor. Therefore, at the point of CHF, a surface will undergo a rapid temperature excursion. For many materials, this results in surface failure, or "burn out." It is crucial that systems such as nuclear reactors operate below the critical heat flux, lest a severe accident occur.

Refrigeration units, many power electronic devices, and other systems depend on the high heat transfer coefficient associated with nucleate boiling to operate as designed. Therefore, raising the upper limit of nucleate boiling could allow for higher safety margins, higher rates of heat transfer in existing systems, or a reduction in the size of future systems while maintaining the same heat transfer capability. Buongiorno et al. concluded in their analysis that a 32% increase in CHF would allow for a 20% power density uprate in pressurized water reactors, thereby improving the economics for electricity generation [1].

The nucleate boiling heat transfer coefficient dictates the operational temperature of a boiling surface for a given fluid saturation temperature at a given heat flux. Devices such as power electronics are highly sensitive to slight increases in temperature. It is therefore desirable to increase nucleate boiling heat transfer in two-phase cooling systems to optimize the performance and operating lifetime of such devices. An overreaching goal of thermal-fluid

scientists has been to find a cost-effective means of enhancing CHF and nucleate boiling heat transfer.

Studies in two-phase heat transfer over the past several years indicate that the addition of nano-sized (1 nm-100 nm) particles to base fluids can dramatically increase CHF and alter other boiling parameters such as nucleation site density, bubble diameter, bubble departure frequency, and so forth. These "nanofluids," as they are referred to in the literature [2], consist of particles such as metal oxides, metals, or allotropes of carbon added to base fluids such as water. Kim et al. summarize findings from various nanofluid boiling experiments, describing that nanofluids can achieve up to 200% enhancement in CHF for pool boiling, and that CHF enhancement occurs at very low loadings (≤0.1% by volume) [3]. For the heat transfer coefficient, some studies report enhancement, some deterioration, and some no change for boiling in dilute nanofluids [3]. Characterization of these dilute nanofluids shows insignificant changes in fluid properties such as thermal conductivity, viscosity, etc. Kim et al. report that boiling in nanofluids deposits a porous coating of nanoparticles upon heater surfaces, increasing surface wettability and resulting in CHF enhancement [4]. Changes in the boiling behavior for dilute nanofluids can therefore be attributed to surface modification imputed by nanoparticle deposition.

Modifying surfaces to augment boiling heat transfer and CHF is not a new concept. In 1962, Berenson observed that increasing surface roughness affects nucleate boiling heat transfer, enhancing the heat transfer coefficient up to 500%-600% [5]. Webb summarizes a number of surface treatments explored from 1931 onward, including mechanical treatments to increase surface roughness along with coatings to alter surface morphology [6]. Webb also states that very porous surfaces show enhancement of CHF. Hwang and Kaviany have demonstrated increases in CHF up to 96% for pool boiling of n-pentane using thin, uniform microparticle coatings on heater surfaces [7]. Kim et al. have reported enhancement for both nucleate boiling heat transfer and CHF in FC-72 using microparticle coatings on wires [8].

Despite in depth investigations of pool boiling heat transfer and CHF over the past seventy years, there is still considerable debate over what causes the boiling crisis and what parameters have the greatest influence upon it. Although Berenson notes in his 1962 paper that the addition of wetting agents to fluids has some effect on critical heat flux, he concludes that, "The maximum nucleate-boiling burnout heat flux is essentially independent of surface material,

roughness and cleanliness [5].” The recent studies in boiling using nanofluids, which show that porous deposits of nanoparticles result in significant CHF enhancement, seem to provide irrefutable proof that surface characteristics have a direct effect on CHF. Investigation into the specific surface parameters that affect CHF and nucleate boiling heat transfer will help reveal the physical mechanisms and reveal optimal means of enhancement in a wide range of applications.

Although various methods have been tested for modifying boiling surfaces over the years, one should note that the predominant focus has been on *microscale* modification of surface parameters. The recent work in the field of nanofluids has led to an interest in the *nanoscale* modification of surfaces and its effect on nucleate boiling heat transfer and CHF. Boiling deposition of nanoparticles on surfaces has been proven to enhance CHF, but the predominant focus has been with water as the working fluid. This work comprises two independent studies, the results of which provide insight into the general mechanisms of boiling heat transfer. Nanoparticle thin-film coatings applied to boiling surfaces are investigated for the development of carefully engineered surfaces with water as the working fluid. Boiling deposition of nanoparticles is investigated in non-aqueous systems, specifically, to determine the potential for nanoparticle-based surface enhancement in well-wetting dielectric fluids.

1.2. Objectives

1.2.1. Nanoparticle Thin-Film Coatings for Pool Boiling Heat Transfer Enhancement

Nanoparticle thin-film coatings applied to boiling surfaces offer a means to carefully control parameters such as wettability, while introducing additional effects such as porosity. The thin-film thicknesses are typically on the order of one micron or less, thereby introducing minimal thermal resistance. This study investigates the heat transfer properties of various polymer/SiO_2 thin-films applied to nickel wires for saturated pool boiling in water at atmospheric pressure. The objective is to obtain pool boiling curves for wires coated with these thin-films, and compare the relative enhancement in heat transfer, if any, to bare wire cases. Relative changes in both the nucleate boiling heat transfer coefficient and critical heat flux are examined. The objective of this study is to demonstrate the performance of thin-film coatings in boiling heat transfer applications for two-phase water systems, and interpret from this the general mechanisms which affect nucleate boiling heat transfer and CHF.

1.2.2. Nanoparticle-Based Enhancement of Pool Boiling Heat Transfer in Low Global Warming Potential Dielectric Fluids

The objective of this study is to investigate a new low global warming potential fluorinated ketone, $C_2F_5C(O)CF(CF_3)_2$, for the two-phase cooling of high power density electronics, and determine whether nanoparticle-based surface enhancement is applicable to the fluid. First, the study compares the pool boiling heat transfer properties of the fluorinated ketone to the perfluorocarbon FC-72, a fluid widely used in electronics cooling. Next, the feasibility of dispersing silica and aluminum nanoparticles in the fluorinated ketone for boiling deposition of nanoparticles is explored using various techniques. Lastly, boiling tests are conducted using the nanoparticle/fluorinated ketone dispersions to assess the enhancement in nucleate boiling heat transfer and CHF achieved with the fluid for such a method. The results of these tests using the fluorinated ketone are important in understanding effects of surface parameters on boiling heat transfer, since boiling interactions are largely dependent on the fluid/surface combination.

SECTION I:
NANOPARTICLE THIN-FILM COATINGS FOR POOL BOILING HEAT TRANSFER ENHANCEMENT

2. PREPARATION OF NANOPARTICLE THIN-FILM COATINGS

2.1. Background on Nanoparticle Thin-film Coatings

Nanoparticle thin-film coatings have been developed and utilized in the fields of materials science and chemical engineering for several decades. Thin-film coatings offer a means to alter optical and wetting properties of surfaces without adding any appreciable thickness to the substrate. Layer-by-layer (LbL) deposition offers a simple means of applying conformal thin-film coatings to many substrates. The LbL method is an aqueous chemical method that involves adhesion and adsorption of subsequent layers onto a surface by alternating the charge of the deposited particles. Iler presented the layer-by-layer deposition method in 1966 as a means of forming thin-films of inorganic colloidal particles on glass substrates [9]. Through pH adjustment, Iler was able to prepare aqueous dispersions of cationic alumina and anionic silica. By immersing his glass substrate in one dispersion following the other, Iler was able to build multilayers of silica and alumina on the surface. Iler noted that the resulting coatings altered the optical and wetting characteristics of the original glass substrate.

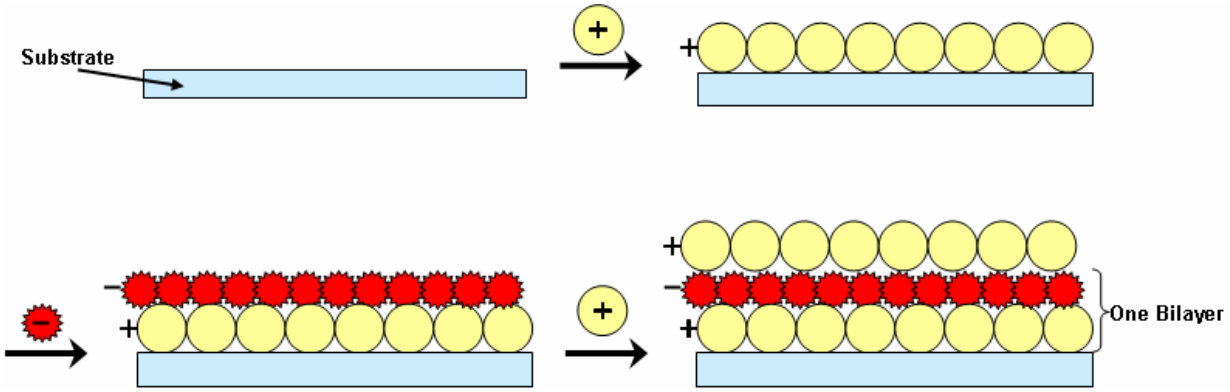

Figure 1: Layer-by-layer Assembly Method for Constructing Thin-film Coatings. Species of alternating charge adsorb onto the surface, with the process repeated until the desired number of bilayers is reached.

Decher and Hong later demonstrated the ability to construct multilayer using charged polymers [10]. More recently, Lee et al. have demonstrated the ability to construct nanoparticle thin-film coatings of carefully controlled thickness and composition by changing deposition conditions such as pH [11, 12, 13]. Figure 1 shows the general assembly process by which multilayers are constructed on a surface. The deposited bilayers can consist of nanoparticle-

nanoparticle, polymer-polymer, or nanoparticle-polymer bilayers. Therefore, a wide range of coatings may be developed. Film thickness, porosity, texture, chemical constituency, and to some degree roughness may be carefully controlled through the use of thin-film coatings. Therefore, optical properties such as refractive index and reflectivity, along with properties such as wettability, may be altered by application of thin-film coatings. Table 1 summarizes various types of thin-film coatings found in literature that have been prepared using the LbL method.

Table 1: Summary of Various Thin-film Coatings Investigated in the Literature[†]

Ref	Subst.	Adhesion Layer	Cationic Species	Anionic Species	Additional Treatment	Film Thickness	Effect on Wettability	Intended Application
[9]	Glass	-	γ-AlO(OH) Fibrils (5-6 nm)	SiO_2 particles (70 nm)	-	425 nm (5 bilayers)	Increase (hydrophilic)	Analytical Techniques
[11] [12]	Glass, Silicon	-	TiO_2 particles (7 nm)	SiO_2 particles (22 nm)	Calcination at 550 ºC	2 nm- 30 nm *per bilayer* (depends on assembly conditions)	Increase (hydrophilic)	Anti-reflection, Anti-fogging, Self-cleaning
[13]	Glass, Silicon	Five bilayers PAH/PSS	AP-SiO_2 particles (16 nm)	SiO_2 particles (8-24 nm)	-	~15 nm *per bilayer* (depends on assembly conditions)	Increase (hydrophilic)	Analytical Techniques
[14]	Glass, Silicon	PAH/SPS or PAH/PAA	PAH	SiO_2 particles (7 nm)	Calcination at 500 ºC	~150 nm (20 bilayers)	Increase (hydrophilic)	Anti-reflection, Anti-fogging
[15]	Glass, Silicon	PAH/SPS	PAH	SiO_2 particles (50/20nm + 20nm)	Calcination at 550 ºC; CVD of fluorosilane	28 nm *per bilayer*	Decrease (hydrophobic)	Anti-reflection, Water-repellant
[16]	Glass, Silicon	-	PAH	PAA, SiO_2	Low pH bath; 180 ºC cross-linking; CVD of fluorosilane; micro-pipette FITC-PAH	N/A	Hydrophilic patterns on hydrophobic surface	Patterned surfaces, Planar microcanals

[†]PAA=poly(acrylic) acid; PAH=poly(allylamine) hydrochloride; SPS=poly(styrene sulfonate); CVD=chemical vapor deposition; Fluorosilane=1H,1H,2H,2H-perfluorodecyltriethoxysilane; AP=3-Aminopropyl-functionalized; FITC-PAH=poly(fluorescein isothiocyanate allylamine hydrochloride). "Analytical techniques" refers to any application used for further study of surface adsorption phenomenon and assembly conditions.

(a) **(b)**

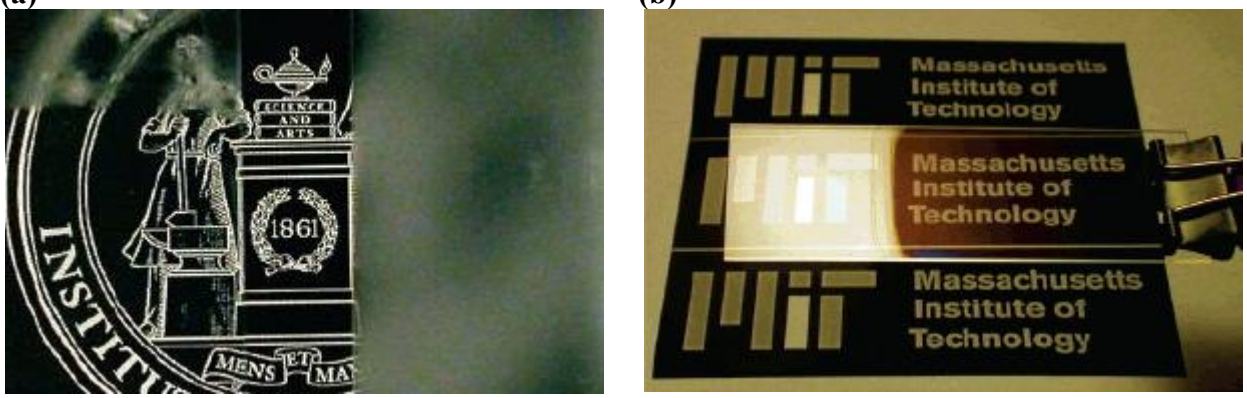

Figure 2: (a) Anti-fog Properties of a TiO_2/SiO_2 Thin-film Coating. The lower portion of the glass slide on the left is coated, whereas the slide on the right is not coated. The anti-fogging property results from the coating having a higher wettability than the untreated glass. (b) Anti-reflective properties of a TiO_2/SiO_2 Thin-film Coating. The left side of the glass slide is not coated, whereas the right side is coated. ***Source: Ref. [11], reproduced with permission of the American Chemical Society, © 2006.***

Current applications of thin-film coatings are primarily focused on creating anti-fog, anti-reflection, and self-cleaning coatings [14]. Glass windshields on automobiles, windscreens on planes, and optics in lasers, cameras, and other sensitive equipment could all benefit from the anti-fog and anti-reflection properties afforded by certain thin-film coatings. Hydrophobic coatings have applications for water-repellant surfaces, anti-fouling surfaces, microfluidic channels, and biosensors [17]. Figure 2a shows anti-fogging properties attained on a glass slide using a TiO_2/SiO_2 thin-film coating. Figure 2b illustrates the anti-reflection properties achieved with the same TiO_2/SiO_2 coating.

Considering that prior studies in boiling have demonstrated the importance of surface chemistry, texture, and wettability and their effect on the nucleate boiling heat transfer coefficient and CHF, nanoparticle thin-film coatings offer a means to develop optimal surface characteristics for boiling heat transfer. By carefully controlling surface conditions, such coatings can help aid in understanding the mechanisms that affect nucleation and CHF. This study investigates the effect of surface parameters on pool boiling in de-ionized water through the use of nanoparticle thin-film coatings consisting of SiO_2/polymer bilayers. Application of these coatings to A286 stainless steel plates in addition to nickel wires allows for investigation into the general adhesion characteristics of these coatings on metal substrates and better characterization of their properties. With the SiO_2/polymer coatings, the effects of film thickness

and wettability on the boiling heat transfer are investigated by carefully controlling these properties.

2.2. Preparation of Solutions and Nanoparticle Colloidal Dispersions

Three varieties of thin-film coatings were prepared using the LbL assembly, following a procedure similar to that used by Bravo et al. [15]. The prepared coatings will be described as hydrophilic (sessile water drop contact angle <90º), superhydrophilic (sessile water drop contact angle ≤3º), or hydrophobic (sessile water drop contact angle >90º). The assembly process for all three coating types required aqueous solutions of sodium poly(styrene sulfonate) (SPS, nominal M_n=70,000 g/mol) and poly(allylamine) hydrochloride (PAH, nominal M_n=70,000 g/mol) and a silica nanoparticle dispersion. One solution of PAH was prepared to a concentration of 10 mM (on a repeat-unit basis) by carefully weighing out 0.4685 g of granular PAH chips and adding them to 500 mL of ultra-pure de-ionized water (>18.2MΩ, Millipore Milli-Q). The PAH was dissolved using a magnetic stirrer. The resulting pH of the PAH solution was acidic, and was reduced further to a pH of 4.00 by titrating with 1 M aqueous hydrochloric acid. A second solution of 10 mM PAH was prepared by adding 0.4685 g of PAH to 500 mL of de-ionized water. The solution was titrated to pH 7.50 using 1 M aqueous sodium hydroxide. A 10 mM solution of SPS was prepared by weighing out 2.062 g of SPS powder and adding to 500 mL de-ionized water. The SPS solution was titrated to pH 4.00 by using 1 M aqueous hydrochloric acid. Lastly, a silica nanoparticle dispersion was prepared by first adding 0.1 M NaCl to pH 9.00 buffer solution and then adding 0.03 wt.% of both 24 nm silica particles (Ludox TM-40) and 50nm silica particles (Polysciences microspheres).

2.3. Application and Processing of Thin-film Coatings

Thin-film coatings were applied to nickel wires (99.98% pure, metals basis) and flat plates made of A286 stainless steel. Prior to the coating process, substrates were aggressively cleaned by sonicating in acetone to remove any dirt, grease, or other materials that could interfere with adhesion of the thin-film coatings. To ensure uniform adsorption and assembly of subsequent layers, five bilayers of PAH (pH 4.00)/SPS (pH 4.00) were deposited on the nickel wire and stainless steel substrates using the layer-by-layer assembly process. These five bilayers of PAH/SPS serve as an adhesion layer, assuring that subsequent layers deposited in the LbL

process adsorb uniformly and adhere properly. The adhesion layer also ensures that aside from roughness, the coating will not be impacted by the substrate used. The deposition process involved immersion into the 10 mM PAH solution (pH 4.00), followed by several rinses in ultra-pure de-ionized water, and then immersion into the 10 mM SPS solution (pH 4.00), followed by several more rinses in de-ionized water. The process was then repeated five times. Figure 3 illustrates the technique used to apply the adhesion sublayers for the thin-film coating, where the PAH (pH 4.00) serves as the cationic species, and the SPS (pH 4.00) serves as the anionic species.

To facilitate the coating process, a Zeiss HMS Programmable Slide Stainer, shown in Figure 4, was used to immerse the nickel and stainless steel substrates in the solutions and rinse baths. The dipper enabled automation of the layer-by-layer assembly process so that the substrates did not have to be moved manually. To deposit the adhesion layers and subsequent PAH/SiO_2 bilayers, the automated dipper immersed the substrates in each solution for ten minutes, with immersion in three rinse baths between each coating. During the application process, substrates were electrically isolated from dissimilar metals to avoid galvanic effects which could potentially interfere with the layer-by-layer assembly.

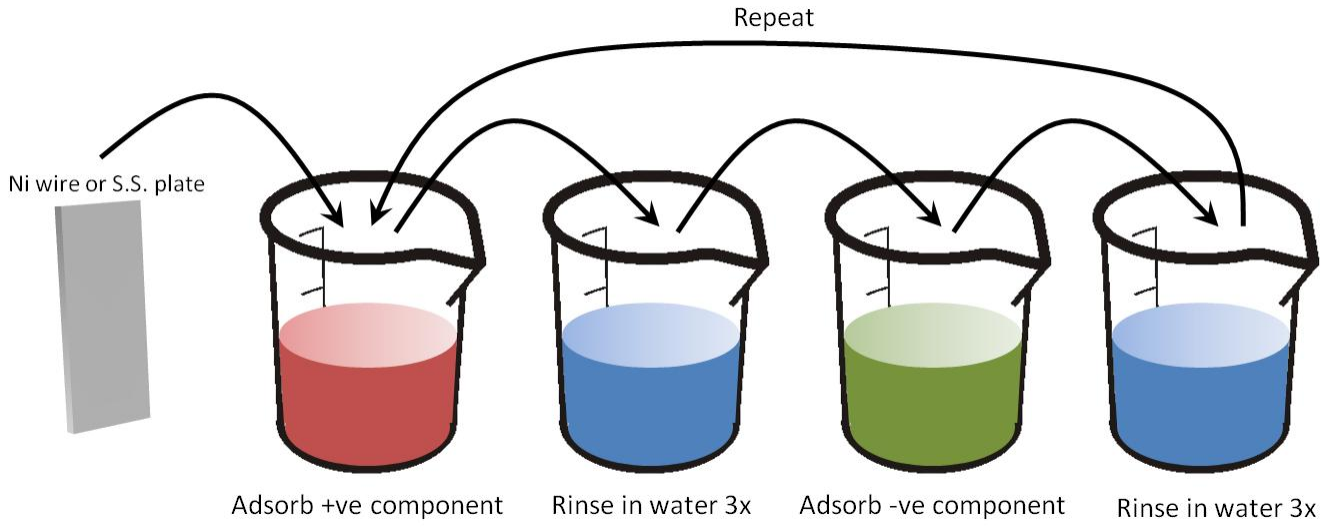

Figure 3: Layer-by-layer Process for Assembling Adhesion Sublayers and Subsequent PAH/SiO_2 bilayers. For the five adhesion bilayers, PAH (pH 4.00) serves as the cationic species and SPS (pH 4.00) serves as the anionic species. For subsequent bilayers, PAH (pH 7.50) serves as the cationic species and SiO_2 (pH 9.00) serves as the anionic species. ***Illustration courtesy of Erik Williamson*.**

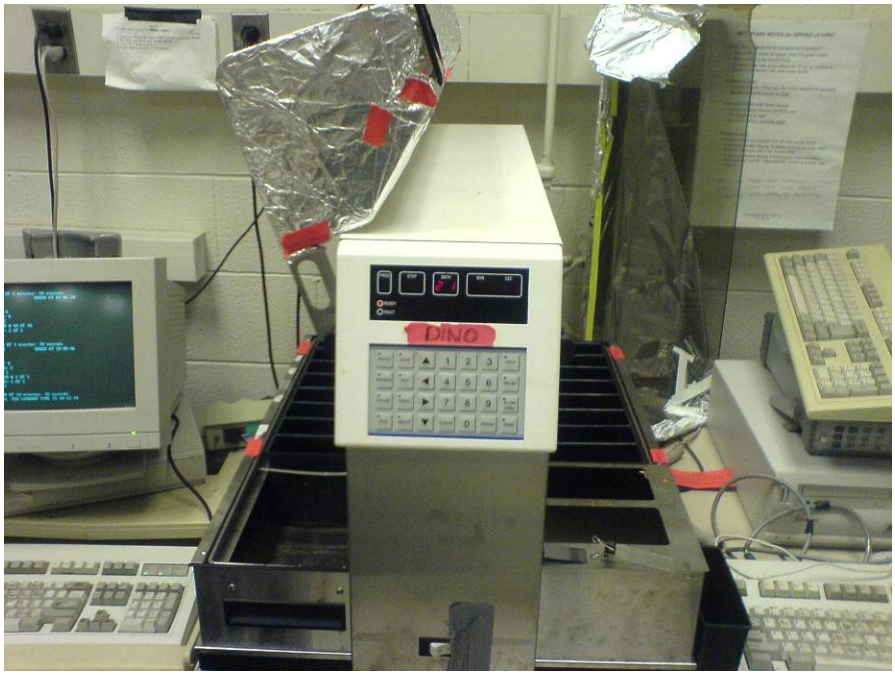

Figure 4: Zeiss HMS Programmable Slide Stainer. The dipper allowed automation of the coating process, which was especially helpful since application of 5 adhesion bilayers + 40 PAH/SiO_2 bilayers takes over 24 hours. The substrates, attached to a mechanical arm, were immersed into the black bins which contained the prepared solutions and rinse water.

2.3.1. Hydrophilic Coatings

Hydrophilic coatings were prepared on nickel wires and stainless steel plates by first applying the five PAH (pH 4.00)/SPS (pH 4.00) adhesion bilayers described above. Following application of the adhesion bilayers and three hours of drying in air, the substrates were immersed in the other PAH solution (pH 7.50), followed by three rinses in de-ionized water, and then immersed in the colloidal dispersion of SiO_2 nanoparticles (pH 9.00), followed by three more rinses. For these bilayers, the PAH (pH 7.50) acts as the cationic species, and the silica nanoparticles act as the anionic species. Immersion in the PAH (7.50) and SiO_2 baths was repeated until the desired number of bilayers was deposited on the substrates. After the layer-by-layer assembly process was complete, the substrates were allowed to dry overnight. Between ten and forty bilayers of PAH/SiO_2 were deposited on the nickel wires and stainless steel plates, depending on the desired coating thickness. Figure 5 illustrates the resulting components of the hydrophilic coating.

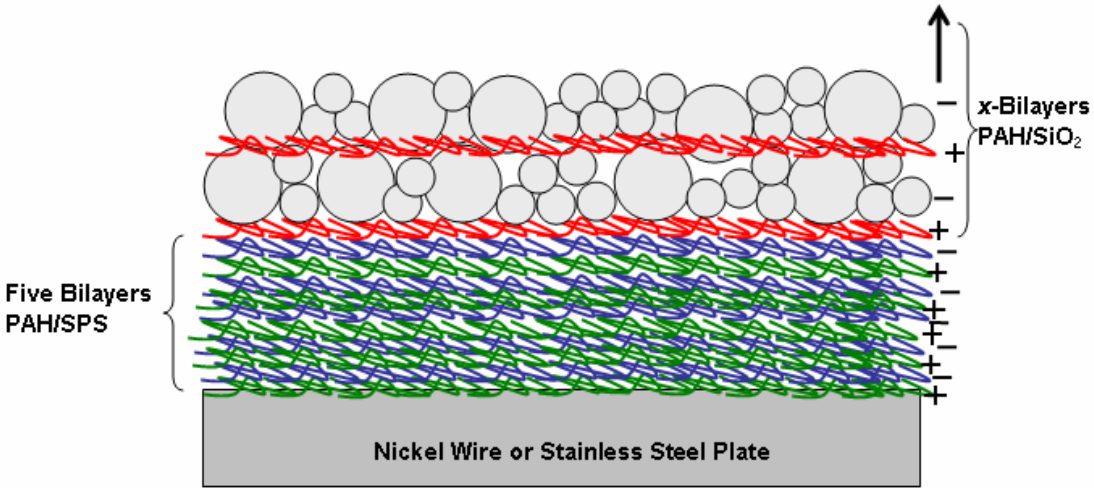

Figure 5: Sketch of a Hydrophilic Thin-Film Coating Applied to Nickel Wires and Stainless Steel Plates. The adhesion layer is made up of PAH (pH 4.00) indicated in green, and SPS (pH 4.00), indicated in blue. The body layers consist of PAH (pH=7.00), indicated by red, and silica nanoparticles (50 nm + 20 nm). Note that the size of the layers is not to scale.

The hydrophilic coatings applied to nickel wires and stainless steel plates withstood regular handling, and in the case of the wires, substantial bending and flexing. Following regular handling and testing, SEM imaging indicated that coatings remained intact and uniformly adhered to the substrate (see section 3.3.4). However, the coatings could be removed by wiping with ethanol or by rubbing the surfaces aggressively. Although the adhesion and durability of the hydrophilic coatings was adequate for conducting pool boiling tests, their use in industrial applications could be precluded without additional treatments for improving their adhesion and integrity.

2.3.2. Superhydrophilic Coatings

Superhydrophilic coatings were prepared in the exact same manner as described for the hydrophilic coatings in section 2.3.1, with one additional treatment. After drying overnight, the nickel wires and stainless steel plates with hydrophilic coatings were calcinated at 550 ºC for four hours in a furnace, making the surfaces superhydrophilic. It should be noted that superhydrophilicity is typically defined as a water droplet having a contact angle of 5º or less within 0.5 seconds of contacting the surface [14]. To simplify discussion of the results, the definition here will be loosened to include surfaces with water droplet contact angles less than 15º after 0.5 seconds and virtually zero degree contact angle after several seconds.

The calcination removes the polymeric components from the coating, leaving behind only a SiO_2 nanoparticle matrix. Figure 6 illustrates the resulting components of the superhydrophilic coating. The calcination also serves to increase the coating's durability, effectively sintering the nanoparticles to each other and the substrate. What remains is a mechanically durable coating with good adhesion, which, according to Cebeci, survives aggressive rubbing and easily passes a standard scotch tape peel test on glass substrates [14]. The superhydrophilic coatings are also expected to have nearly the same thickness as hydrophilic coatings with an equivalent number of PAH/SiO_2 bilayers, since the adhesion sublayers and PAH monolayers have negligible thickness compared to the nanoparticle monolayers [15].

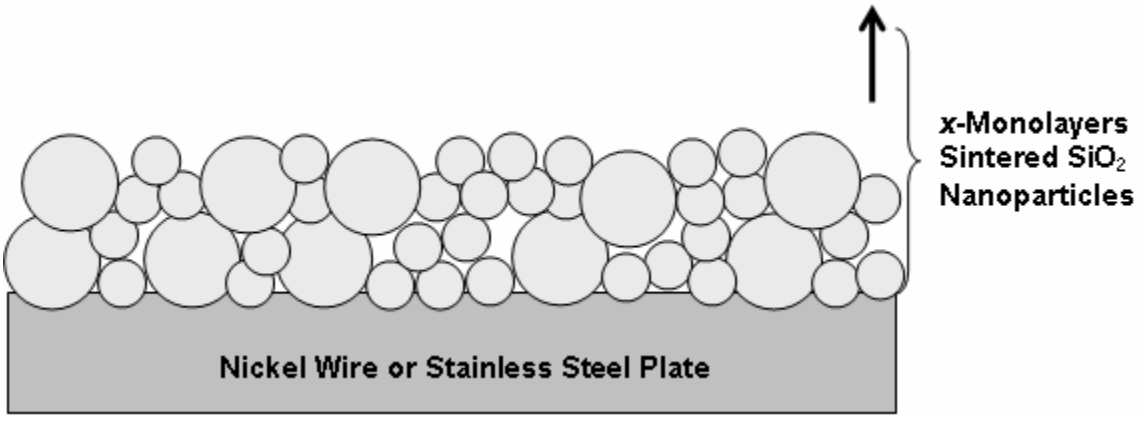

Figure 6: Sketch of a Superhydrophilic Thin-film Coating Applied to Nickel Wires and Stainless Steel Plates. The superhydrophilic coating is a hydrophilic coating that has been calcinated at 550 ºC, removing the polymeric components, including the adhesion sublayers.

2.3.3. Hydrophobic Coatings

Hydrophobic coatings were prepared on nickel wires and stainless steel plates in the exact same manner as described for the Superhydrophilic coatings in section 2.3.2, with one more additional treatment. After applying the PAH/SPS adhesion sublayers, the PAH/SiO_2 bilayers, and calcinating at 550 ºC, the nickel and stainless steel samples were treated with 1H,1H,2H,2H-perfluorodecyltriethoxysilane (fluorosilane, Alfa-Aesar) via chemical vapor deposition (CVD). For the chemical vapor deposition process, nickel wires and stainless steel plates with calcinated PAH/SiO_2 coatings were placed in a poly-tetrafluoroethylene (PTFE)

container with an open vial of fluorosilane. A PTFE container was used to ensure that no moisture would remain after adequate drying, since moisture can interfere with the CVD process. The PTFE container was closed and placed in a 140 ºC oven for 30 minutes. Fluorosilane has a nominal boiling point between 103 ºC and 106 ºC [18], so placement in the oven vaporized the fluorosilane, allowing it to deposit on the calcinated coating. After standing overnight, the resulting coating exhibited hydrophobicity. Figure 7 illustrates the components of the hydrophobic coating. Although the other organic components and SiO_2 particles in the coating deposit uniformly in monolayers, the fluorosilane may deposit in multiple layers since the process is not controlled by surface charge. However, the overall thickness of the fluorosilane layer(s) is still expected to be negligible when compared to the SiO_2 nanoparticle layers.

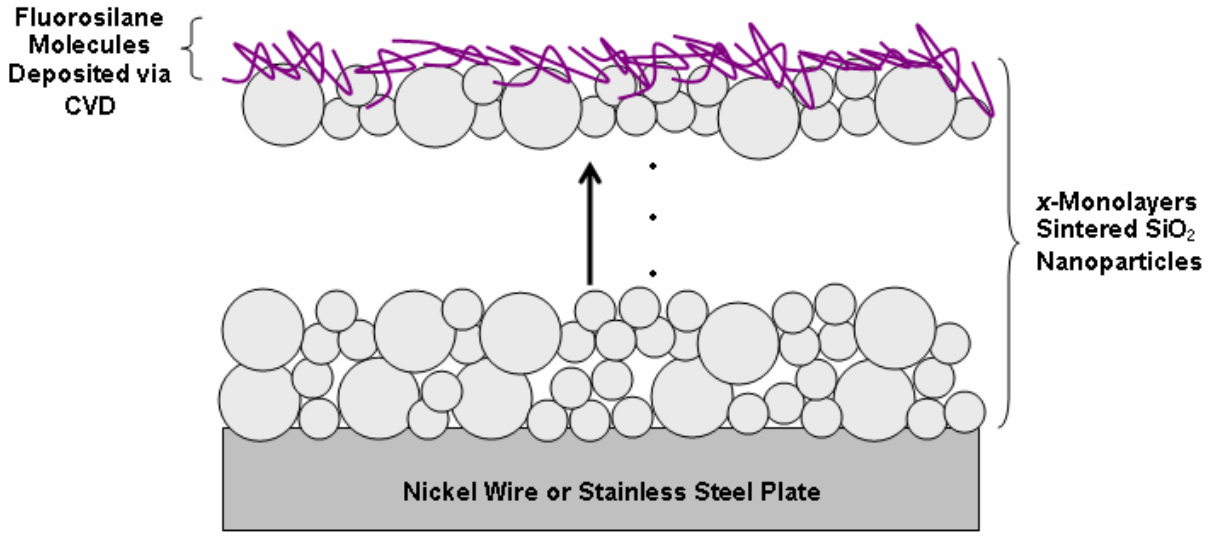

Figure 7: Sketch of a Hydrophobic Coating on Nickel Wires and Stainless Steel Plates. The coating is identical in constituency and texture to the superhydrophilic coating, except that molecules of fluorosilane have been deposited on the top layer of particles using chemical vapor deposition.

3. WIRE BOILING EXPERIMENTS IN WATER

3.1. Experimental Apparatus

The boiling heat transfer coefficient and critical heat flux were measured for bare nickel wires and coated nickel wires in pure de-ionized water at atmospheric pressure. Figure 8 depicts the pre-existing experimental apparatus used to conduct pool boiling experiments with the nickel wires. The experimental apparatus and technique for obtaining boiling curves were loosely based on that established by Nukiyama in 1934 for attaining pool boiling curves in water [19], though modern power sources and data collection equipment make the tasks of control and acquisition significantly simpler and more accurate. The pool boiling apparatus consisted of an inner test bath surrounded an outer isothermal bath. The isothermal bath was filled with tap water and kept at saturation using an electric preheater. The facility was constructed primarily of polycarbonate to aid in the visualization of the pool boiling experiments. However, the polycarbonate effectively insulated the inner test bath, so several modifications were made to the existing facility, including changing the bottom wall of the inner bath to aluminum to decrease the duration required for heat up. Nickel wires were attached to the copper leads using tin-lead solder.

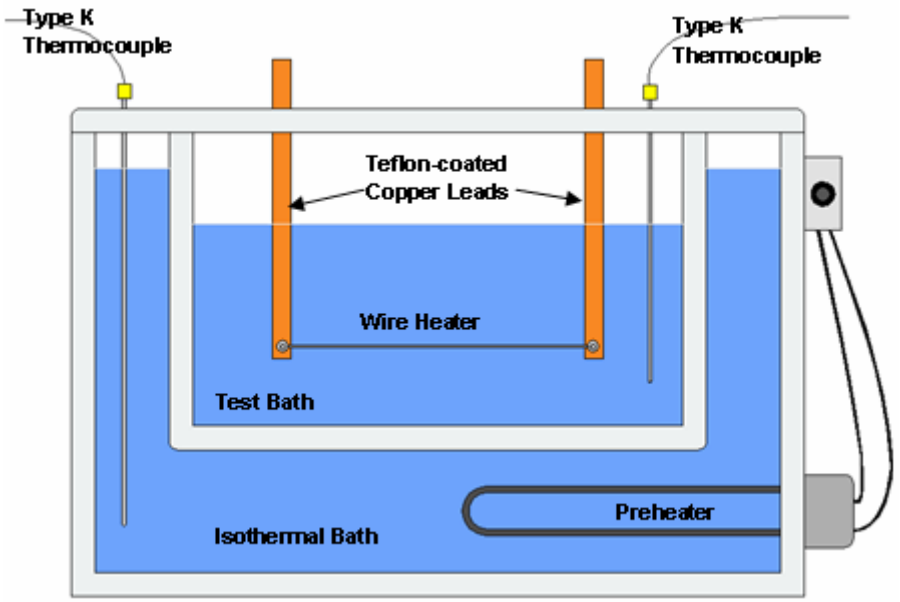

Figure 8: Schematic of the Wire Boiling Facility. Tests were conducted by resistively heating bare or coated nickel wires in de-ionized water at atmospheric pressure. ***Original boiling facility constructed by Tim Lucas, with modifications made by the author.***

Considering that surface chemistry can dramatically alter wettability, and in turn, affect boiling heat transfer, corrosion and oxidation of boiling surfaces cannot be ignored. Surface oxidation, or aging, has been shown to increase the wettability of de-ionized water on many metal surfaces [20], and oxidation has even been used as a technique to enhance the critical heat flux on copper surfaces [21]. Corrosion effects may either increase or decrease nucleate boiling heat transfer, depending on the original surface material [22]. Nukiyama recognized that electrolysis effects caused significant variations in his experimental results [19]. Stralen and Sluyter even advocated using AC current for wire pool boiling tests to alleviate fouling due to electrolysis [23], despite the added difficulties in measurement and control over the use of DC current. Therefore, to obtain unadulterated boiling curves, corrosion and electrolysis should be minimized in the boiling system. Even when using de-ionized water, corrosion is difficult to avoid. Carbon dioxide gas from the air dissolves in the water and forms carbonic acid, which disassociates to increase the hydronium ion concentration, making the water slightly acidic and promoting corrosion. Additionally, application of an external potential effectively creates an electrolytic cell, which may cause corrosion reactions which are nominally non-spontaneous. High voltages may also increase corrosion reaction rates. Several steps were taken to reduce the impact of electrochemical corrosion and associated effects in the pool boiling experiments. The copper leads were insulated with PTFE tubing to mitigate electrochemical effects, similar to Nukiyama covering his electrical leads with glass to reduce electrolysis [19]. Pure nickel wire was chosen for the boiling surface because pure nickel displays very good corrosion resistance in a variety of environments, even at moderately high temperatures [24, 25, 26]. Additionally, by grounding the positive leg of the power supply, the potential of the nickel wire was kept below earth ground, further reducing the likelihood for oxidation at the wire surface [27].

For the boiling experiments, the wire was heated resistively using a Sorensen SRL DC power supply. While the electric preheater brought the isothermal bath and test fluid up to saturation temperature, the wire surface was degassed by operating at low heat fluxes. An Agilent Technologies 34980A Data Acquisition System measured the voltage drop across the wire, along with the voltage drop across a shunt resistor to determine the current passing through the wire. The heat flux through the wire was calculated by:

$$q'' = \frac{IV}{\pi DL} \qquad (1)$$

The temperature of the nickel wire was calculated using the temperature coefficient of resistance method, where the change in electrical resistance of the wire was correlated to the temperature change of the wire using:

$$R(T) = R(T_0)[1 + \alpha \Delta T] \qquad (2)$$

In addition to its corrosion resistance, nickel was chosen for its high sensitivity in electrical resistivity over the temperature range of interest (i.e. large temperature coefficient of resistance), as is the case for most pure metals when compared to metal alloys. The linearized temperature coefficient of resistance, α, for the nickel was determined to be 0.0053 ± 0.0006 K^{-1} over the temperature range of interest, which is outlined in section 3.1.1.

Boiling tests were conducted by increasing the power in steps until CHF was reached. At CHF, the nickel wire typically became red hot and subsequently failed. At each power step, the heat flux and wire resistance were recorded for the purpose of plotting boiling curves and calculating the effective heat transfer coefficient. The effective heat transfer coefficient at the wire surface is given by Newton's Law of Cooling:

$$q'' = h_{eff}(T_w - T_{sat}) \qquad (3)$$

Measurement uncertainty was determined using stated uncertainty values for the thermocouples and data acquisition system published by the manufacturers. Using the method of error propagation [28], measurement uncertainty was evaluated for all calculated quantities. If some calculated quantity, f, is function of one or more independent measured variables, x_1, x_2, x_3,…x_n (i.e., $f = f(x_1, x_2, x_3, \ldots x_n)$), and each measured variable has associated uncertainty σ_{xi}, then the uncertainty of the calculated quantity will be:

$$\sigma_f = \sqrt{\left(\frac{\partial f}{\partial x_1}\right)^2 \sigma_{x_1}^2 + \ldots + \left(\frac{\partial f}{\partial x_n}\right)^2 \sigma_{x_n}^2} \qquad (4)$$

Table 2 lists experimental error for parameters which were measured directly. Uncertainty for all other quantities could be propagated using these uncertainties. The experimental uncertainty for all wire tests in water was typically 2.2% or less for the heat flux, 11% or less for the wall superheat, and 12% or less for the heat transfer coefficient. Uncertainty in the wall superheat and heat transfer coefficient was primarily due to the uncertainty associated with the linearized temperature coefficient of resistance for the nickel wire (see section 3.1.1).

A Biot-type analysis reveals that one may approximate the surface temperature of the wire as equal to the average radial temperature due to the small diameter and high thermal conductivity of nickel. The Biot number for the nickel wire under boiling conditions is expressed by:

$$Bi = \frac{h_{eff} L_c}{k_{Ni}} \qquad (5)$$

Table 2: Experimental Uncertainties for Various Quantities

Measured Quantity	**Measurement Error**
Voltage [% of reading (V) + range error (V)]	± [0.005% + 4×10^{-6}] V
Shunt Resistance	± 4×10^{-5} Ω
Wire Diameter	± 2.54 μm
Wire Length	± 0.2 cm
Fluid Temperature [TC + DAQ reading]	± [1.1 ºC + 1.0 ºC]
Calculated Quantities	
Heat Flux	≤ ±2.2%
Wall Superheat	≤ ±11%
Heat Transfer Coefficient	≤ ±12%

Pure nickel has a thermal conductivity of 90.7 W/m-K at 27 ºC [29], and the characteristic length for the 0.01" (0.0254 cm) wire is $L_c = V / A_s = D/4 = 6.35\text{x}10^{-5}$ m, where V is the volume of the wire and A_s is the surface area. Taking a bounding value of the effective boiling heat transfer coefficient as 180,000 W/m^2-K, one calculates that the maximum Biot number attained by the wire under boiling conditions will be Bi=0.126. For situations where $Bi \sim\leq 0.1$, the lumped capacitance model is appropriate [30]. Therefore, since h_{eff}=180,000 W/m^2-K is an upper bounding value, it is appropriate to assume that radial temperature gradients in the nickel wire are negligible. That is to say, the measured average temperature of the wire may be approximated as equal to the average surface temperature.

3.1.1. Determination of the Temperature Coefficient of Resistance for Nickel

The temperature coefficient of resistance of the nickel wire (99.98% pure, metals basis), was first determined using tabulated values in the literature, and then verified by actual measurements. Using tabulated values of electrical resistivity between 100 ºC and 200 ºC [31], the average temperature coefficient of resistance over that range was determined to be 0.005340 K^{-1}. Experiments were also carried out to verify the value of α, in which a temperature controlled hot plate raised the temperature of a bath of water from room temperature up to 100 ºC. The nickel wire was immersed in the water, and a very small current was passed through it such that the resistance of the wire could be measured without heating the wire appreciably. A type K thermocouple measured the temperature of the bath to determine the temperature change associated with the resistance change of the wire. Although an autoclave or a fluid with a higher saturation temperature than water could have been used to obtain resistance values above 100 ºC, neither was readily available at the time. As such, the temperature coefficient of resistance was simply extrapolated for temperatures beyond 100 ºC, which is reasonable considering that the temperature coefficient of resistance remains relatively constant for small temperature changes. Figure 9 shows the measured resistance values of the wire between 50 ºC and 100 ºC. Figure 10 shows R/R_0 plotted against $T-T_0$, with a fit using least squares linear regression. The slope of the line represents the temperature coefficient of resistance, as seen in the following relation:

$$\frac{R}{R_0} = \alpha(T - T_0) + 1 \qquad (6)$$

The resistance change with temperature is very linear, yielding an average temperature coefficient of resistance of 0.005349 ± 0.0006 K^{-1} up to 100 ºC. The uncertainty in the slope accounts for both the uncertainty in temperature and resistance measurements, and was determined using the method outlined by Coleman and Steele [32]. Using values reported in the literature and experimental measurements, the temperature coefficient of resistance for the nickel wire was approximated as 0.0053 K^{-1} in all saturated water boiling tests.

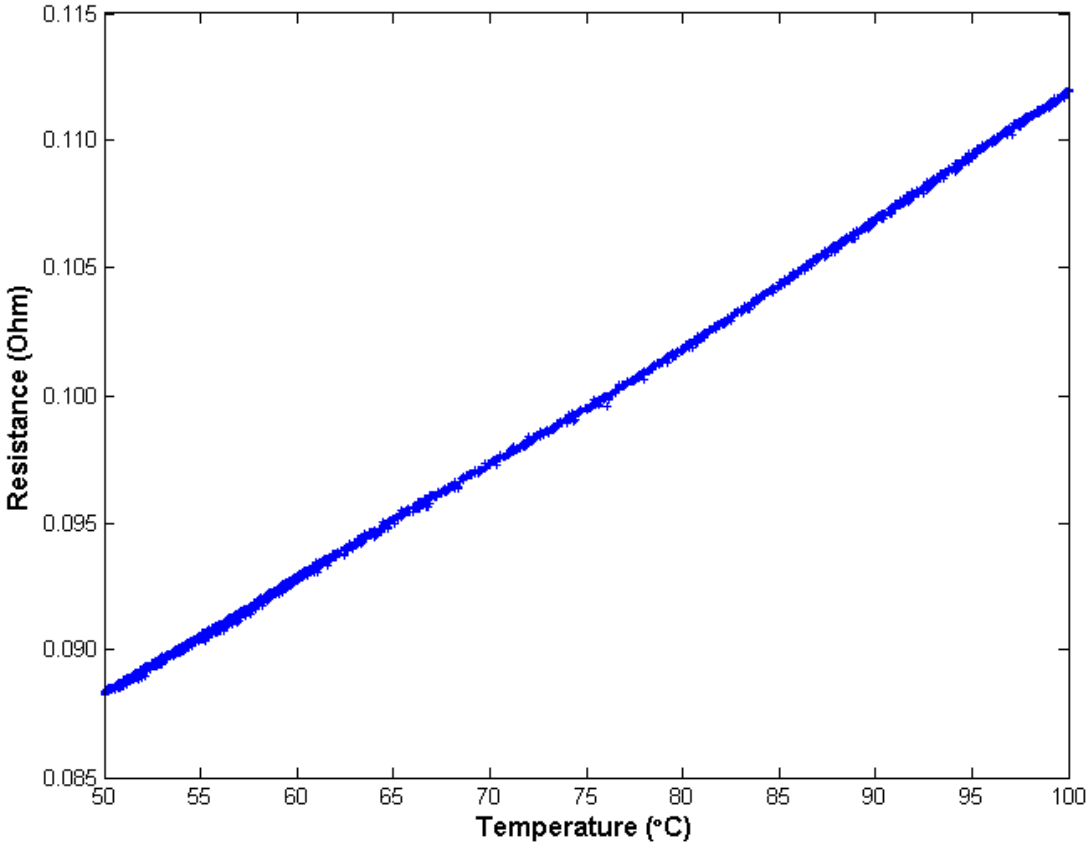

Figure 9: Electrical Resistance versus Temperature Data for a 0.01" Nickel Wire (99.98% pure, metals basis).

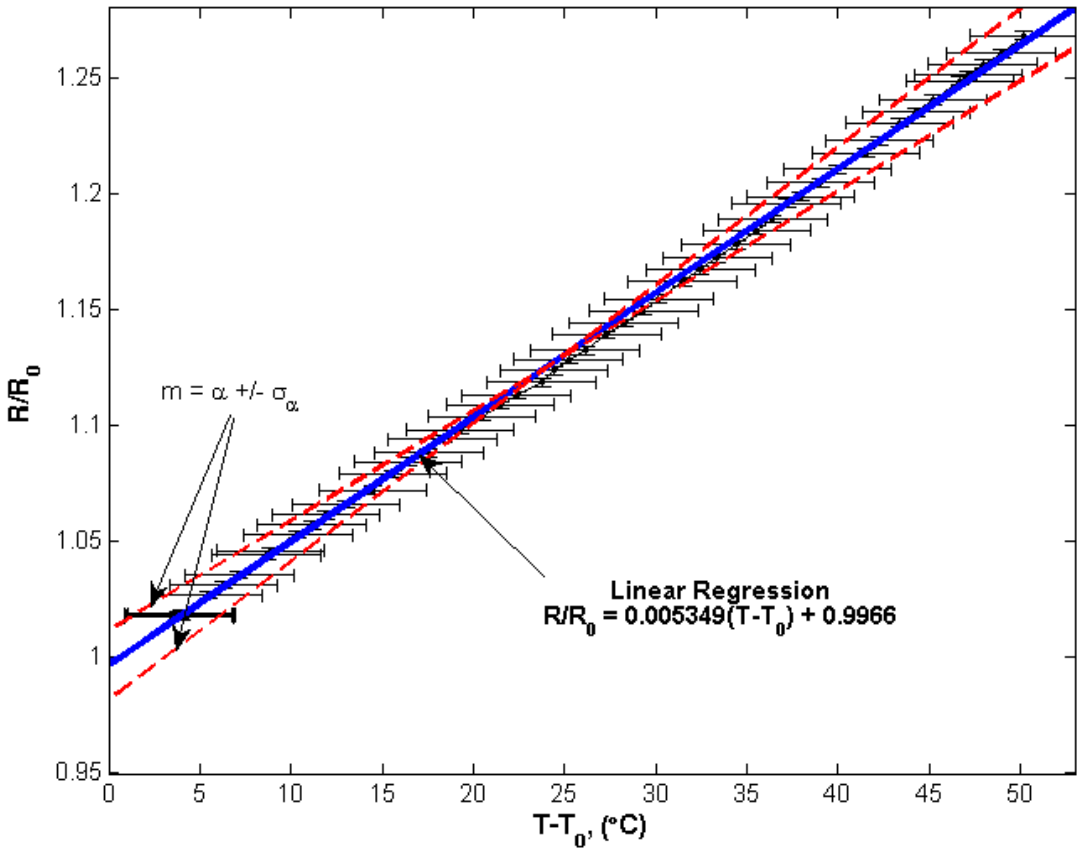

Figure 10: Least Squares Linear Regression to Compute the Average Temperature Coefficient of Resistance Between 50 ºC and 100 ºC. The dashed red lines indicate the uncertainty on the slope (temperature coefficient) associated with uncertainty from the resistance and temperature measurements. The coefficient of determination, R^2=0.9993, indicates the linear model is appropriate for the data.

3.2. Results of Wire Boiling Experiments

Pool boiling data were obtained for untreated nickel wires, hydrophilic wires with 40-bilayers, superhydrophilic wires with 10, 20, and 40-bilayers, and hydrophobic wires with 20-bilayers. Typically, three boiling tests were conducted for each case to ensure repeatability of the results. Although rare, the results of some tests appeared unusual, and were labeled as suspect. In one particular test of an untreated wire, the wire appeared visibly oxidized prior to CHF, and experienced CHF at a value higher than expected for a bare, clean nickel wire. In one case of suspected premature failure of the wire, CHF occurred at the soldered connection. In one other suspected case of premature failure for a coated wire, failure occurred on a portion of the

wire that appeared to be uncoated. To confirm suspected outliers, Peirce's criterion was applied to the CHF data [33, 34]. The following deviation ratio was calculated for each boiling test within a set:

$$\zeta_i = \frac{\left| q''_{CHF_i} - \overline{q}''_{CHF} \right|}{\sigma_{CHF}} \qquad (7)$$

If the quantity ζ_i were greater than the maximum allowable deviation, ζ^*, the test was labeled as an outlier and removed. In a set of three nominally identical CHF measurements with one value suspect, the maximum allowable deviation ratio, ζ^*, is 1.196 (the derivation of this value is found in Reference [33]). Nearly all boiling tests passed Peirce's criterion, with the exception of the aforementioned tests, which failed. In the event that a test failed Peirce's criterion, an additional boiling test was conducted for the set. In some situations, scheduled tests were canceled prior to reaching CHF due to noticeable defects in the wire or coating.

One should note that the statistical dispersion of a set of nominally identical CHF measurements, represented by the standard deviation, is perhaps a better measurement of the uncertainty in CHF rather than the measurement error associated with the heat flux, even when one accounts for the heat flux step size (~50 kW/m^2 for wire tests in water). Reporting the stochastic uncertainty is most appropriate because departure from nucleate boiling is a local phenomenon [35, 36], whereas the measured heat flux in the experiment is the average across the entire wire, not the local heat flux. Additionally, local parameters on the wire and electrochemical effects on the boiling surface, which affect CHF, are difficult to control, thereby introducing additional random errors into the CHF measurement.

To validate the experimental apparatus and approximate the accuracy of the results, CHF values for bare, untreated wires were compared to CHF predictions from theory and those in the literature for similar experiments. Lienhard's adaptation of the hydrodynamic instability theory for application to finite bodies [37] is generally useful for predicting the peak pool boiling heat flux on various surface geometries. However, the "small horizontal cylinder" prediction only applies for dimensionless lengths $0.15 \leq R^* < 1.2$. The non-dimensional radius for the wire heater can be calculated from:

$$R^* = \frac{r}{R_c} \qquad (8)$$

where r is the wire diameter and the critical bubble radius, r_c, can be calculated using:

$$R_c = \sqrt{\frac{\sigma}{g(\rho_f - \rho_g)}} \qquad (9)$$

For saturated water at atmospheric pressure, one finds the critical bubble radius to be Rc=2.50x10^{-3} m. For the 0.01" (0.0254 cm) wire, the non-dimensional radius is R^*=0.0507. Therefore, Lienhard's "small horizontal cylinder" prediction for the peak pool boiling heat flux is not applicable to the 0.01" nickel wire. Sun and Lienhard report that the data for the peak heat flux begin to deviate from the prediction for R^*<0.15, due to the dominance of surface tension forces [38]. Bakhru and Lienhard write that when the radius of a wire becomes sufficiently small, hydrodynamic transitions disappear and the boiling curve becomes monotonic, with the natural convection regime proceeding directly to the film boiling regime and nucleate boiling vanishing [39]. Bakrhu and Lienhard claim that in the range of 0.01<R^*<0.15, a transition regime is present, but the traditional hydrodynamic regimes are not yet fully established. However, the boiling curves and photographic evidence obtained in this study indicate that that this is not the case for nickel wire, as clear demarcations between the natural convection, isolated bubbles, and fully developed nucleate boiling regimes exist in de-ionized water at atmospheric pressure.

The study by Bakhru and Lienhard heavily relies on the use of platinum wires, ignoring the importance of the adhesion force determined by the unique liquid-surface combination. Even Nikuyama's original study on pool boiling heat transfer demonstrates that for small wires of the same diameter, the wire material can heavily influence the peak heat flux. In the case of Nukiyama's study, Nukiyama finds the peak heat flux for nickel wires to be 40% greater than that for platinum wires in saturated water at 1 atm, both with dimensionless radius R^*=0.0279 [19]. Hong and You indicate that the lower limit on R^* for the "hydrodynamic mechanism" is fluid dependent, extending down to R^*=0.0140 for well-wetting fluids [40], but do not account

for the unique surface-fluid combination. Hong and You proposed the following CHF correlation for cylinders in the range $0.0140<R^*<0.6$:

$$\frac{q''_{CHF}}{q''_{CHF,Zuber}} \cong 0.89 + 1.18e^{-2.56\sqrt{R^*}} \qquad (10)$$

where $q''_{CHF,Zuber}$ is the Zuber prediction of CHF for an infinite flat plate, which will be discussed in section 4.3.1. However, this correlation strongly relies on Hong and You's data obtained for well-wetting fluids on platinum wires, and does not appear to agree with the trend of empirical data of peak heat flux gathered by Sun and Lienhard for $0.01<R^*<0.15$ shown in Figure 11.

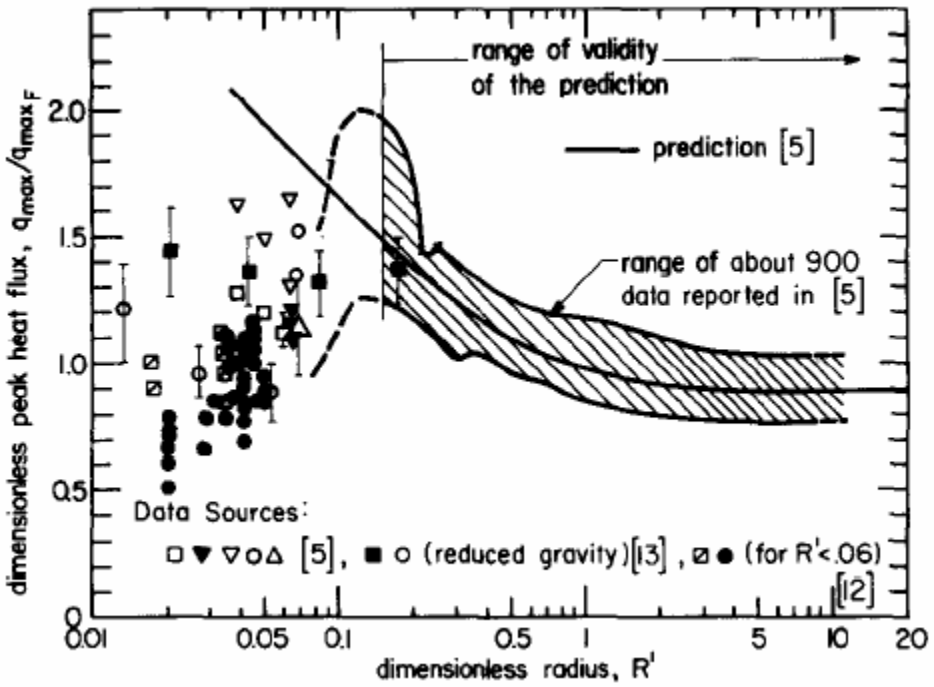

Figure 11: Peak Boiling Heat Flux from Horizontal Cylinders. Note that for $R^*<0.15$, the Lienhard prediction for small horizontal cylinders deviates significantly from empirical data. Hong and You's prediction attempts to address this region, but still tends to over-predict other empirical results. ***Source: Ref. [39], reproduced with permission of Elsevier, © 1972.***

Although there does not appear to be an appropriate correlation for predicting CHF in the case of this study with R^*, the empirical data in Figure 11 indicates that the CHF for R^*=0.0507 should fall between about $0.7\,q''_{CHF,Zuber}$ and $1.5\,q''_{CHF,Zuber}$, which equates to a CHF value between 776 kW/m^2 and 1660 kW/m^2. From the results in section 3.2.1, the average CHF for the untreated, bare nickel wire in de-ionized water falls in this range.

Boiling data were reduced and analyzed using a routine written in MATLAB. The MATLAB routine computed wall superheats for each data point, and computed the experimental uncertainty of all values using error propagation. The MATLAB routine also reduced hundreds of data points at each heat flux step to a single data point using a simple moving average. Values at each heat flux step were calculated by taking the arithmetic average of neighboring individual measurements to smooth small variations, while step increases, indicating a new heat flux level, were detected using pre-existing input criteria for the routine. Figure 12 summarizes relative effects of hydrophilic, superhydrophilic, and hydrophobic PAH/SiO_2 nanoparticle thin-films on boiling curves. Note that the boiling curve for the hydrophilic test case closely resembles that of the bare wire, except that it is shifted somewhat to the right and CHF is enhanced considerably. For the hydrophobic wire, the shape of the boiling curve resembles that of the bare wire and hydrophilic wire, except that it is shifted to the left. The substantial reduction in the wall superheat for the hydrophobic wire signifies appreciable enhancement in the nucleate boiling heat transfer coefficient. Additionally, CHF is still enhanced for the nickel wire with hydrophobic treatment over the bare wire test case. As seen in Figure 12, the most unusual behavior is exhibited by the wire with the superhydrophilic coating, where the wire temperature increases dramatically until falling at high heat fluxes. This behavior will be discussed further in section 4.2.

Table 3 summarizes average CHF values for all nickel wire boiling test cases. Note that CHF enhancement was observed for all nickel wires with thin-film coatings, regardless of the final treatment. The maximum average CHF value of 101% was observed for the nickel wires that were coated with 40-bilayers of PAH/SiO_2 and calcinated.

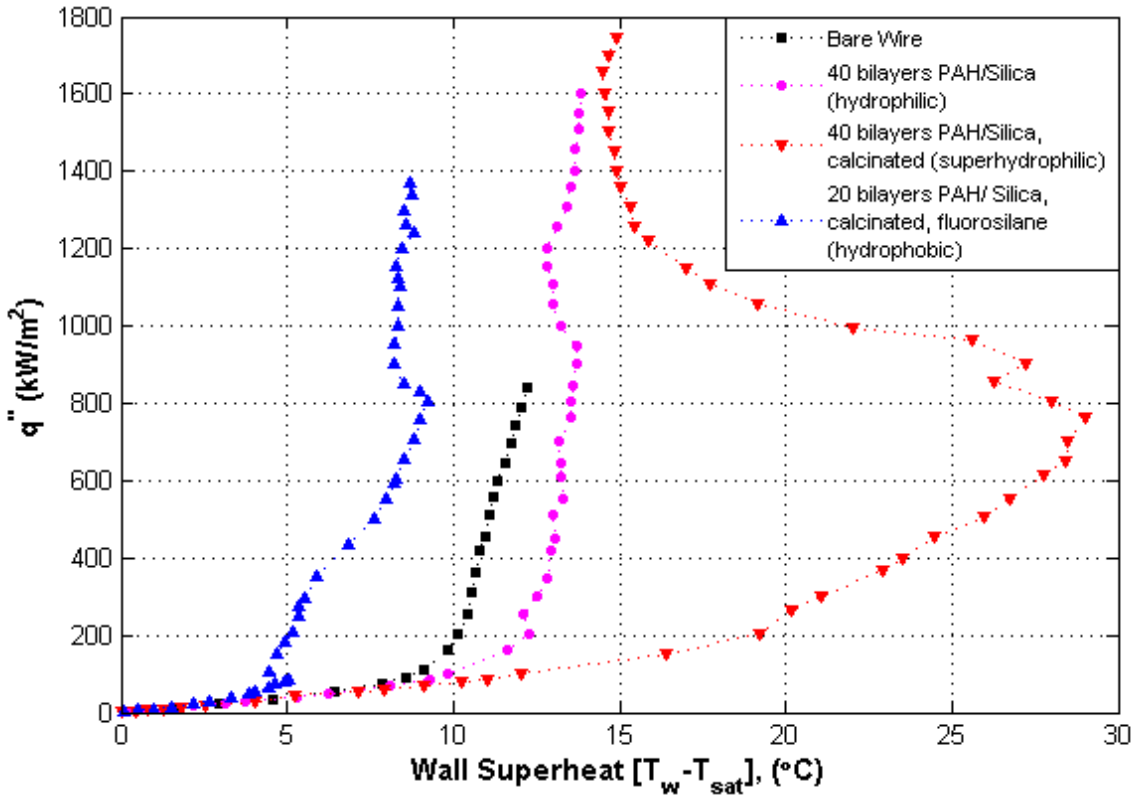

Figure 12: Typical Boiling Curves in Pure Water for 0.01" Diameter Bare Nickel Wire (squares), Wire Coated with 40 Bilayers of PAH/SiO_2, (circles), Wire Coated with 40 Bilayers PAH/SiO_2 and Calcinated (inverted triangles), and Wire Coated with 20 Bilayers PAH/SiO_2 and Calcinated with Fluorosilane Treatment (triangles). All wires were boiled in pure de-ionized water.

Table 3: Summary of CHF Values for 0.01" Nickel Wire Boiling Tests. Average enhancement for coated wires over untreated wires is also provided.

Test Case	Average CHF	CHF Std. Dev.†	CHF 90% Conf. Interval‡	CHF Enhancement
Bare Wire	862 kW/m^2	7.4%	[787 kW/m^2, 936 kW/m^2]	-
40 bilayers PAH/SiO_2	1583 kW/m^2	4.5%	[1462 kW/m^2, 1704 kW/m^2]	84%
20 bilayers PAH/SiO_2, calcinated, fluorosilane	1458 kW/m^2	21%	[933 kW/m^2, 1983 kW/m^2]	69%
10 bilayers PAH/SiO_2, calcinated	1241 kW/m^2	6.4%	[1108 kW/m^2, 1374 kW/m^2]	44%
20 bilayers PAH/SiO_2, calcinated	1402 kW/m^2	9.5%	[1234 kW/m^2, 1682 kW/m^2]	63%
40 bilayers PAH/SiO_2, calcinated	1735 kW/m^2	1.6%	[1687 kW/m^2, 1783 kW/m^2]	101%

†Standard deviation (% of average) over three nominally identical tests (four tests for the bare wire case).
‡Calculated from the t-distribution.

Although the superhydrophilic wires displayed the greatest enhancement in CHF, they suffered substantial degradation in the heat transfer coefficient. Figure 13 shows typical results for the effective heat transfer coefficient plotted against heat flux for nickel wire coated with the PAH/SiO_2 thin-films. Nickel wires with the non-calcinated, hydrophilic coating showed little change in the heat transfer coefficient at a given heat flux when compared with the base case. The wires with the hydrophobic treatment showed on average 127% enhancement in h_{eff} over the untreated surfaces at their respective critical heat fluxes. Clearly, the hydrophobic coating demonstrates the optimum performance enhancement when one accounts for both the nucleate boiling heat transfer coefficient and CHF. Detailed results for all test cases are provided in sections 3.2.1 through 3.2.4.

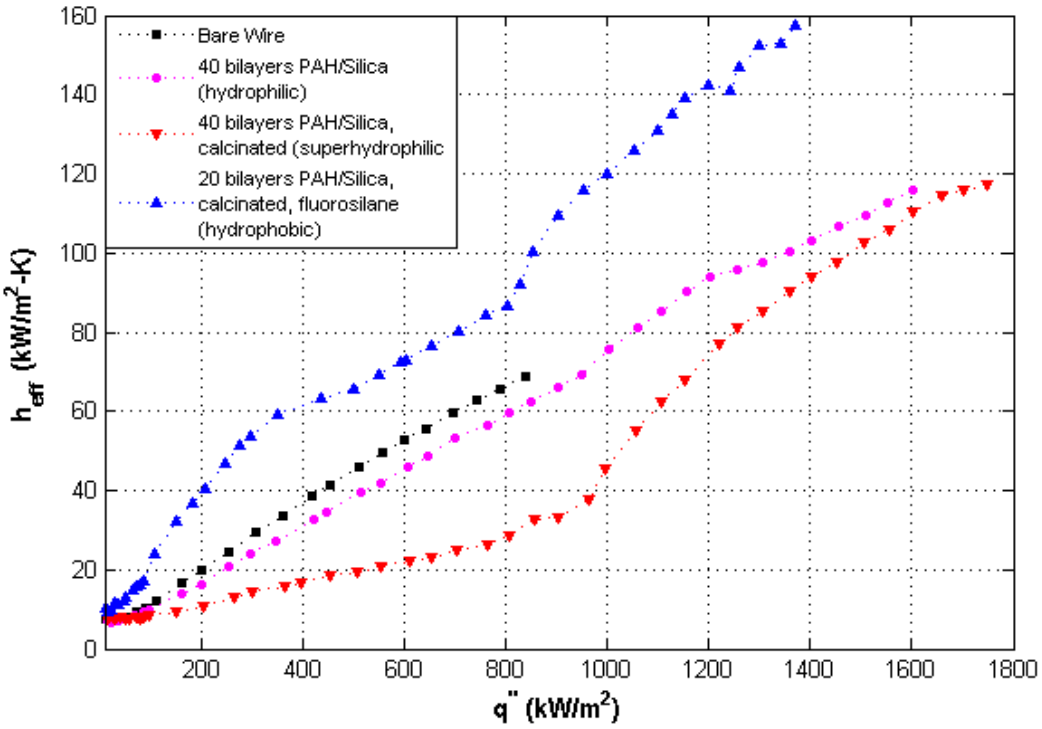

Figure 13: Typical Values of the Heat Transfer Coefficient versus Heat Flux in Pure Water for Uncoated and Coated Nickel Wires Boiled in Pure Water.

3.2.1. Untreated Nickel Wire

Untreated, bare nickel wires were tested in saturated de-ionized water at atmospheric pressure to establish a base case and determine relative changes in wall superheat and CHF achieved with application of the thin-film coatings. Nickel wires were tested with the as-received surface condition, with no sanding or other mechanical treatments. Prior to the tests, the wires were cleaned aggressively by sonicating in acetone and then rinsing in de-ionized water. This cleaning process removed any potential dirt, grease, or other contaminants that could adversely affect the boiling tests. Figure 14 shows plots of the four boiling tests used to establish a baseline measurement, with an average CHF of all tests being 862 ± 63.5 kW/m^2. At CHF, a hot spot developed at a random location on the wire, with the wire subsequently failing at that point. In the following plots of boiling curves, the peak heat flux plotted for each test represents the critical heat flux for that test. Figure 15 shows the effective heat transfer coefficient plotted against the heat flux for the bare wire tests. From the figure, one can see that the spread of values for the tests fall within the experimental uncertainty on the heat transfer coefficient (±12%).

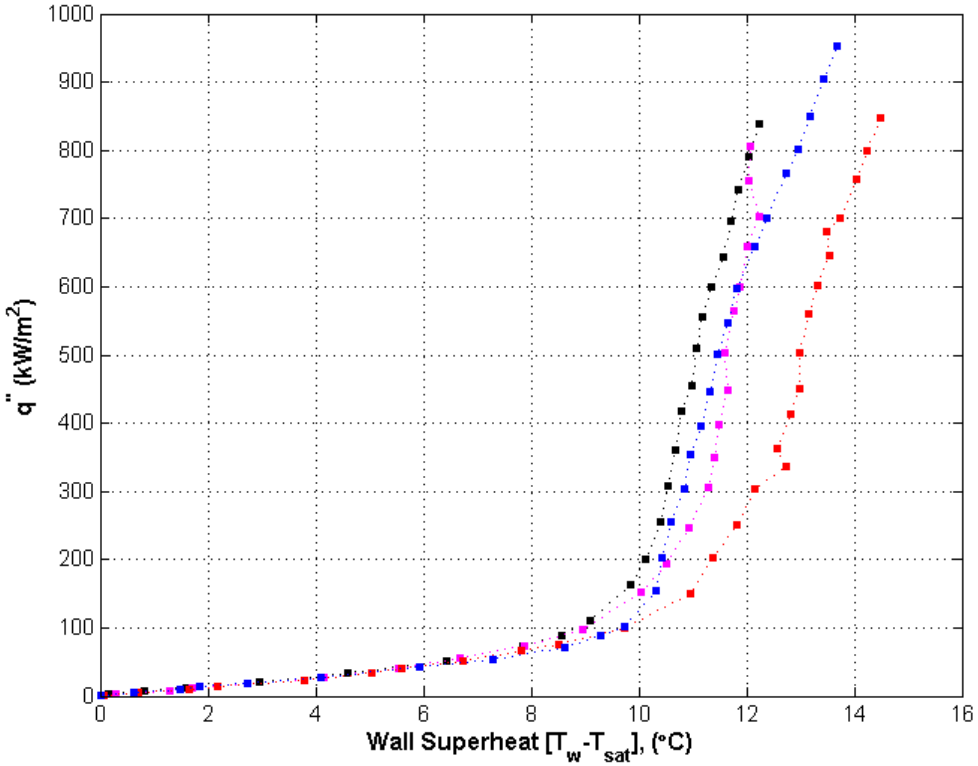

Figure 14: Boiling Curves in Pure Water for the Bare 0.01" Nickel Wires. These four boiling tests established the base case from which relative enhancement was determined for CHF and the boiling heat transfer coefficient in subsequent tests.

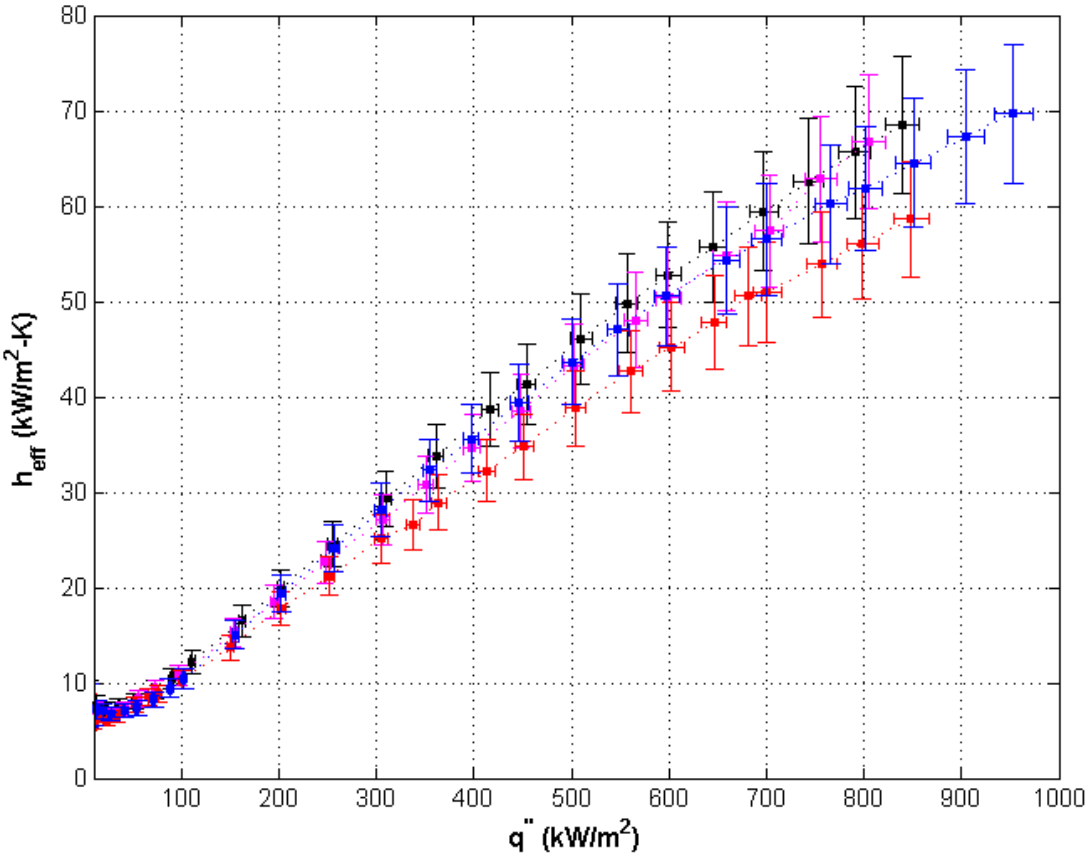

Figure 15: Effective Heat Transfer Coefficient Plotted Against Heat Flux for the Bare 0.01" Nickel Wire Boiling Tests. Error bars represent the experimental uncertainty in the heat transfer coefficient and heat flux. Note that the spread of h_{eff} values falls within the experimental uncertainty.

3.2.2. Nickel Wire Treated with a Hydrophilic SiO_2/PAH Thin-Film Coating

Nickel wires coated with hydrophilic thin-films (see section 2.3.1) were tested in saturated de-ionized water at atmospheric pressure. All hydrophilic wires that were tested had 40-bilayers of PAH/SiO_2. Figure 16, which also provides a bare wire boiling test for reference, shows that CHF is enhanced considerably for the wires with the hydrophilic coatings, while the wall superheat increased only slightly. The average CHF for the hydrophilic wires was 1583 ± 72.0 kW/m^2. Figure 17 shows photographs of boiling from the hydrophilic wire and bare wire at comparable heat fluxes. Qualitatively, the nucleation site density in boiling from the hydrophilic wire appears comparable to that of the bare wire. Figure 18 indicates that for a given heat flux, the effective heat transfer coefficient for the hydrophilic wires is only slightly degraded relative to the bare wire.

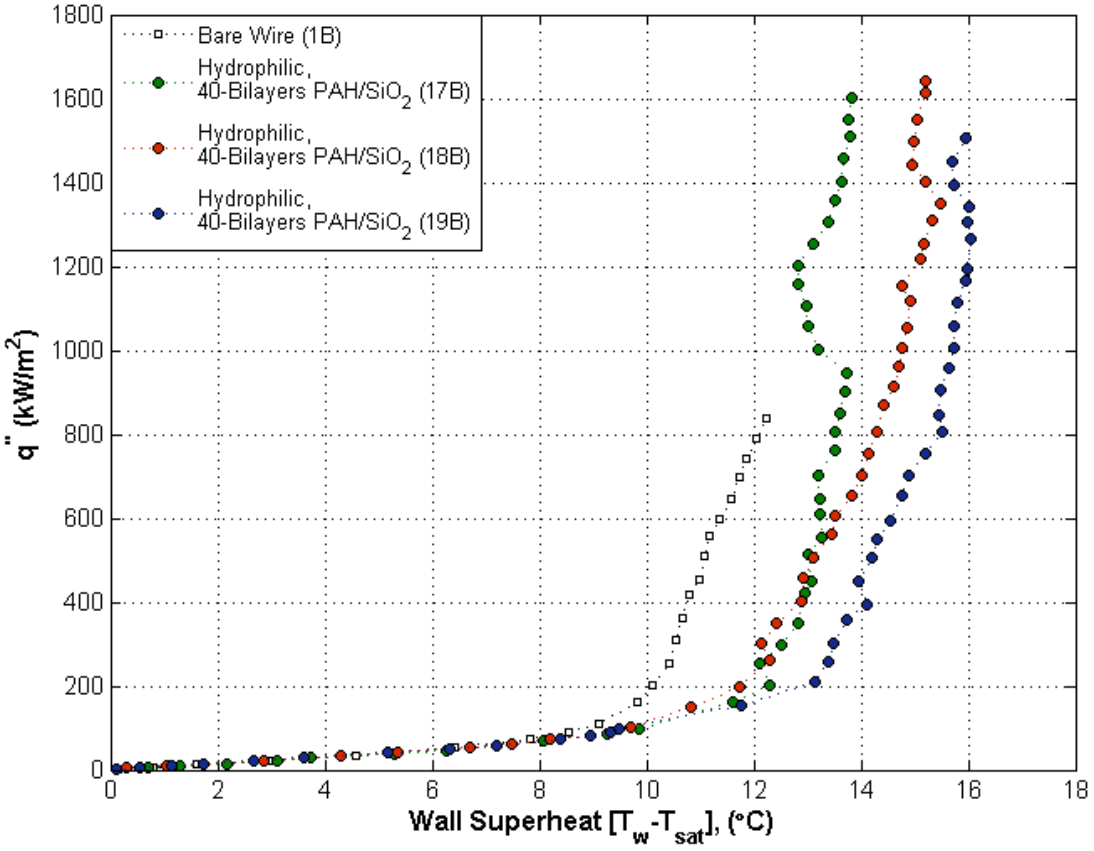

Figure 16: Boiling Curves in Pure Water for 0.01" Nickel Wires Coated with 40-Bilayers PAH/SiO_2. A boiling curve for a bare nickel wire is shown for reference. The number in parentheses is the test identifier.

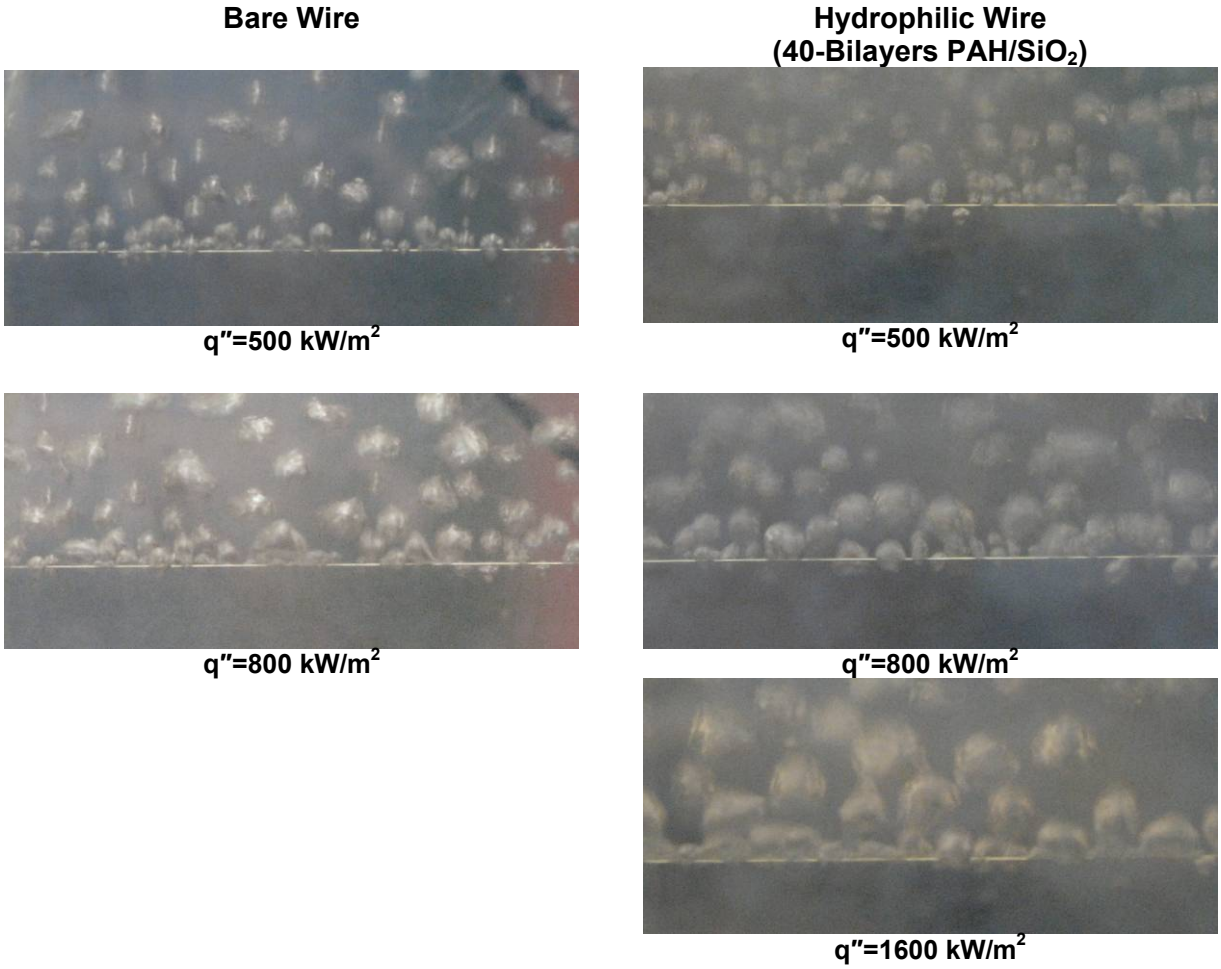

Figure 17: Boiling from a Bare Wire (Left side) and a Hydrophilic Wire Coated with 40-Bilayers PAH/SiO_2 (Right side).

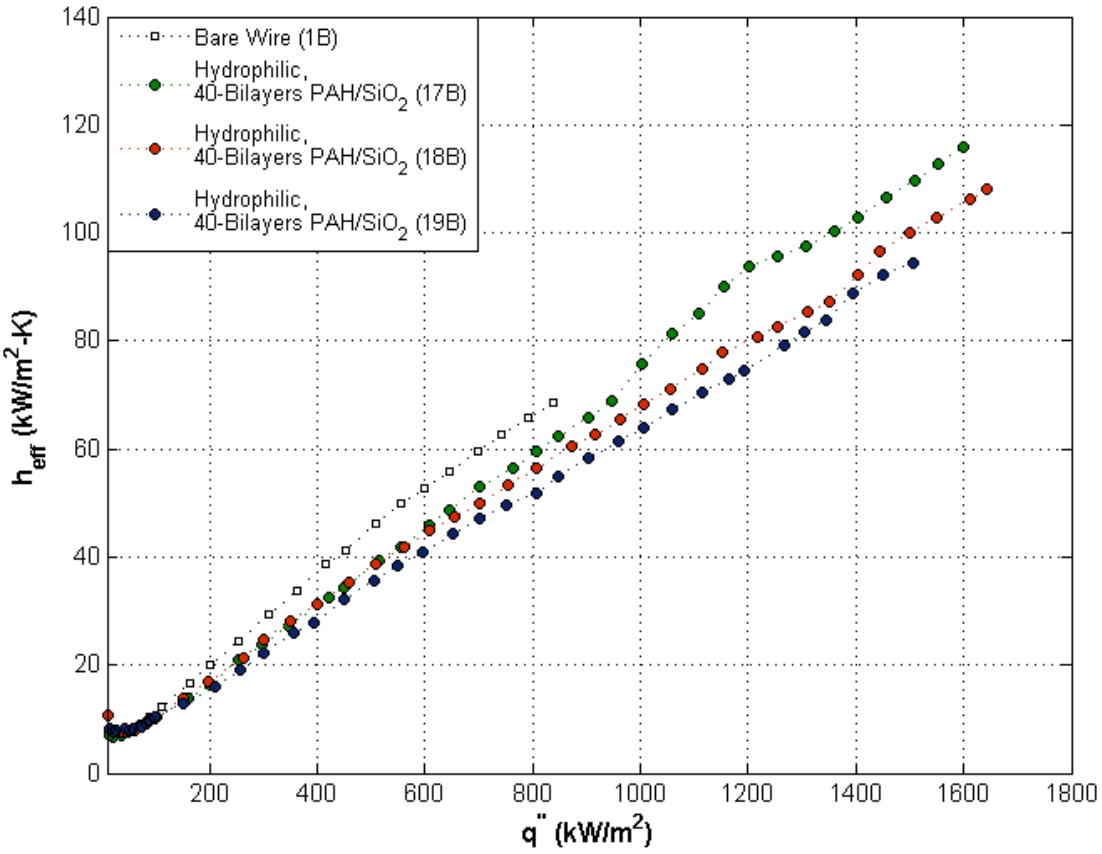

Figure 18: Effective Heat Transfer Coefficient Plotted Against Heat Flux for 0.01" Nickel Wires Coated with 40-Bilayers PAH/SiO_2. Results for a bare nickel wire are shown for reference. Error bars have been omitted for clarity.

3.2.3. Nickel Wire Treated with a Superhydrophilic SiO_2/PAH Thin-film Coating

Nickel wires coated with superhydrophilic thin-films (see section 2.3.2) were tested in saturated de-ionized water at atmospheric pressure. Superhydrophilic wires with three different coating thicknesses were tested: 10-bilayers, 20-bilayers, and 40 bilayers of PAH/SiO_2, in order to gauge the effect of the coating thickness on nucleate boiling heat transfer and CHF. Figure 19 shows the boiling curves for the 10-bilayer case, Figure 20 shows boiling curves for the 20-bilayer case, and Figure 21 shows boiling curves for the 40-bilayer case. The average CHF was 1241 ± 79.1 kW/m^2 for 10-bilayers of PAH/SiO_2, 1402 ± 133 kW/m^2 for 20-bilayers, and 1735 ± 28.2 kW/m^2 for 40-bilayers. There appears to be a clear trend in CHF with coating thickness for the superhydrophilic thin-films. Figure 22 shows that the CHF increases linearly between 10 and 40-bilayers with coating thickness. In all superhydrophilic test cases, the wall superheat is much greater than that for the bare wire cases at low heat fluxes, only falling at high heat fluxes.

However, there appears to be no clear trend between wall superheat and coating thickness. Figure 23 shows this observation, indicating that there is significant scatter in the effective heat transfer coefficient between all superhydrophilic wire tests, regardless of coating thickness.

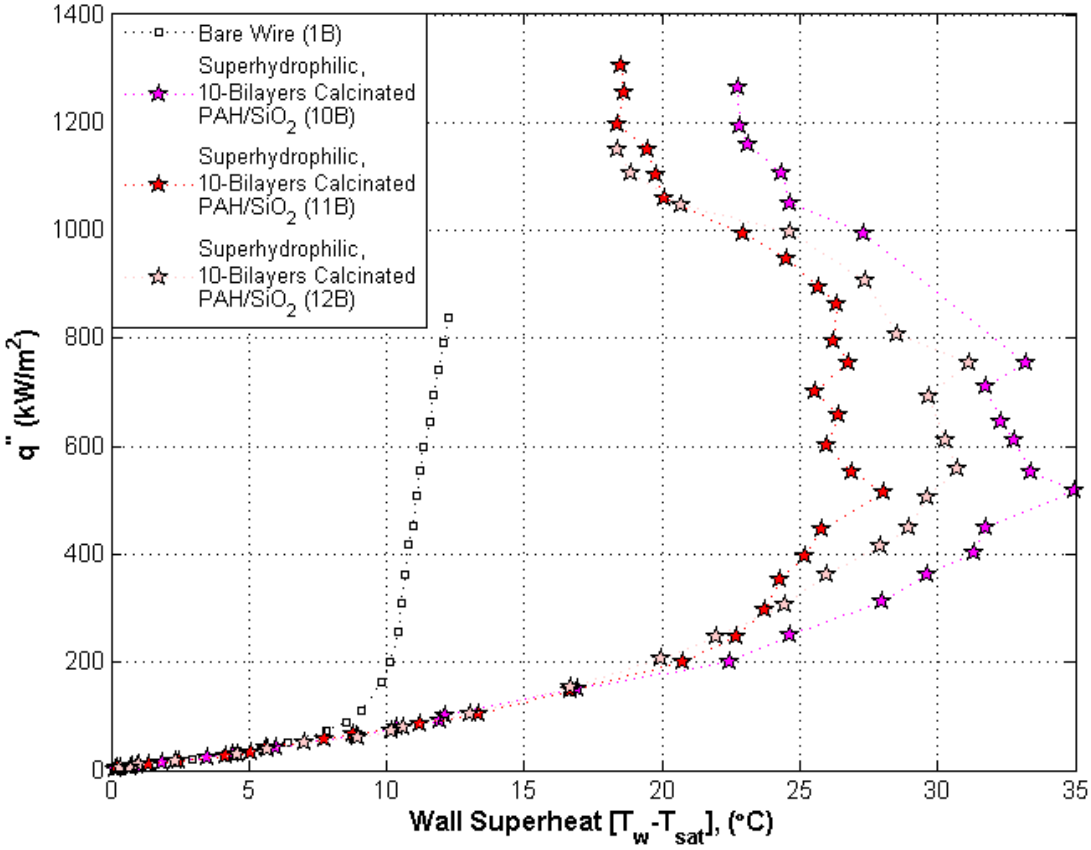

Figure 19: Boiling Curves in Pure Water for 0.01" Nickel Wires Coated with 10-Bilayers PAH/SiO_2 and Calcinated. A boiling curve for a bare nickel wire is included for reference.

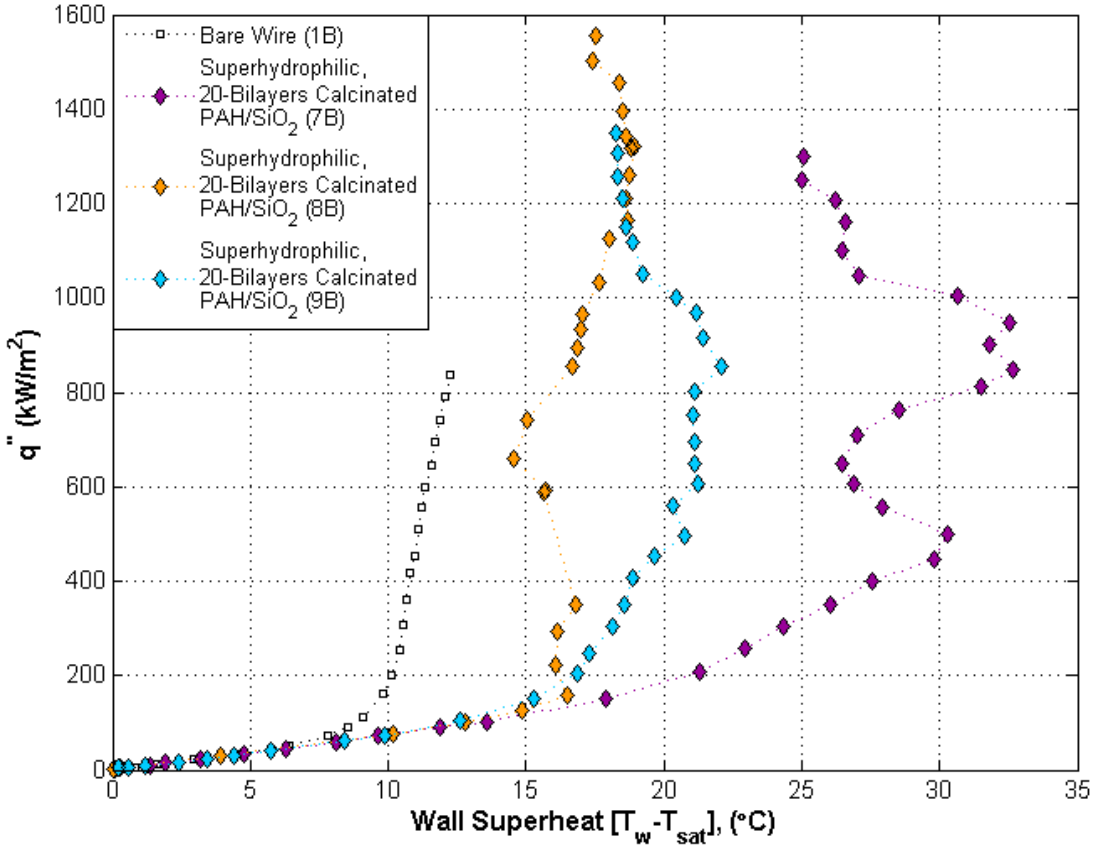

Figure 20: Boiling Curves in Pure Water for 0.01" Nickel Wires Coated with 20-Bilayers PAH/SiO_2 and Calcinated. A boiling curve for a bare nickel wire is included for reference. Note that for test 8B, power was lost mid-test after boiling incipience, and the data collection was re-started from 0 kW/m^2. This likely resulted in flooding of vapor cavities on the second attempt, shifting the curve to the left (see section 4.2).

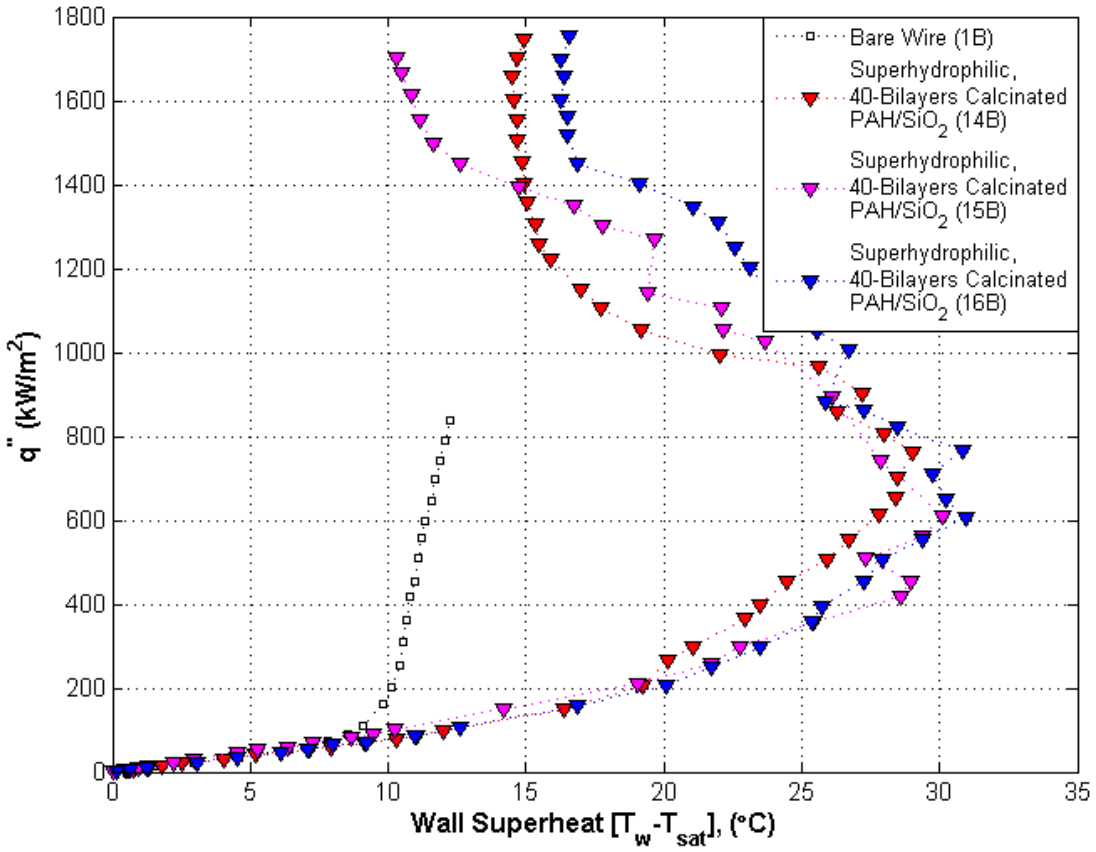

Figure 21: Boiling Curves in Pure Water for 0.01" Nickel Wires Coated with 40-Bilayers PAH/SiO_2 and Calcinated. A boiling curve for a bare nickel wire is included for reference.

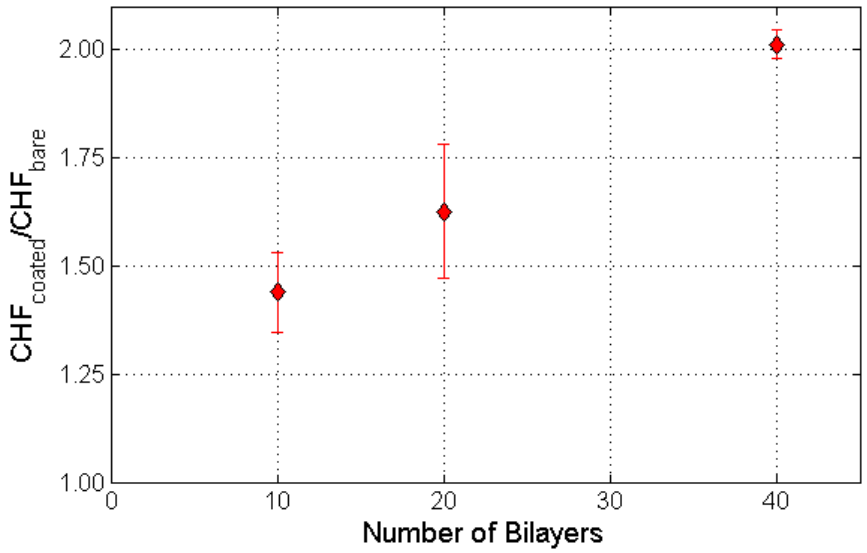

Figure 22: Average CHF Enhancement versus Coating Thickness for Calcinated PAH/SiO2 Coated Nickel Wires. Error bars indicate the standard deviation in CHF for three nominally identical tests.

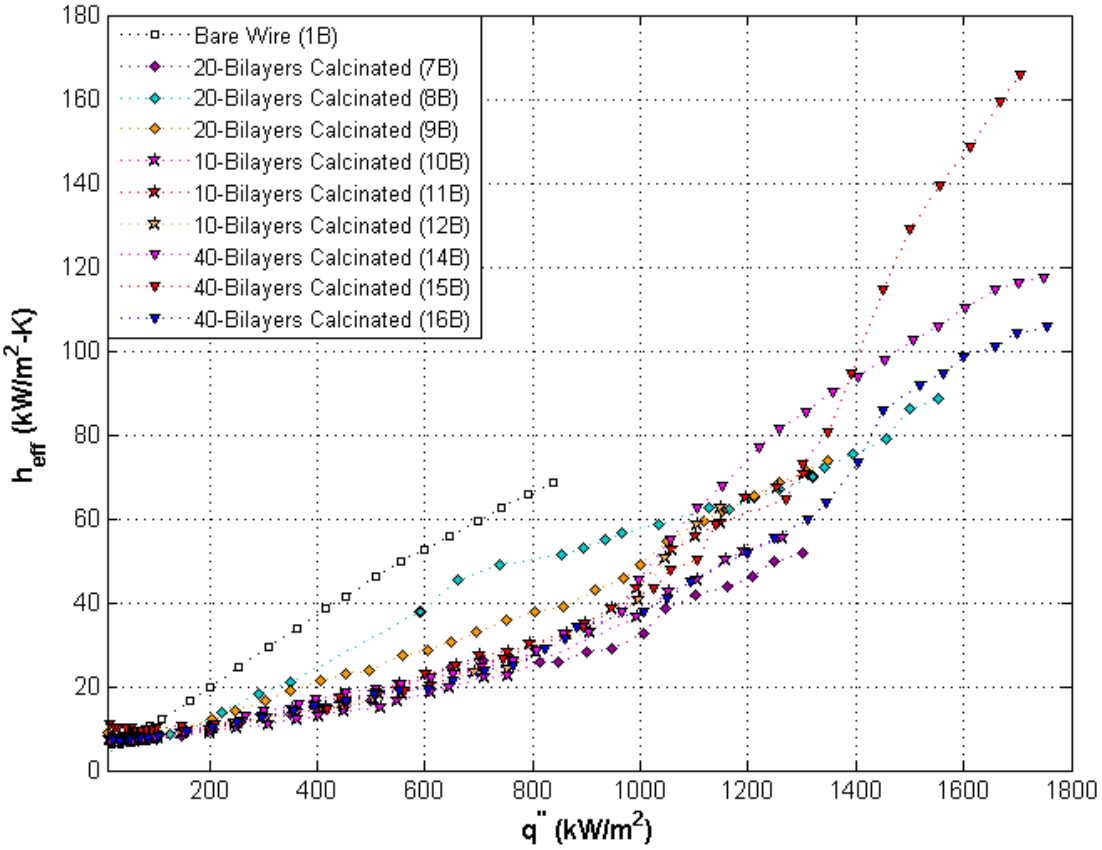

Figure 23: Effective Heat Transfer Coefficient versus Heat Flux for All Superhydrophilic Wire Tests. There does not appear to be a clear correlation between coating thickness and nucleate boiling heat transfer coefficient, though the heat transfer coefficient does recover at higher heat fluxes.

It was hypothesized that the reversal of the boiling curves at high heat fluxes for the superhydrophilic wires was a result of vapor entrapment in nucleation cavities, thereby reducing the superheat required for nucleation (see section 4.2 for more details). To test this hypothesis, several boiling tests were conducted using 0.01" nickel wires with superhydrophilic coatings in which the heat flux was cycled below CHF. Figure 24 shows the results of one such test for a nickel wire coated with 20-bilayers PAH/SiO_2 and calcinated (test 21B). Figure 25 shows a similar test for a nickel wire coated with 40-bilayers PAH/SiO_2 and calcinated (test 29B). A hysteresis effect clearly exists with the superhydrophilic coatings, and does not appear to depend on coating thickness. Visualization of boiling from the superhydrophilic wire helps corroborate the high wall superheats and hysteresis observed in the boiling curves. In Figure 26, one can see that even at a high heat flux of q''=500 kW/m^2, the nucleation site density is surprisingly low on the superhydrophilic wire, with only a few active sites. The nucleation site density remains low

compared to the bare wire, up to the point where the reversal in the boiling curve is observed. In the ramp down and second ramp up of the heat flux, the photographs show a higher nucleation site density compared to the initial ramp up in heat flux.

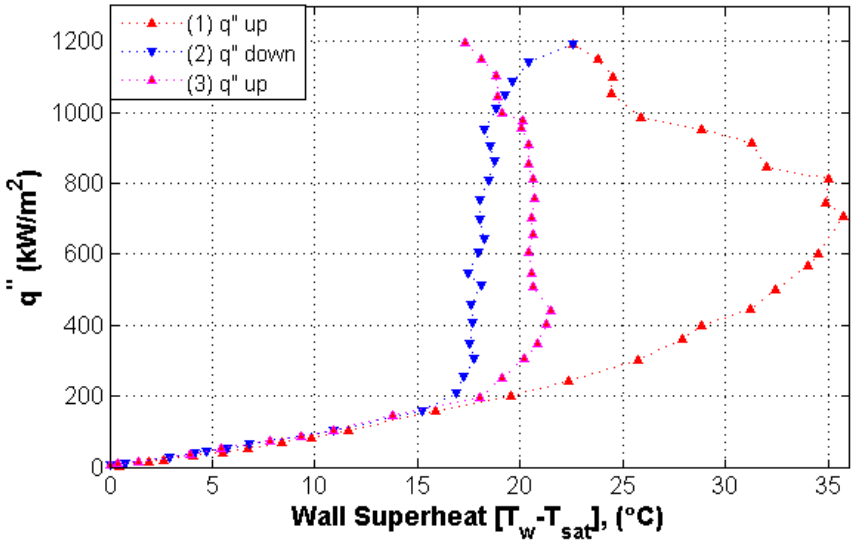

Figure 24: Boiling Test Results for 0.01" Nickel Wire Coated with 20-Bilayers PAH/SiO_2 and Calcinated (22B). The heat flux was cycled three times, demonstrating a hysteresis in the boiling curve likely resulting from vapor entrapment in initially fully-flooded cavities. Note that the heat flux was kept below CHF.

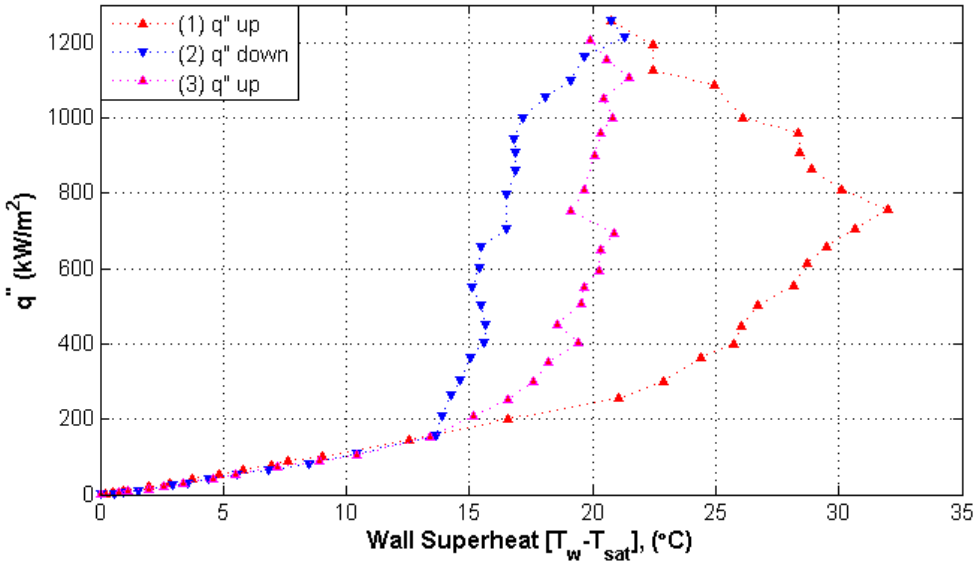

Figure 25: Boiling Test Results for 0.01" Nickel Wire Coated with 40-Bilayers PAH/SiO_2 and Calcinated (29B). The heat flux was cycled three times below CHF. As in the 20-bilayer case, a hysteresis effect was observed, with no apparent influence from coating thickness.

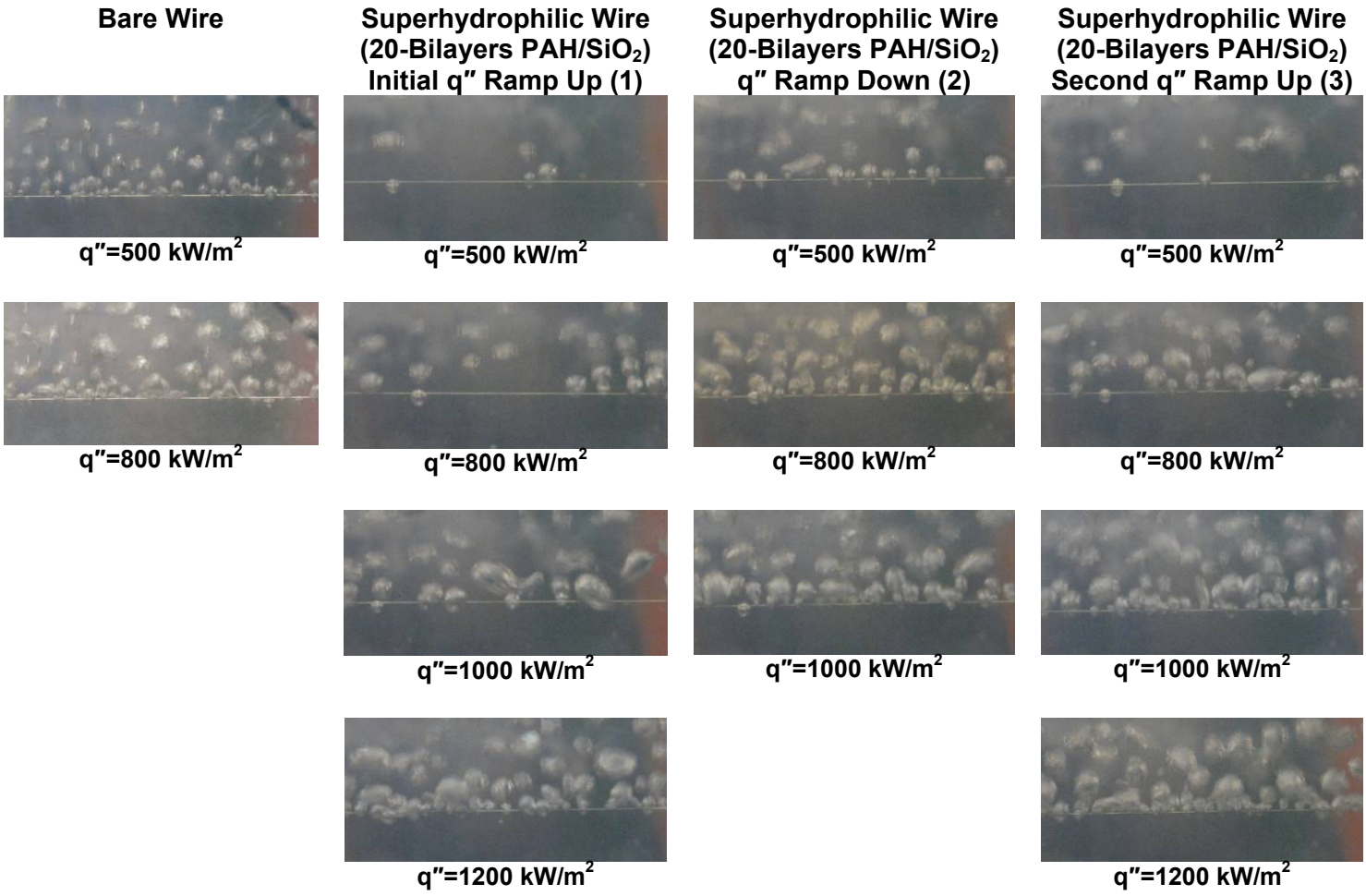

Figure 26: Boiling from a Bare Wire (Left side) and a Superhydrophilic Wire Coated with 20-Bilayers PAH/SiO_2 and Calcinated (Three columns on the right). Photographs for the superhydrophilic case are from test 22B (see Figure 24 for the boiling curve), in which the heat flux was cycled below CHF. Clearly, a hysteresis exists, due to a higher nucleation site density during subsequent heat flux cycles.

3.2.4. Nickel Wire Treated with a Hydrophobic SiO_2/PAH + Fluorosilane Thin-Film Coating

Nickel wires coated with hydrophobic thin-films (see section 2.3.3) were tested in saturated de-ionized water at atmospheric pressure. All hydrophobic wires that were tested had 20-bilayers of PAH/SiO_2. Figure 27 shows boiling curves for the three hydrophobic wires tested. As seen in Figure 27, the incipience of boiling occurs at a lower heat flux and wall superheat than for the bare wire tests. Additionally, CHF is enhanced in all three tests over the bare wire case. However, the scatter in the CHF values for the three nominally identical tests is somewhat larger than for the other tests cases, possibly due to the lack of control in the application of the top layer of fluorosilane. Interestingly, the average CHF value for the nickel wires with 20-bilayers PAH/SiO_2, calcinated and treated with hydrophobizing fluorosilane was 1458 ± 311 kW/m^2, within 4% of the average CHF value for the nickel wires with 20-bilayers PAH/SiO_2 and calcinated. Figure 28 shows that boiling incipience occurs at a much lower heat flux than for the bare wire, and that the nucleation site density remains higher than that of the bare wire at all heat fluxes. Figure 29 shows that the effective heat transfer coefficient for the hydrophobic wires is significantly higher than that for the bare wires at all heat fluxes, as expected from the higher nucleation site densities.

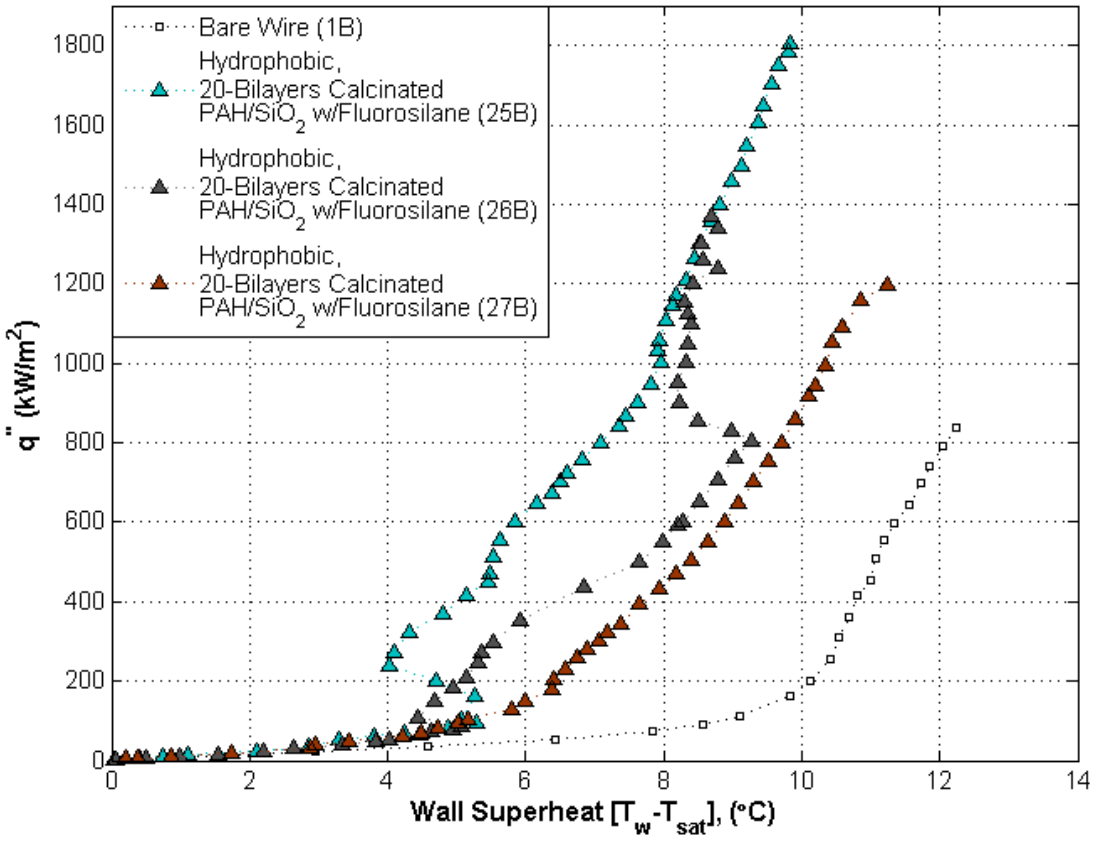

Figure 27: Boiling Curves for 0.01" Nickel Wire Coated with 20-Bilayers PAH/SiO_2, Calcinated, and Treated with Fluorosilane. A bare wire boiling curve is shown for reference. Compared to other boiling cases, the hydrophobic wires had the most scatter in CHF. The lack of control in the fluorosilane deposition process may have led to the scatter.

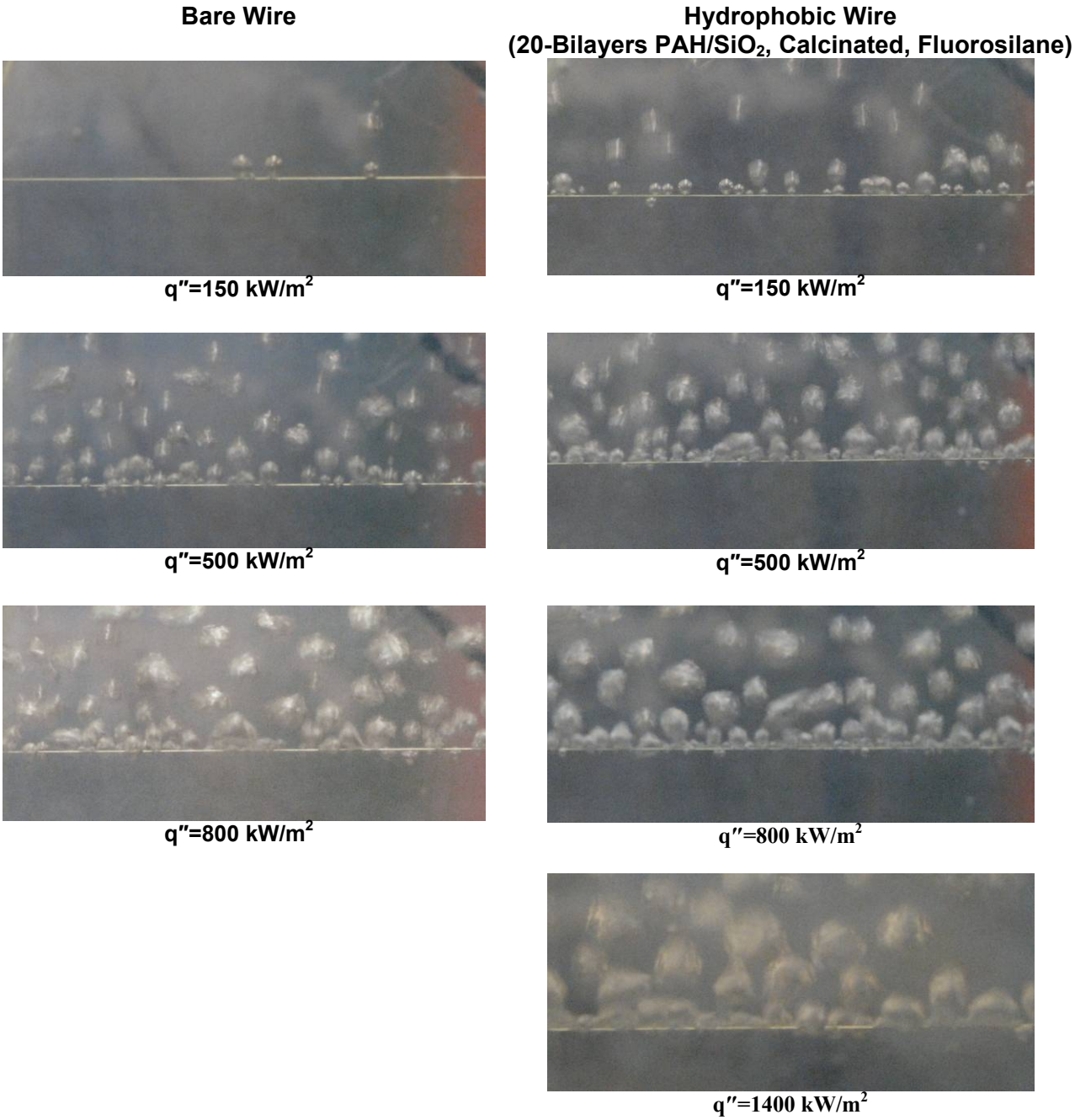

Figure 28: Boiling from a Bare Wire (Left side) and a Hydrophobic Wire Coated with 20-Bilayers of Calcinated PAH/SiO_2 and Treated with Fluorosilane (Right side).

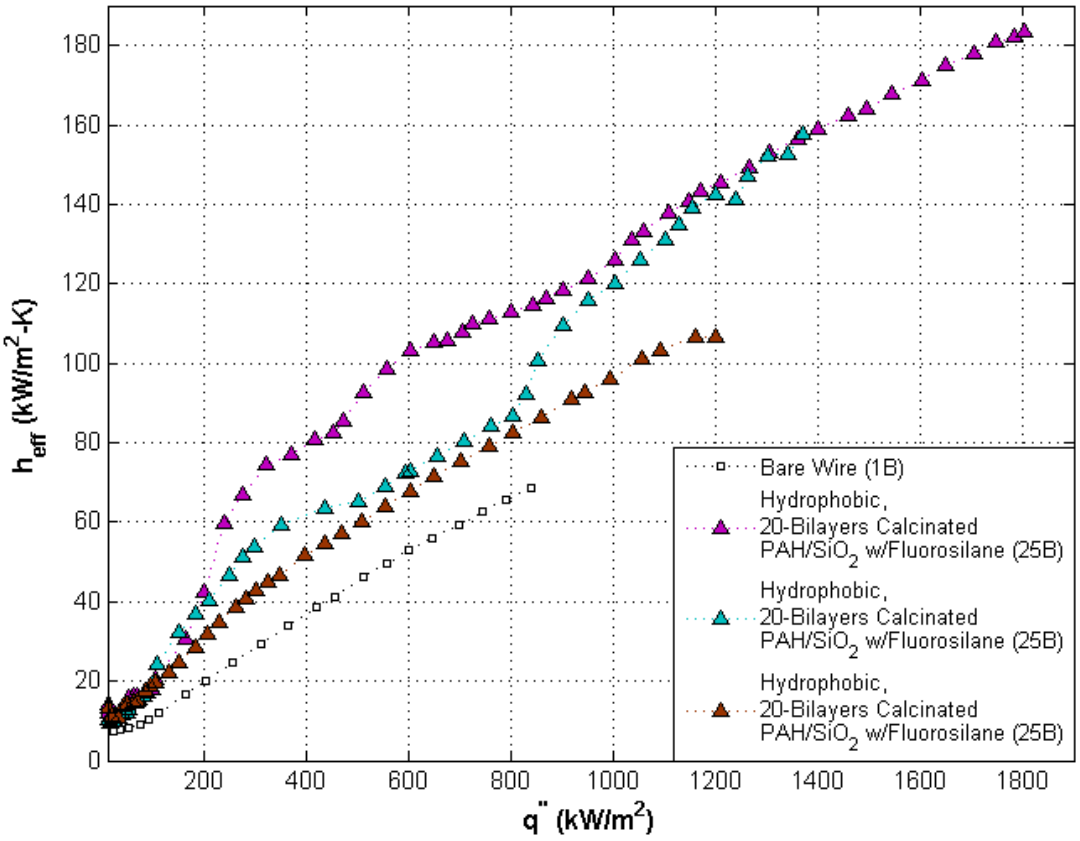

Figure 29: Effective Heat Transfer Coefficient Plotted Against Heat Flux for Boiling from the Hydrophobic Wires. The results for a bare nickel wire are plotted for reference.

3.3. Characterization of Thin-film Coatings

3.3.1. Particle Size Characterization Using Quasi-Elastic Light Scattering

The primary component of the nanoparticle thin-film coatings investigated in this study was the SiO_2 nanoparticles, deposited onto the substrate in the layer-by-layer process from a colloidal dispersion. The silica was the majority constituent, by weight, in all varieties of the PAH/SiO_2 thin-films investigated, and the silica nanoparticles were essentially the sole contributor to overall film thickness. In order to characterize the size of these silica nanoparticles, quasi-elastic light scattering, commonly referred to as dynamic light scattering (DLS), was used to measure the SiO_2 particle size distribution in suspension, i.e., prior to deposition on the substrate. DLS is a useful technique for sizing suspended particles in a dispersive medium because the measurement can be taken quickly and directly. DLS can also be used for agglomeration and settling rates of dispersed particles.

Particles that are much smaller than the wavelength of an incident photon scatter light according to Rayleigh theory. In Rayleigh scattering, the intensity of the scattered light varies by the sixth power of the particle diameter, and follows the relation below:

$$I = I_0 \frac{8\pi^4 d^6}{l^2 \lambda^4} \left(\frac{n^2 - 1}{n^2 + 1} \right)^2 (1 + \cos^2 \theta) \qquad (11)$$

Particles greater than 50 nm cannot be considered small compared to the wavelength of visible light [41], and these particles may absorb some light. Mie theory is more appropriate for describing scattering of light from particles on the same order of size as the wavelength of the light. If a particle were stationary in a dispersive medium, one would expect the observed intensity of light scattered from the particle to follow Rayleigh or Mie theory, depending on the size of the particle. However, Brownian motion results in random movement of the dispersed particle, causing the intensity to fluctuate with time. The diffusion coefficient of a particle may be related to the particle's hydrodynamic diameter by:

$$D = \frac{kT}{3\pi\eta d} \qquad (12)$$

Particle size measurement by DLS exploits the fact that larger particles diffuse in a medium more slowly than smaller particles, resulting in the period of the intensity fluctuation depending on the particle size. Polydisperse systems are more difficult to characterize, but an autocorrelation function for a polydisperse system may be considered an integral of exponentials. Software provides various methods for solving the autocorrelation function, and oftentimes it is up to the discretion of the user to determine the best method for their particular situation.

The DLS setup used to measure the silica particles in dispersion consisted of a Lexel 95 Argon Laser (514.5 nm, or green light), a sample holder with constant temperature bath, and a detector with photomultiplier tube on a goniometer. Brookhaven Instruments software processed the data to provide particle size distributions and mean diameters. Figure 30 shows the DLS setup used for the measurements. A laser is best suited for DLS measurements since the light is monochromatic and the intensity is very stable with time. For the DLS measurements, the detector was kept at a fixed 90º angle relative to the incident laser light. Figure 31 shows the results for DLS measurements of the SiO_2 colloidal dispersion used in the layer-by-layer assembly process. From two nominally identical runs, the SiO_2 number-weighted mean particle diameter was determined to be 48.6 nm. Polysciences lists the diameter of their SiO_2 nanoparticles as 50 nm [42], whereas the reported diameter of the TM-40 SiO_2 nanoparticles is 20 nm [43]. Since the prepared silica dispersion contained equal weight concentrations of both particles, one would expect the mean diameter to be slightly less. However, some loose agglomeration of the TM-40 particles may have occurred in the dispersed phase. Additionally, it is important to realize that DLS measurements assume perfectly spherical particles, whereas the TM-40 particles may not have been perfectly spherical. As it is an indirect measurement of particle size, DLS is only capable of providing the effective hydrodynamic diameter, i.e., the diameter of a spherical particle with the same diffusion coefficient. Lastly, the mean diameter in polydisperse systems is more difficult to assess using DLS, especially when the size range is large (due to intensity scattering as $\sim d^6$), and often leads to greater measurement error. Nonetheless, the silica particles appear to be small (~<50 nm) and well-dispersed.

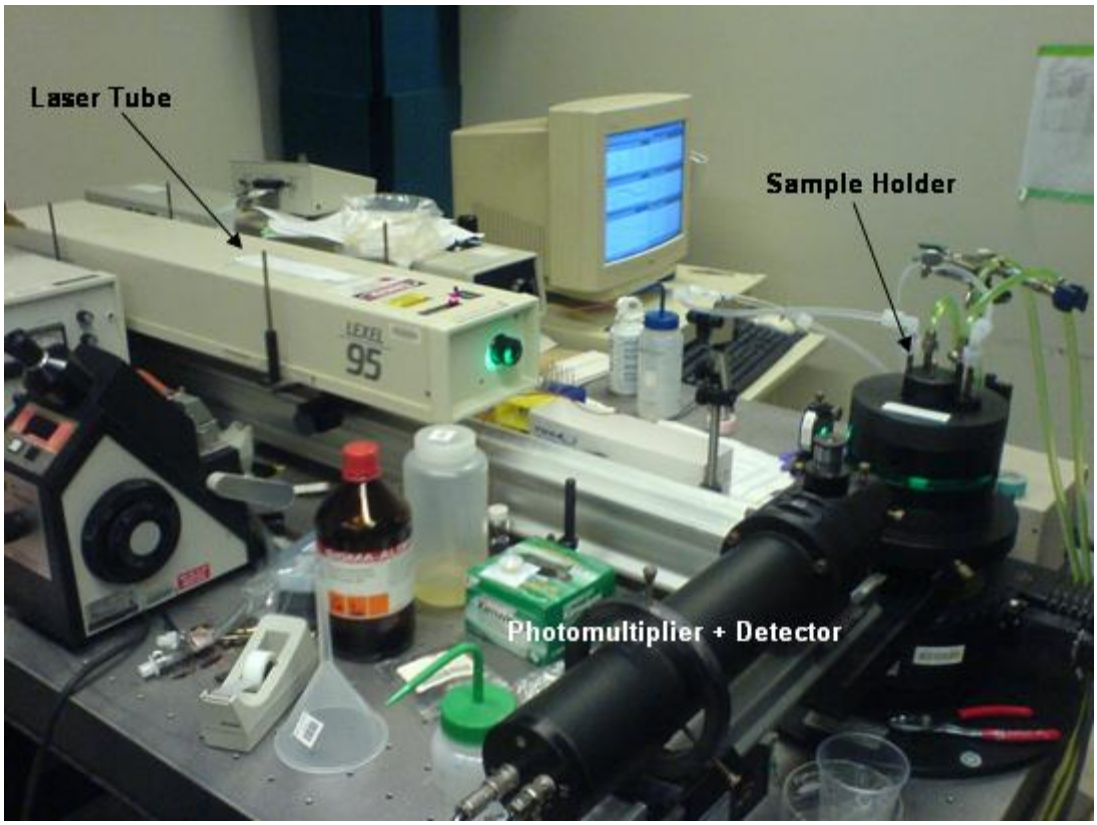

Figure 30: Dynamic Light Scattering Setup. The setup consists of an argon laser (514.5 nm) which shines monochromatic light onto a sample in the sample holder. The scattered light then passes through a pinhole at an angle of 90º relative to the incident light, where it then enters a photomultiplier tube and the detector.

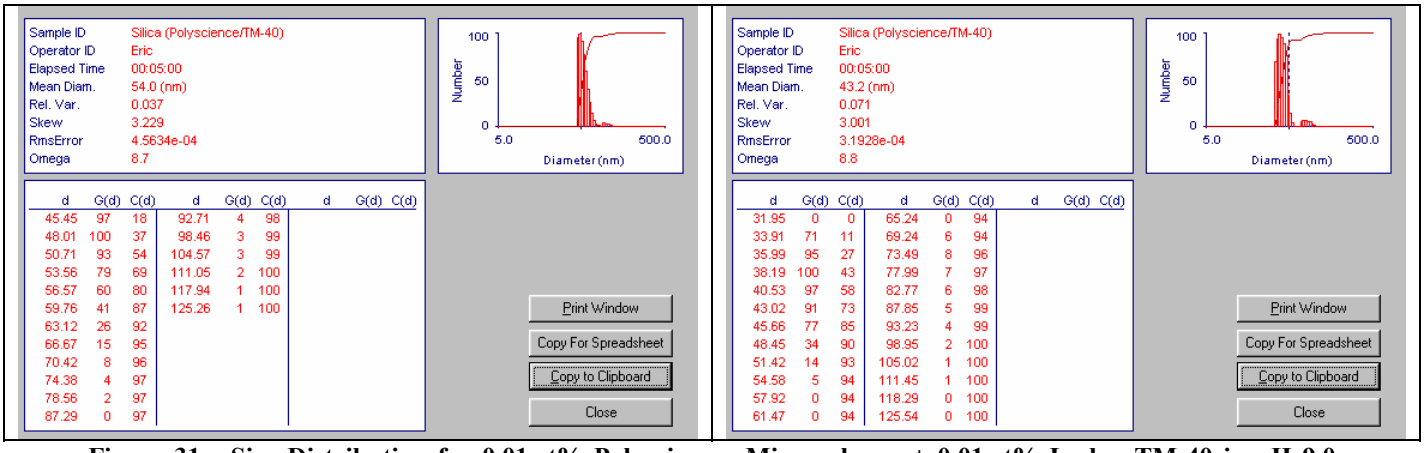

Figure 31: Size Distribution for 0.01wt% Polysciences Microspheres + 0.01wt% Ludox TM-40 in pH 9.0 Buffer. Results reported using the Exponential Sampling (EXPSAM) algorithm for deconvoluting the autocorrelation function. Run 1 is on the left, run 2 is on the right, yielding an average mean particle diameter of 48.6 nm. The plots show number density of particles versus diameter, with the diameter axis on a logarithmic scale. G(d) is the probability distribution function, and C(d) is the cumulative distribution function.

3.3.2. Surface Roughness Using Confocal Microscopy

Confocal microscopy provided measurements of the surface roughness value for stainless steel plates with PAH/SiO_2 thin-film coatings. An Olympus LEXT OLS3000 Confocal Scanning Laser Microscope measured the surface roughness of bare and coated stainless steel plates. For each test case, measurements were performed at two separate locations on the plate. Figure 32 and Figure 33 show mapped surface textures of a bare and coated stainless steel plate, respectively. Table 4 summarizes the results of surface roughness measurements for the plates. The R_a value is simply the arithmetic average of the absolute deviation in height, $|z_i|$, from the mean height over a given number of measurements. The measured roughness factor, which will be discussed in detail later, is the ratio of the actual external surface area to the geometric (projected) surface area. The roughness factor measured using this confocal technique *does not account for additional surface area from porosity effects*. The measurements indicate that there is virtually no change in the microscale surface roughness with the application of the thin-films. This implies that the nanoparticle-based coatings fill micron-scale deformities in the stainless steel surface conformally, which is expected with the LbL deposition method.

Table 4: R_a Values for Flat Plates Coated with PAH/SiO2. Typical measurement uncertainty is ±0.1 µm.

Case	R_a (µm)	Roughness Factor
Bare Plate	0.290	1.093
40 bilayers PAH/SiO_2	0.261	1.077
20 bilayers PAH/SiO_2, calcinated, fluorosilane	0.225	1.062
10 bilayers PAH/SiO_2, calcinated	0.281	1.066
20 bilayers PAH/SiO_2, calcinated	0.222	1.057
40 bilayers PAH/SiO_2, calcinated	0.268	1.062

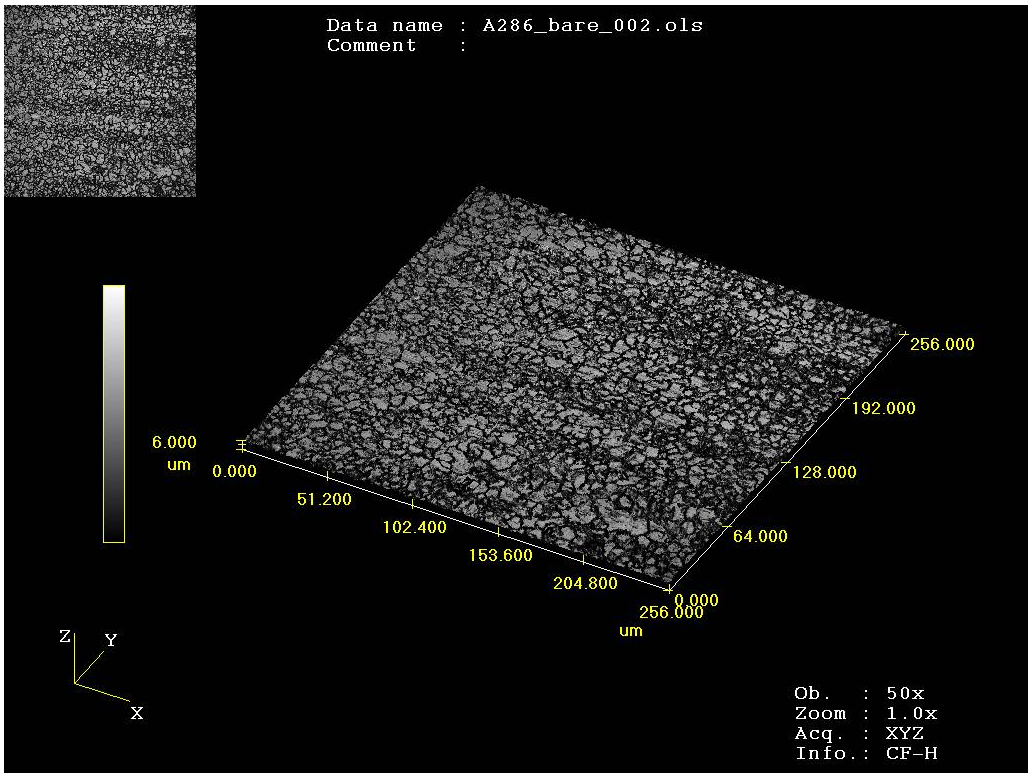

Figure 32: Surface Texture of a Bare Stainless Steel Plate Obtained Using Confocal Microscopy.

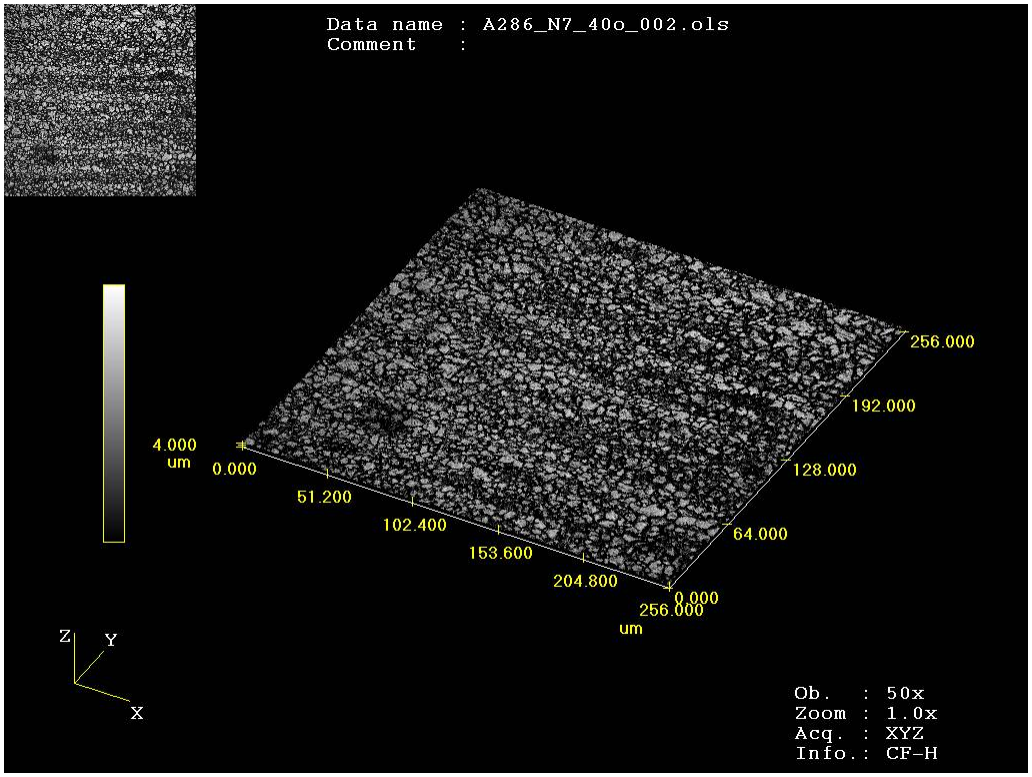

Figure 33: Surface Texture of a Stainless Steel Plate Coated with 40-Bilayers of PAH/SiO_2. On a micron scale, there is no visible change in the surface texture from that of the bare substrate.

3.3.3. Wettability Using Contact Angle Measurement

Contact angles for thin-film coatings on flat stainless steel plates are listed in Table 5. A CAM 101 contact angle analyzer and optical measurement software (KSV Instruments) measured the static and dynamic contact angles of de-ionized water on bare and coated stainless steel plates, providing insight into the wettability change by applying the PAH/SiO_2 thin-film coatings. All measurements were taken at room temperature. Contact angles are reported after 0.480 seconds for the superhydrophilic cases, as the static contact angles were so small as to be immeasurable (less than 3º). For the hydrophobic surfaces, static advancing (advanced) and static receding (receded) contact angles were measured using the technique outlined in Figure 34. Although it is possible to measure dynamic advancing and dynamic receding contact angles by rolling a droplet down a tilted surface, the measurement is not as straightforward, as these contact angles depend on the velocity. Note that starting with the same calcinated PAH/SiO_2 coating, dramatically different contact angles can be achieved by altering the chemical constituency of the top surface.

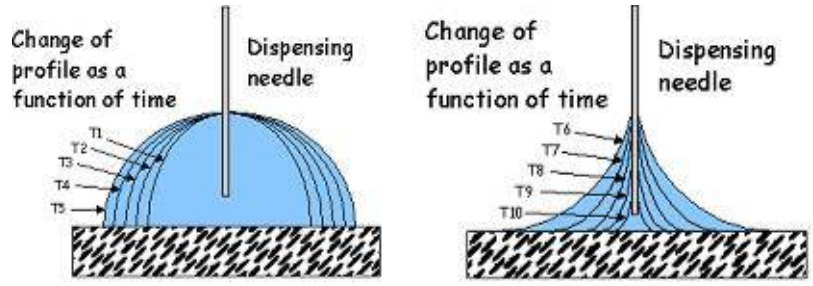

Figure 34: Technique for Measuring Static Advancing Contact Angle (Left) and Static Receding Contact Angle (Right). The static advancing and static receding contact angles are the apparent angles immediately prior to motion of the three-phase contact line. ***Source: Ref. [44], reproduced with permission of KSV Instruments, © 2009.***

The static equilibrium contact angle is expected to be between the static receding contact angle and static advancing contact angle [45]:

$$\theta_R < \theta_{eq} < \theta_A \qquad (13)$$

This is observed for the measurements on the hydrophobic surface. For the hydrophobic surface, an unusually large contact angle hysteresis was observed, with receding contact angles as low as 19º. The bare stainless steel surface exhibited some hysteresis in the contact angle (θ_A=90º, θ_R=50º), but no where near the magnitude observed for the hydrophobic surface. Advanced and receded contact angles were not measured on hydrophilic and superhydrophilic surfaces, as the highly wettable surfaces wicked the water away from the syringe. Nonetheless, the contact angle hysteresis on these surfaces is expected to be small, with receded contact angles of ~0º and advanced contact angles near 0º on superhydrophilic surfaces. Tadmor provides an equation which can be used to relate the equilibrium, advancing, and receding angles [46]. Figure 35 depicts the various contact angles, highlighting the stark differences in wettability that can be achieved with the PAH/SiO_2 coatings.

Since contact angle depends on the chemical constituency of the coating and not the substrate, one would expect similar wetting properties for coatings on other substrates. However, since the coating is conformal, one should not neglect the roughness of the substrate, as it could have an effect on the contact angle. Since expected contact angles for smooth nickel are similar to those for stainless steel, typically between 60º and 80º [47, 48], changes in contact angle for a smooth nickel surface coated with these thin-film coatings (i.e., as on the nickel wires used in boiling tests) should be similar to changes seen for stainless steel plates.

Table 5: Summary of Measured Contact Angles for Flat Stainless Steel Plates. Typical measurement uncertainty is ±5º.

Surface	Static	At t=480ms
Clean surface	84º	Not Measured
40 bilayers PAH/SiO_2	21º	Not Measured
10 bilayers PAH/SiO_2, calcinated	<3º	11º
20 bilayers PAH/SiO_2, calcinated	<3º	12º
40 bilayers PAH/SiO_2, calcinated	<3º	11º
20 bilayers PAH/SiO_2, calcinated fluorosilane	141º	Not Measured

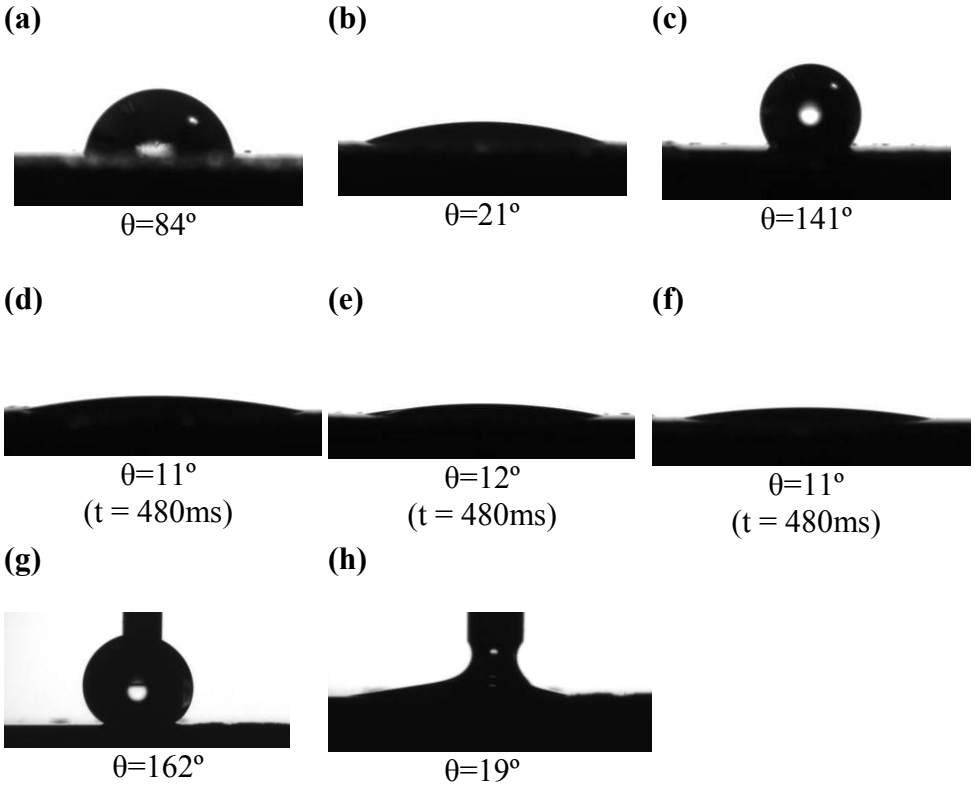

Figure 35: Static Contact Angles of Water on Stainless Steel Plates for (a) clean surface, (b) surface coated with 40 bilayers of PAH/SiO_2, and (c) surface coated with 20 bilayers of PAH/SiO_2, calcinated, and treated with fluorosilane. Contact angles after 480 ms on plates with calcinated PAH/SiO_2 for (d) 10 bilayers, (e) 20 bilayers, and (f) 40 bilayers. Advanced (g) and receded (h) contact angles for surface coated with 20 bilayers of PAH/SiO_2, calcinated, and treated with fluorosilane.

3.3.4. Coating Thickness and Porosity Using SEM

Images were obtained for nickel wires coated with PAH/SiO_2 thin-films using a FEI/Philips XL30 FEG Environmental Scanning Electron Microscope. SEM images show qualitatively that the coatings are smooth and homogenous on a micron-scale. Estimates of coating thickness can also be obtained from these images. As seen in Figure 36, SEM images reveal that 10-bilayer PAH/SiO_2 coatings are of the order of 300 nm thick, 20-bilayer coatings are of the order of 600 nm thick, and 40-bilayer coatings are of the order of 1 μm thick. Therefore, coating thickness is nearly proportional to the number of bilayers. These data correspond closely to data previously collected for multilayers of the same composition deposited on glass substrates. On glass, the per-bilayer thickness was 28 nm, constant up to at least 40 bilayers [15]. 28 nm per bilayer appears to be a reasonable value for the PAH/SiO_2 coatings investigated in this study based off DLS measurements of particle size, considering that nanoparticle layers are likely to intermesh.

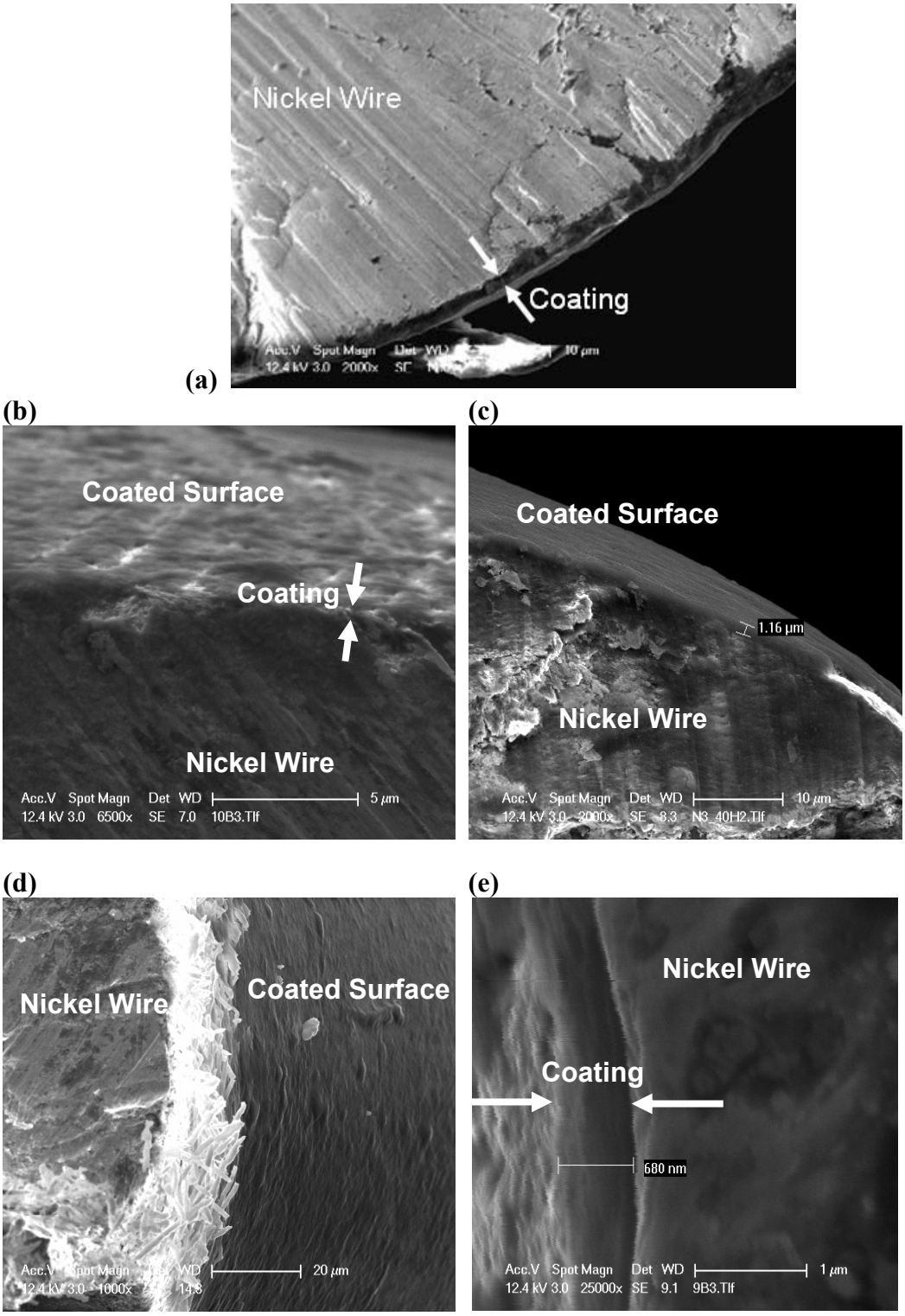

Figure 36: SEM Images of 0.01" Nickel Wires Coated with PAH/SiO_2 Thin-films. Wires were clipped and then oriented diametrically to view the coating thickness. (a) Nickel wire coated with 40-bilayers PAH/SiO_2, (b) Nickel wire coated with 10-bilayers PAH/SiO_2 and calcinated, (c) Nickel wire coated with 40-bilayers PAH/SiO_2 and calcinated, (d) & (e) Nickel wire coated with 20-bilayers of PAH/SiO_2 and calcinated. Note that in some cases, the coating did not cut cleanly (e.g. image (d)), making estimates of coating thickness more difficult.

Unfortunately, the XL30 was not capable of obtaining high resolution images on length scales under a few microns for the coated surfaces. A Supra 55VP Field Emission Scanning Electron Microscope was used to investigate the nanoscale surface texture. As seen in Figure 37, the coating is nanoporous, with cavity sizes on the order of 100 nm or less. In Figure 37, one can clearly distinguish between the larger Polysciences 50 nm silica microspheres, and the smaller 20 nm TM-40 silica particles. Although the DLS data indicates that these smaller 20 nm particles were not present, they may have formed loose agglomerates in suspension, thereby effecting a larger measured diameter by the DLS.

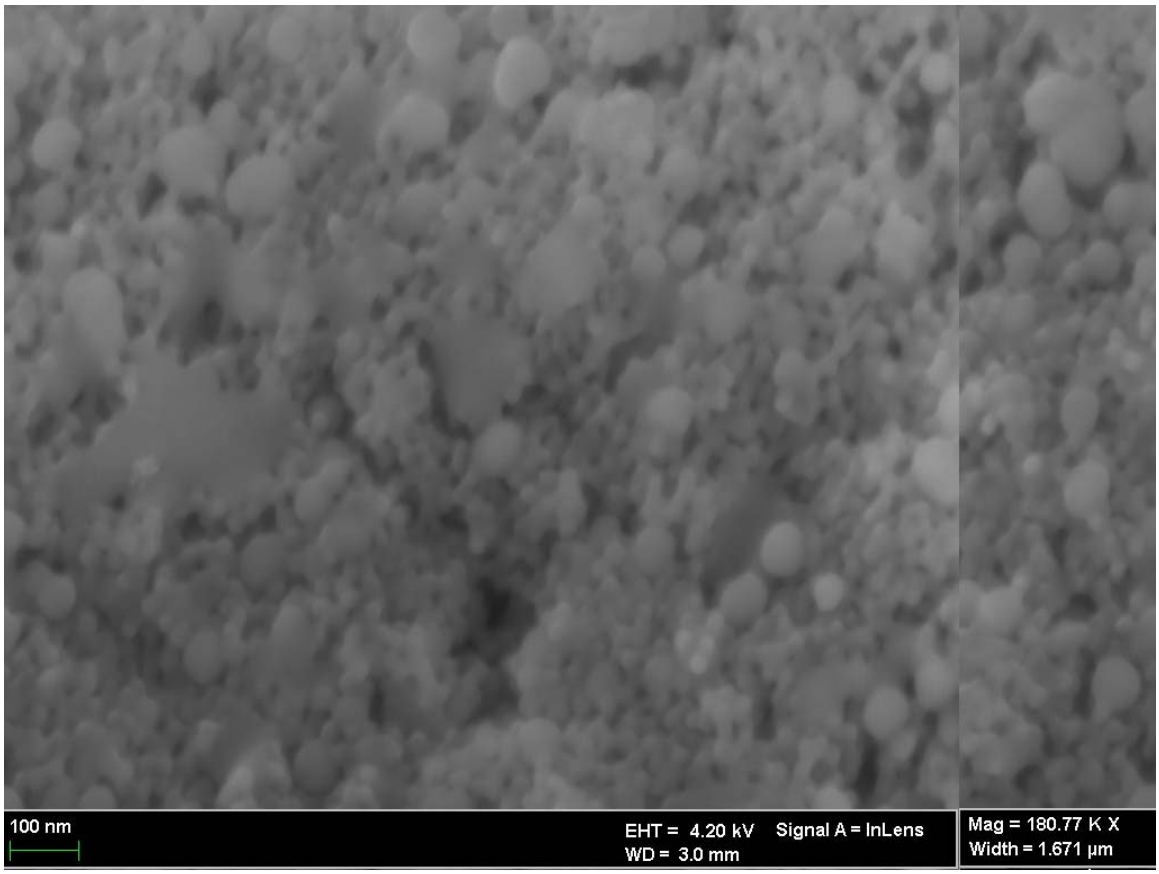

Figure 37: Highly magnified View of a 20-bilayer PAH/SiO_2 Calcinated Coating on a Stainless Steel Substrate. Note that the coating is very porous at the nanoscopic level, with both large spherical SiO_2 particles (~50 nm) and smaller SiO_2 particles (~20 nm) being constituents of the film. ***Image taken by Dr. Hyung Dae Kim*.**

3.3.5. Coating Thickness and Porosity Using Ellipsometry

Ellipsometry is a powerful optical technique that is widely used for the characterization of SiO_2 thin-films in the microelectronics industry [49]. Ellipsometric techniques are used to measure various properties of thin-films, including refractive index, thickness, and porosity. Common ellipsometric setups use an incident beam of polarized light at a fixed angle, which then reflects off the surface of interest into a detector at a fixed angle. The change in polarization of the reflected light can then be used to determine properties of the thin-film. Ellipsometric techniques are designed for differential analysis, i.e., one needs to measure the change in polarization from a clean, bare surface to establish a baseline measurement. Using the established baseline, one may then measure the change in polarization obtained from application of a thin-film of nanoparticles.

Measurements of film thickness and porosity were attempted for PAH/SiO_2 thin-films on stainless steel plates using ellipsometric techniques. Unfortunately, the reflectivity on these surfaces was so low that an appreciable signal could not be obtained at the detector (leading to an unacceptably high signal-to-noise ratio), despite varying source and detector angles. It was suspected that the reflection off the matte surface was too diffuse for this type of measurement, which is not surprising since typical substrates for thin-films analyzed with ellipsometry are glass slides or silicon wafers. Although some film thickness data were obtained for the stainless steel substrates, uncertainty values were on the order of the measurement itself, and thus the results were discarded. For future measurements, the author suggests that the metal surface be finely polished prior to application of the thin-films, in order to increase the reflectivity. Ellipsometry results from prior studies of similar coatings on glass substrates are useful in estimating coating thickness and porosity for PAH/SiO_2 thin-films on nickel wires and stainless steel plates used in this study. Bravo et al. observe linear growth of PAH/SiO_2 (50 nm+20 nm particles) films up to 40-bilayers, indicating a per bilayers thickness of 28 nm, with the calcination process causing a negligible change in the overall coating thickness [15]. The per bilayers thickness measured by Bravo implies that the 10-bilayer coatings investigated in this study will be 280 nm thick, 20-bilayer coatings will be 560 nm thick, and 40-bilayer coatings will be 1.12 μm thick. These thicknesses agree well with the rough estimates attained using SEM. Lee et al. measure porosity values of ε=0.42 for thin-films consisting of alternating bilayers of 16 nm/8 nm SiO_2 particles, ε=0.49 for thin-films consisting of alternating bilayers of

16 nm/24 nm SiO_2 particles, and ε=0.453 for calcined thin-films consisting of 7 nm TiO_2/22 nm SiO_2 particles [11,13]. Note that these films were prepared using similar techniques as the films in this study, and were prepared in the same laboratory; thus their porosity measurements are representative of expected porosity values.

If one assumes that we have dense random packing [50] of hard, spherical SiO_2 particles, it is possible to predict the porosity of the PAH/SiO_2 thin-films applied to nickel and stainless steel substrates in this study. From the SEM micrograph shown in Figure 37, the particles appear to be essentially spherical. Additionally, we will assume the particles adsorbed onto the surface constitute a bimodal distribution of 20 nm and 50 nm SiO_2 particles. Lastly, we will assume that the volume fraction of each particle type (50 nm and 20 nm) absorbed onto the surface is equivalent, since the dispersed aqueous volume fraction is equivalent. Using results of simulations from Bezrukov et al. for packing of bimodal distributions of hard spheres of appropriate size ratio [51], one predicts that the porosity for dense random packing of 50 nm + 20 nm SiO_2 particles will be $\boldsymbol{\varepsilon \approx 0.39}$. One must consider that in Bezrukov's model, gravity is the packing force, whereas in our case it is an electrostatic interaction. Nonetheless, even though this porosity prediction for the calcined PAH/SiO_2 coatings used in this study is highly approximated, is seems to be reasonable when compared to measured porosity data for other nanoparticle thin-films.

4. THEORETICAL ASPECTS OF THE EFFECT OF THIN-FILM COATING ON NUCLEATE BOILING HEAT TRANSFER AND CRITICAL HEAT FLUX

4.1. Review of Effects of Surface Structure and Chemical Constituency on Wettability

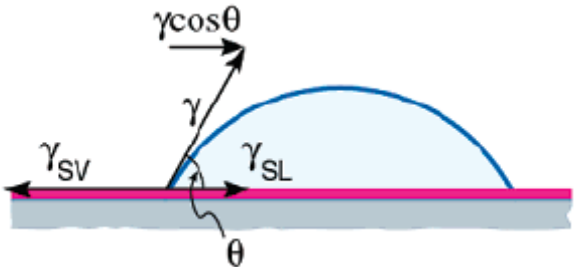

Figure 38: Two-Dimensional Representation of the Interfacial Forces Acting On a Sessile Drop. Here γ=σ, the surface tension (or liquid-vapor interfacial tension). ***Source: Ref. [46], reproduced with permission of the American Chemical Society, © 2004.***

Previous work on boiling heat transfer of nanofluids by Kim et al. [3] has shown that porous deposits of nanoparticles on boiling surfaces lead to a substantial increase in the surface wettability, as measured by the contact angle of water on the surface. Figure 35 shows that a wide range of contact angles can be achieved with the nanoparticle thin-film coatings tested in this study. Figure 38 illustrates the forces acting at the triple contact line of a sessile drop on a flat surface. From a force balance, the intrinsic contact angle may be determined using Young's equation:

$$\cos\theta_I = \frac{\gamma_{sv} - \gamma_{sl}}{\sigma} \qquad (14)$$

Here (γ_{sv}-γ_s) represents the adhesion tension for the liquid/solid combination, and σ is the surface tension of the liquid. However, if a surface is not perfectly flat, one must account for the surface roughness, as described by Wenzel [52], in order to determine the apparent contact angle:

$$\cos\theta = r\cos\theta_I \qquad (15)$$

Here *r* is the roughness factor, which Wenzel defined as the total surface area divided by the projected area. Note that, in the absence of line tension, the local contact angle on a rough surface will be exactly equal to the intrinsic contact angle for that material.

For very porous materials, the *r* term should be modified to account for effects of porosity. Interconnected pores beneath the external surface increase the effective wetted area, thereby increasing the apparent wetting through wicking. Lee corroborates this, explaining that for very porous materials, the *r* term becomes very large, implying that the surface will have an apparent contact angle of ~0º if the intrinsic contact angle is less than 90º, or ~180º if the intrinsic contact angle is higher than 90º [11]. This happens to be the case for the calcinated PAH/SiO_2 coatings. Although the higher adhesion tension associated with silica certainly improves wettability over the bare metal substrates, it is the nanoporous nature of the coatings that leads to the superhydrophilicity and wettability. As a comparison, 22º static equilibrium contact angles in air have been reported for de-ionized water on ultra-smooth (0.3 nm roughness) amorphous silica surfaces [53]. Cebeci et al. [14] attribute the superhydrophilicity of the PAH/SiO_2 multilayers to the 3D nanoporous network of controlled thickness and the resulting nanowicking of water into that network. They also note that there is a minimum critical film thickness needed to obtain the super wetting behavior, likely due to a critical volume capacity.

For the non-calcinated PAH/SiO_2 coatings, the contact angle is reduced relative to the bare metal, but not to the same extent as with the calcinated coatings. This can be attributed to the presence of PAH in the multilayers, which is slightly hydrophobic in nature. Therefore, removal of the PAH during calcinations increases the hydrophilicity of the coating. Nonetheless, significant improvement in wettability is still observed (θ=84º to θ=21º) due to the effect of the silica even if the PAH is not burned out. Following calcination, a contact angle of about 10º is observed 480 ms after droplet contact, with nearly perfect wetting after several seconds.

The hydrophobic surface is perhaps the most fascinating, as the hydrophobic behavior is achieved from the superhydrophilic coating through only slight changes in surface chemistry. As discussed, wettability is controlled by both the surface energy (the adhesion tension) and the geometry or texture of the surface (the *r* term in equation (15)). The hydrophobic coating, while maintaining the same geometry and surface texture as the superhydrophilic coating, experiences a substantial change in wettability by changing the surface adhesion tension through application of the fluorosilane. The wetting behavior of the hydrophobic surface is also characterized by a

large contact angle hysteresis, with an advancing angle around 160º and a receding angle around 20º. Note that despite the hydrophobic chemical constituency, the wetting of water on the hydrophobic coating remains in the Wenzel state, in which water fills the nano- and micro-cavities on the surface. Were the coating in the Cassie-Baxter state, water droplets would sit completely above the surface over air pockets, thereby leading to a low contact angle hysteresis and roll-off characteristics, which are not observed. For the hydrophobic coatings investigated in this study, the nanostructure, combined with the chemical vapor deposition of fluorosilane, leads to the high static advancing contact angles and large contact angle hysteresis.

Since bubble nucleation and CHF are dynamic processes, dynamic advancing and receding contact angles are more appropriate in relating wettability to the boiling processes. Bernardin et al. describe the distinct differences between dynamic and static angles [54]. Unfortunately, measurement of the dynamic advancing and dynamic receding contact angles is not as straightforward as static measurements, and depend on the velocity of the three point line. Regardless, advanced and receded contact angles provide useful information regarding wettability, and can be closely correlated to the dynamic advancing and dynamic receding contact angles. Although temperature effects may also influence contact angle and wettability, and should be considered, experimental results by Bernardin and Mudawar showed that the contact angle for water on aluminum between room temperature and saturation at atmospheric pressure [54].

4.2. Wettability and Bubble Nucleation

As seen in Figure 12, for a given heat flux, the hydrophobic surface has the greatest enhancement in the nucleate boiling heat transfer coefficient, up to about 100%, whereas the hydrophilic surface suffers a slight degradation, ~10%, compared to the base case. The superhydrophilic surface, however, shows substantial degradation of about 50% in the heat transfer coefficient, only recovering at very high heat fluxes.

Research in the field of boiling heat transfer indicates that entrapped gas (vapor or air) in surface cavities leads to the initial nucleation process [55]. Therefore, cavities that are not completely flooded by liquid water can promote bubble nucleation at lower wall superheats. Young and Hummel obtained higher nucleate boiling heat transfer by adding PTFE to localized regions of a boiling surface, resulting in better nucleation [56]. Enhancement in boiling heat

transfer from the PAH/SiO_2 multilayers with hydrophobizing treatment can be explained in a similar manner. The surface structure and chemical constituency of the calcinated PAH/SiO_2 multilayers with vapor-deposited fluorosilane result in a surface with a high advancing and static contact angle This implies that cavities on the surface will not be flooded, but rather, filled with air and vapor. This in turn leads to preferential nucleation from these cavities at lower wall superheats, explaining the considerable enhancement in the nucleate boiling heat transfer coefficient.

On an idealized boiling surface, the degree to which a cavity will be flooded depends on the groove angle, 2γ, and the contact angle of the liquid with the side of the cavity. The situation can be treated as a liquid front advancing over the cavity, and therefore, the relevant parameters for initial entrapment of gas in the cavity will be the dynamic advancing contact angle [57, 58, 59]. Although this model is overly simplified for our complex coatings, it is useful in estimating relative entrapment of gas on our different surfaces. Therefore, the higher advancing contact angle, the higher the *initial* radius of the nucleus. Upon incipience, we can imagine the microcavity dynamics involving the recession of a liquid meniscus, and here the receding contact angle will be relevant. Nonetheless, the advancing contact angle is important for enhancing the nucleate boiling heat transfer coefficient as initial entrapment of vapor will substantially reduce the initial activation temperature resulting in a higher nucleation site density leading to lower wall superheats, as demonstrated by the results.

For wires coated with the hydrophilic and superhydrophilic surfaces, one may infer that cavities are more likely to be flooded when compared to the wires with the hydrophobic coating. Additionally, cavities that do become active will require higher superheats to nucleate. For example, Wang and Dhir predicted that surfaces with higher wettability will display poorer nucleate boiling heat transfer, whereas surfaces with reduced wettability will exhibit better nucleate boiling heat transfer, and provided a correlation to predict the nucleation site density as a function of contact angle at a fixed wall superheat [60]:

$$N_a(sites/cm^2) \propto (1-\cos\theta\ )D_c^{-6.0} \qquad (16)$$

where N_a is the active nucleation site density and D_c is the cavity diameter.

Equation (16) predicts a higher nucleation site density and thus a higher heat transfer rate for higher contact angle, which is in agreement with observations, illustrated by photographs of boiling from the different surfaces. However, one cannot predict the boiling heat transfer coefficient solely from the knowledge of the nucleation site density because parameters such as bubble diameter and bubble departure frequency, which affect nucleate boiling heat transfer, are also altered by application of the thin-film coatings but were not measured in our experiments.

The boiling behavior of nickel wire with the calcinated PAH/SiO_2 multilayers, shown in Figure 12, is particularly unusual due to the reversal of the boiling curve at high heat fluxes. Figure 26 shows qualitatively that there are very few active nucleation sites at a heat flux of 500 kW/m^2. However, at even higher heat fluxes, a significant number of nucleation sites appear, cooling the wire substantially, resulting in the reversing trend observed in the boiling curve. This late activation of nucleation sites results in high wall superheats for the wire. The situation exhibited by the superhydrophilic wire is similar to that described by Carey for boiling experiments seeking to eliminate trapped gas in surface cavities. Such experiments displayed very high superheats for the initiation of nucleation, but after nucleation was initiated, the superheat required to sustain bubble formation dropped to a lower value [55]. The superheat required for nucleation falls due to the refilling of cavities with vapor upon nucleation.

For the superhydrophilic wires, one may presume that the high wettability leads to the majority of cavities being flooded at the start of each test, since $\theta_A<2\gamma$. This, in turn, requires higher wall superheats to initiate nucleation. However, upon nucleation, vapor becomes entrapped in the cavities, lowering the required superheat. The hysteresis tests shown in Figure 24 and Figure 25 support this hypothesis.

4.3. Critical Heat Flux

4.3.1. Review of Existing Theories

The exact mechanism and parameters affecting the boiling crisis, or CHF, remain unclear to this day. For many years, the hydrodynamic instability theory, developed by Zuber [61], has been widely used to predict the departure from nucleate boiling or CHF. The Kutateladze-Zuber correlation, developed by Kutateladze through dimensional analysis [62], and Zuber through his hydrodynamic instability analysis [61], is shown in simplified form below:

$$q''_{CHF} = K\rho_g h_{fg}\left[\frac{g\sigma(\rho_f - \rho_g)}{\rho_g^2}\right]^{1/4} \qquad (17)$$

where K is a constant that only depends on the geometry of the system. For an infinite flat plate, K=0.131. The hydrodynamic theory has been scrutinized in recent years because it does not account for surface characteristics such as wettability. Recent work by Kim et al. [3], among others, clearly revealed the effects of surface parameters on CHF. The hydrodynamic instability theory fails to predict the enhancement associated with modified surfaces, such as those created by the boiling deposition of nanoparticles. The CHF enhancement presented here for pool boiling of nickel wires coated with nanoparticle thin-films also demonstrates the limitation of this theory.

Two popular theories, which do include dependence on surface characteristics such as wettability, are the macrolayer dryout theory [63, 64] and the hot/dry spot theory [65]. For the macrolayer dryout theory, the dependence of CHF on surface wettability is tied to the thickness of a liquid macrolayer covering the surface between vapor bubbles. The equivalent thickness of the macrolayer can be calculated by:

$$\delta_e = r_b\left[\cos\theta - \frac{\pi}{12}(3\cos\theta - \cos^3\theta)\right] \qquad (18)$$

The equivalent thickness from equation (18) is directly proportional to the dryout time of the liquid macrolayer. CHF occurs if the liquid macrolayer vaporizes completely. As contact angle decreases, the equivalent liquid macrolayer thickness increases, so CHF will also increase proportionally. The macrolayer dryout theory qualitatively captures the wettability effect on CHF for hydrophilic surfaces.

The hot/dry spot theory predicts that CHF will occur at a nucleation site when rewetting is unable to occur at a growing hot spot. Therefore, increasing the surface wettability would allow for easier rewetting of hot spots, thereby delaying CHF. Theofanous and Dinh [65] give the following expression for the critical heat flux based off the hot/dry spot theory:

$$q''_{CHF} = \kappa^{-1/2} \rho_g h_{fg} \left[\frac{g\sigma(\rho_f - \rho_g)}{\rho_g^2} \right]^{1/4} \qquad (19)$$

Equation (19) is almost identical to the Zuber equation, except that the leading constant depends on surface characteristics such as wettability. Kim et al. [3] derived the following analytical expression for κ:

$$\kappa = \left(1 - \frac{\sin\theta}{2} - \frac{\pi/2 - \theta}{2\cos\theta} \right)^{-1/2} \qquad (20)$$

Using Eqs. (19) and (20), one would also expect an increase in CHF with a reduction in contact angle. However, equation (20) is only applicable for $\theta \leq 90^{\circ}$.

4.3.2. Importance of the Dynamic Receding Contact Angle on CHF

A pool boiling CHF model proposed by Kandlikar involves a force balance of a quasi-static bubble on a heated surface, where the force due to momentum change at the bubble interface is an important parameter in determining CHF [66]. Kandlikar formulated a prediction for CHF from this model, which can be applied to both hydrophilic and hydrophobic surfaces:

$$q''_{CHF} = \rho_g{}^{1/2} h_{fg} \left(\frac{1 + \cos\beta}{16} \right) \cdot \left[\frac{2}{\pi} + \frac{\pi}{4}(1 + \cos\beta)\cos\phi \right]^{1/2} \left[\sigma g (\rho_f - \rho_g) \right]^{1/4} \qquad (21)$$

where β is the dynamic receding contact angle for the surface-fluid combination. Figure 39 illustrates Kandlikar's model.

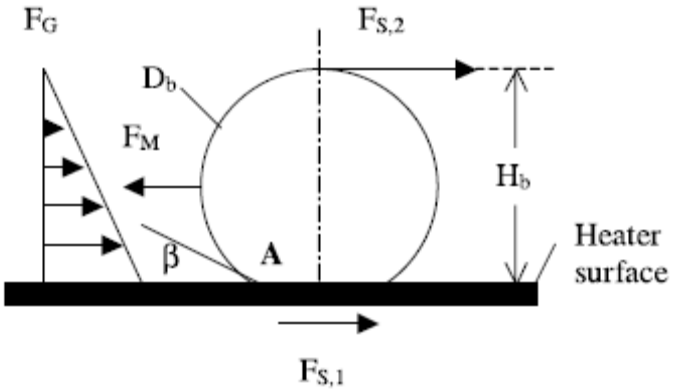

Figure 39: Force Balance on a Vapor Bubble Growing in a Liquid Over a Heated Surface. β is the dynamic receding contact angle, F_M is the force on the bubble due to momentum change. ***Source: Ref. [66], reproduced with permission of Elsevier, © 2002.***

It is important to note that all wires coated with nanoparticle thin-films demonstrated CHF enhancement. However, one incongruity arises from the results of this study when compared with the CHF predictions of the hot/dry spot theory and Kandlikar's model, as shown in Table 6. Varying the coating thickness yields significant differences in CHF enhancement, while the measured contact angles for these coatings were virtually identical. Both the macrolayer dryout theory and the hot/dry spot theory predict a direct dependence based on surface contact angles.

For the calcinated, superhydrophilic coatings, the only variable of the 10-bilayer, 20-bilayer and 40-bilayer cases is coating thickness. This implies that the total pore volume increases linearly with increasing thickness. Although the pore volume is closely tied to the surface wettability, test results clearly indicate that the thickness of the porous layer, in addition to the apparent contact angle, should be accounted for when evaluating parameters that affect CHF.

Although the CHF enhancement associated with the hydrophobic coating seems counterintuitive, one must recognize that the hydrophobic coating is characterized by a large contact angle hysteresis. The hydrophobic coating has static and advanced contact angles of about 140º and 160º, respectively, but the static receding contact angle is only about 20º. Kandlikar explains that the dynamic receding contact angle is the parameter influencing the dryout phenomenon [66, 67]. The static receding contact angle can be closely correlated to the dynamic receding contact angle. Therefore, for low receding contact angles, one would expect a

higher CHF, which is exhibited with the hydrophobic coating. Therefore, the hydrophobic thin-film coating appears to be the ideal surface treatment for augmenting heat transfer, i.e., offering a large advancing contact angle to enhance the nucleate boiling heat transfer coefficient, while possessing a small receding contact angle to enhance the CHF.

Table 6: Comparison of Measured and Predicted CHF Enhancements for Various Thin-Film Coatings. Contact angles measured on flat plates are extended to the wire CHF results. In applying equation (21), receding contact angles for the hydrophilic and superhydrophilic cases were assumed equal to the equilibrium angle, which is reasonable given the low contact angle hysteresis.

Test Case	Measured CHF Enhancement	Predicted CHF Enhancement Eq. (19)	Predicted CHF Enhancement Eq. (21)
10 bilayers PAH/SiO_2, calcinated	44%	225%	117%
20 bilayers PAH/SiO_2, calcinated	63%	224%	116%
40 bilayers PAH/SiO_2, calcinated	101%	225%	117%
40 bilayers PAH/SiO_2	84%	114%	110%
20 bilayers PAH/SiO_2, calcinated, fluorosilane	69%	---	111%

>><<<<<<<<<<<<<<<<<<<<<<<<<<<<<<<<

SECTION II:
NANOPARTICLE-BASED ENHANCEMENT OF POOL BOILING HEAT TRANSFER IN LOW GLOBAL WARMING POTENTIAL DIELECTRIC FLUIDS

5. BACKGROUND ON LOW GLOBAL WARMING POTENTIAL DIELECTRIC FLUIDS FOR ELECTRONICS COOLING

5.1. Two-phase Cooling of Electronic Devices

The cooling of microelectronics, power electronics, and other high power density devices poses a continuing challenge for thermal engineers. Considering that the performance of electronic devices degrades rapidly with increasing temperature, it is crucial that proper thermal management techniques are integrated into the design of electronic systems. Large multi-chip modules and power electronics can dissipate thousands of watts, and as packaging becomes smaller, this can equate to heat fluxes of 3 MW/m^2 and higher at the die surface [68]. Such high heat fluxes necessitate large heat sinks to increase the surface area along with other thermal management techniques. Air cooling is often insufficient to maintain proper operational temperatures in high power density devices such as insulated-gate bipolar junction transistors (IGBT's), even when coupled with large conduction heat sinks and forced convection setups. Indirect cooling using water offers higher cooling capacities than air cooling alone, but still requires large heat exchangers and creates corrosion issues which could lead to failure of the electronic device. Direct immersion cooling of electronic devices has been a popular alternative to air and indirect water cooling due to the much higher heat transfer coefficient without the need for large heat sinks attached to the electronic device.

Bergles [69], Chu [70], and others have long recognized the difficulties associated with the cooling of electronic devices. The use of dielectric fluids to cool electronics, both directly and indirectly, has been researched since the late 1960's [70]. More recently, there has been a re-emergent interest in electronics cooling using dielectric fluids due to development of advanced power electronics for the renewable energy field. Photovoltaic cells, wind turbines, electric vehicles, and hybrid-electric vehicles all require high density power electronics for rectifying or otherwise converting electrical energy to other forms [71, 72]. Two-phase direct immersion cooling offers high heat transfer coefficients coupled with the size reduction of secondary heat exchangers or heat sinks. Figure 40 shows one such application of two-phase immersion cooling, in which an IGBT die is immersed in a dielectric fluid. The primary challenge of two-phase immersion cooling is finding a fluid with good dielectric properties, good thermophysical properties, low toxicity, low flammability, low environmental impact, long-term stability, and acceptable chemical compatibility with electronic materials. The search for an

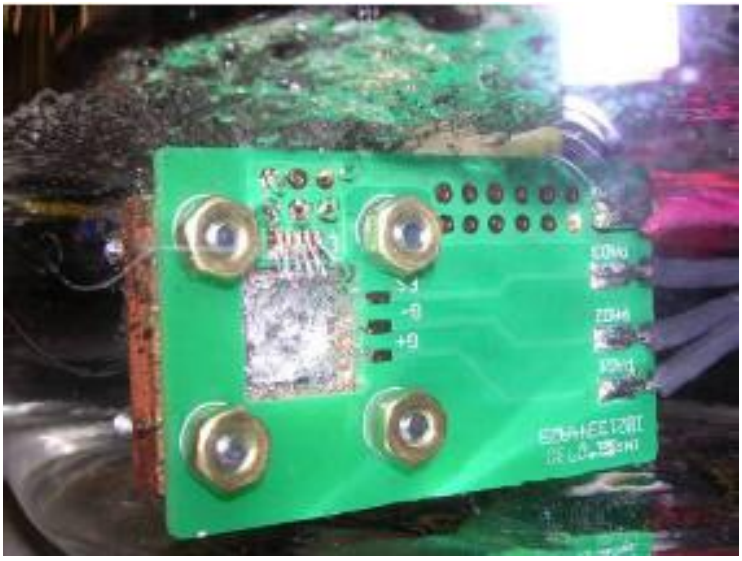

Figure 40: Dual Side Immersion Cooling of an IGBT Die Soldered to a Copper Boiler in a Hydrofluoroether Working Fluid. ***Reproduced with permission of Phil Tuma, 3M Electronics Markets Materials Division, 2008.***

acceptable fluid has often led to significant compromises in reducing environmental impact or in fluid performance.

Many chlorofluorocarbons (CFC's) and hydrochlorofluorocarbons (HCFC's) are suitable for power electronics cooling applications, but have a significant environmental impact, as they are ozone-depleting. The 1987 Montreal Protocol enacted legislation essentially banning all CFC's and requiring the phasing out of HCFC's [73]. Hydrofluorocarbons (HFC's) have replaced CFC's and HCFC's for nearly all refrigeration and air conditioning applications. One such HFC, 1,1,1,2-tetrafluoroethane (R-134a), is now widely used in automotive air conditioning systems, and has been used for the indirect cooling of electronic devices. Recent work at the National Transportation Research Center has also shown the potential for direct immersion cooling of power electronics for hybrid-electric vehicles using R-134a [74].

Perfluorocarbons (PFC's) have been widely used for the cooling of power electronics for over four decades. They offer high dielectric strengths, low toxicity and adequate heat transfer properties. Perfluorocarbons are currently used as heat transfer fluids for supercomputers, avionics, and many mission-critical military electronics. Perfluorohexane (C_6F_{14}), one such fluorocarbon, is available commercially as FC-72. Perfluorocarbons, along with HFC's, are non-ozone depleting, and are therefore excluded from the Montreal Protocol. However, perfluoro-carbons and hydrofluorocarbons are both greenhouse gases, and on a per mass basis, contribute significantly to global warming, as explained in the following section.

5.2. Greenhouse Gases and the Kyoto Protocol

Greenhouse gases are those which have a net positive effect on radiative forcing. Radiative forcing is typically defined as the change in irradiance at the tropopause, the atmospheric boundary between the troposphere and the stratosphere [75]. Radiative forcing is the cause of the well-known greenhouse effect. The infrared absorption and emission characteristics of a gas partially determine its significance as a greenhouse gas, along with other factors such as the atmospheric lifetime. The global warming potential (GWP) is a means of expressing the cumulative contribution of a unit mass of gas to radiative forcing over a designated time period relative to some reference gas [76]. Carbon dioxide is almost always used as the reference gas, with a GWP of 1. The global warming potential accounts for the net of direct and indirect contributions to global warming from a gas. The atmospheric lifetime of a gas primarily depends on the rate at which the gas decomposes from photolyzation or oxidation in the troposphere or stratosphere [77]. Whereas most naturally occurring substances such as methane or ozone have atmospheric lifetimes on the order of several years or less, inert HFC's and perfluorocarbons can have atmospheric lifetimes on the order of thousands of years.

The 1997 Kyoto Protocol set forth by the United Nations Framework Convention on Climate Change seeks to reduce greenhouse gas emissions worldwide. Nearly all major contributors to greenhouse gas emissions have signed and ratified the Protocol, with the exception of the United States, which has not yet ratified it. The Kyoto Protocol includes hydrofluorocarbons and perfluorocarbons, calling for reductions in their production and use [78].

With the potential reduction in the future availability of HFC's and perfluorocarbons, there has been considerable interest in low global warming potential coolants to replace perfluorocarbons and other more environmentally disruptive haloalkanes for the cooling of power electronics and other devices. Hydrofluoroethers (HFE's) are one potential alternative, offering relatively good dielectric properties with low global warming potentials. Another alternative is a new fluorinated ketone, $C_2F_5C(O)CF(CF_3)_2$, sold commercially by the 3M Company as Novec 649 Engineered Fluid. $C_2F_5C(O)CF(CF_3)_2$ is particularly attractive due to its high dielectric strength, similar thermophysical properties to those of perfluorohexane, and global warming potential of 1 over a 100 year timeframe [79]. Table 7 lists relevant properties of $C_2F_5C(O)CF(CF_3)_2$ and perfluorohexane [79].

Table 7: Relevant Properties of Novec 649 and FC-72 at 25 ºC.
Source: Ref. [79], reproduced with permission of IEEE, © 2008.

Molecular Formula	**$C_2F_5C(O)CF(CF_3)_2$**	**C_6F_{14}**
Fluid Type	Fluoroketone	Perfluorocarbon
Trade Name (3M™)	Novec™ 649 Engineered Fluid	Fluorinert™ Electronic Liquid FC-72
Normal Boiling Point (ºC)	49	56
Freezing Point (ºC)	<-100	<-100
Critical Temperature (ºC)	169	178
Critical Pressure (MPa)	1.87	1.83
Closed Cup Flashpoint (ºC)	None	None
Open Cup Flashpoint (ºC)	None	None
Surface Tension (mN/m)	11.4	12.0
Thermal Conductivity (W/m-K)	0.059	0.057
Liquid Specific Heat (J/kg-K)	1103	1050
Liquid Density (kg/m^3)	1610	1680
Kinematic Viscosity (cSt)	0.42	0.40
Latent Heat (kJ/kg)	88	88
Vapor Pressure at 25 ºC (kPa)	40.4	30.9
Vapor Pressure at 100 ºC (kPa)	441	350
Resistivity (GΩ-cm)	10,000	1,000,000
Dielectric Constant	1.84	1.76
Dielectric Strength (kV at 2.54 mm)	~40	~40
Solubility of H_2O in fluid (ppmw)	21	10
Atmospheric Lifetime (years)	0.014	3200
Global Warming Potential (100 year Integration Time Horizon)	1	9300
Ozone Depletion Potential	0	0

This portion of the study investigates the two-phase heat transfer performance of Novec 649 Engineered. Boiling properties of FC-72 are measured as a basis for comparison. Results are also compared to those expected by theory. Additionally, prospective enhancement techniques for improving the boiling heat transfer properties of $C_2F_5C(O)CF(CF_3)_2$ are investigated, focusing on nanoparticle-based enhancement using dilute dispersions of nanoparticles. Boiling deposition of nanoparticles provides distinct advantages in electronics cooling over other methods (such as application of thin-film coatings via the LbL method), in that the application process can be performed in situ, and the particle dispersion provides a regenerative coating. As such, methods are explored for dispersing metal and metal oxide nanoparticles in fluorinated fluids, with the end goal of depositing nanoparticles on heated surfaces via boiling deposition.

6. PREPARATION OF COLLOIDAL DISPERSIONS IN DIELECTRIC FLUIDS

6.1. Theoretical Aspects of Dispersing and Stabilizing Nanopowders in Liquids

The stability of a colloidal system relies on maintaining the small size of the dispersed particles such that Brownian motion of the fluid can keep the particles suspended. Inter-particle forces have a significant impact on stability, resulting in agglomerates (loosely bound particles) or aggregates (tightly bound) which, when they become large enough, settle out of the fluid. Chemical agents can also decrease inter-particle stability, causing flocculation (sometimes used synonymously with agglomeration). In a colloidal system, there are two primary competing mechanisms which affect particle stability: attractive dispersion forces between particles (commonly attributed to Van der Waals forces, or dipole-dipole attraction, which encompasses London Dispersion Forces) and repulsive forces between particles. Repulsive forces between particles may be electrostatic or steric, or both. A popular theory for describing the inter-particle forces between suspended particles, and therefore the stability of a colloidal system, is that developed independently by Derjaguin, Landau, Verwey, and Overbeek (DVLO Theory, see Ref. [80] for a detailed description of the theory). However, DVLO theory was developed for aqueous media, and cannot be applied to nonpolar dispersions since the Debye length, necessary to describe DVLO theory, is undefined [81].

Stabilization methods for colloidal dispersions may be placed in three general categories: electrostatic, steric, and electrosteric. Electrostatic stabilization relies on the repulsions between like surface charges on the particles. Electrostatic stabilization is popular for oxide particles (such as alumina, silica, zirconia, etc.) in aqueous media since the surface charge may be readily controlled by adjusting the pH. The degree of stability depends on the zeta potential of the system, and as the isoelectric point (i.e., the pH at which the net electric charge of all particle surfaces is zero) of the aqueous system is approached, the particles will begin to rapidly agglomerate and settle. Steric stabilization, commonly referred to as polymer stabilization, relies upon adsorption of a relatively long chain molecule onto the particle which prevents particle-particle interaction. When two particles coated with polymers interact, the adsorbed polymer layers overlap, resulting in repulsion due to osmotic pressure (i.e. a higher concentration of polymer in the overlap region) and what is referred to as “entropic repulsion.” [82]. Electrosteric methods rely on the adsorption of a charged molecule onto the dispersed particles, providing

both electrostatic repulsion and some physical barrier to agglomeration. For example, citrate ions have been used to stabilize gold nanoparticles in water.

For this study, steric and electrosteric methods are applicable for dispersing and stabilizing particles in the fluorinated ketone. A dispersant refers to the additive (usually a polymer) used to disperse and stabilize the particles. Note that all dispersants are surface active agents (surfactants), but not all surfactants are dispersants. Some surfactants may actually act as coagulants, decreasing stability of dispersions. Three criteria are required to successfully disperse nanoparticles in a base fluid using the steric or electrosteric approach. First, the surface active agent (surfactant) must be soluble in the base fluid. Although this seems trivial, many surfactants are either insoluble or poorly soluble in fluorocarbons and similar fluids (like the fluorinated ketone), due to the non-polar nature of such fluids. Second, the solvated surfactant must be capable of adsorbing onto the particle surface, and the strength of this adsorption is important, since shear forces can strip the surfactant from the particles. Therefore, the type of particle that is being dispersed, in addition to the base fluid, influences the surfactant. Lastly, the surfactant must be capable of preventing particle agglomeration. This is primarily dominated by the thickness of the absorbed layer on the particle. The minimum critical adsorbed polymer thickness, t_0, required for each particle is:

$$t_0 = \frac{dA_{121}}{48kT} \qquad (22)$$

where d is the particle diameter, kT represents the particle's kinetic energy, and the Hamaker constant, A_{121}, depends on the particle-fluid combination [83]. Clearly both the fluid and particle type are important for determining the best dispersant for a given situation. Nelson created tables offering a general approach to selecting a suitable class of surfactant for preparing a particular particle/fluid dispersion [84]. In the tables, Nelson distinguishes fluorinated liquids as its own class of fluid, and indicates that the optimum surfactant for this fluid type will depend on whether the dispersed particles are metals or metal oxides. Using this general approach, fluorinated surfactants were chosen for further study as a dispersing agent for preparing colloidal dispersions in the fluorinated ketone.

6.2. Colloidal Dispersions of Nanoparticles in a Fluorinated Ketone

6.2.1. SiO_2 Nanoparticles

Dilute dispersions of SiO_2 nanoparticles in $C_2F_5C(O)CF(CF_3)_2$ were prepared using a two-step method. Commercially available silica nanopowder (15 nm particle size, Sigma Aldrich) was added to pure $C_2F_5C(O)CF(CF_3)_2$ (Novec 649, 3M Company) and sonicated using a probe sonicator (VibraCell VC-505, Sonics & Materials). One should note that despite the manufacturer's stated size of 15 nm, nanoparticles in the dry powder likely form much larger aggregates. This is a primary disadvantage of two-step preparation methods, as it is difficult to break up tightly bound nanoparticles that have aggregated in dried form.

Even with aggressive sonication, the SiO_2 particles quickly flocculated in the fluorinated ketone, and settled to the bottom of the liquid shortly thereafter. Due to the inability to disperse the SiO_2 particles, various surfactants were tested in varying concentrations to disperse and stabilize the particles. Fluorinated surfactants were chosen due to the higher likelihood of solvation in fluorinated liquids. Additionally, fluorinated surfactants have been used in the past to disperse particles in fluorinated liquids. For example, magnetite particles have been successfully dispersed with a fluorinated surfactant in a fluorocarbon-type solvent [85]. After various trials, one particular fluorinated surfactant was chosen for use in preparing SiO_2 dispersions in the fluorinated ketone.

0.01% by volume and 0.001% by volume SiO_2 particles were prepared in $C_2F_5C(O)CF(CF_3)_2$ using the aforementioned fluorinated surfactant. 600 mL quantities of the 0.01vol% SiO_2 in Novec 649 dispersions were prepared for boiling tests by adding small quantities of fluorinated surfactant to the pure fluid. After sonicating to dissolve the surfactant, the SiO_2 nanoparticles were added and sonicated. Sonication was carried out with an ice bath surrounding the beaker to prevent overheating and evaporation of the fluid. 0.001vol% SiO_2 dispersions were prepared in a similar manner, except that the surfactant concentration was reduced. Following sonication, the SiO_2 appeared well-dispersed, with no visible signs of settling after several hours. However, the majority of particles appeared to have settled after one day, though they could be re-dispersed easily by shaking. SiO_2 particles in Novec 649, with no surfactant, remained flocculated, even after agitation. Figure 41 shows smaller samples (in which sonication times were reduced) of the dispersions shortly after preparation.

Figure 41: (Left) Pure Novec 649; (Middle) 0.01vol% SiO_2 in Novec 649 with Fluorinated Surfactant ~1 hour after preparation (Middle); and (Right) 0.01vol% in Novec 649 w/o surfactant ~40 minutes after preparation. Note that the sample without the surfactant is heavily flocculated, whereas the sample with surfactant appears well-dispersed.

6.2.2. Aluminum Nanoparticles

Commercially available aluminum nanopowder (99.99% pure, NTbase #NP-A80) was dispersed in Novec 649 using the aforementioned probe sonicator. According to the vendor, the aluminum nanoparticle size is between 45 nm and 55 nm [86], although as with the SiO_2 nanopowder, aggregation in the dry state is expected to increase the dispersed particle diameter. 0.01vol% concentrations of aluminum were dispersed with a small amount of fluorinated surfactant and with no surfactant, using the same method as that described for the SiO_2 particles in section 6.2.1. However, extra caution was used in handling the aluminum nanopowder, as it can oxidize rapidly in air and is potentially flammable. The aluminum particles appeared to disperse well in the fluorinated ketone. The surfactant appeared to have minimal effect on the dispersion and stability of the aluminum particles. Both 0.01vol% aluminum dispersions appeared initially stable, with some visible settling after one hour. After one day, it appeared as though the majority of particles had settled to the bottom, though the fluid still had a grayish tint. Figure 42 shows small samples (with reduced sonication times) shortly after preparation. It is not surprising that the surfactant had minimal effect because, as described in section 6.1, the optimal dispersant depends both on fluid type and particle type, and is typically different for metal oxides and metals in the same fluid.

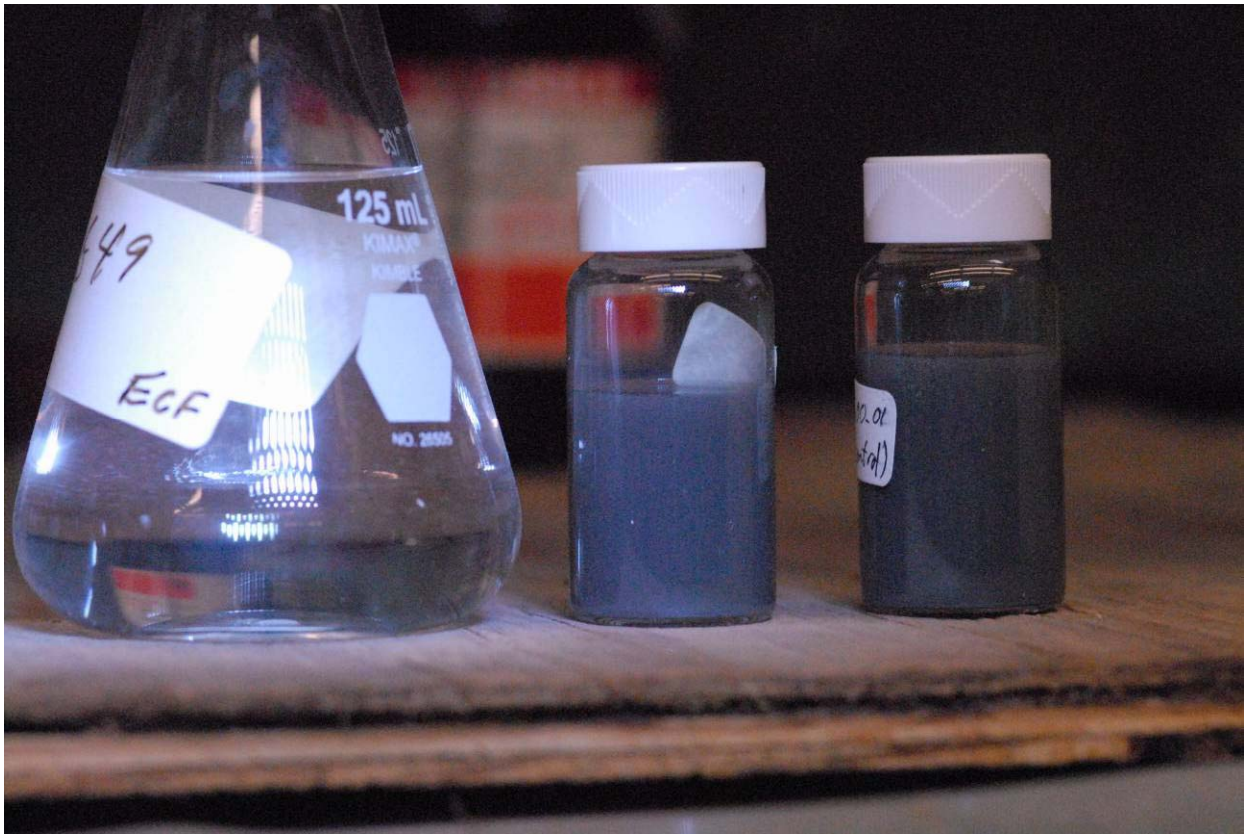

Figure 42: (Left) Pure Novec 649; (Middle) 0.01vol% Aluminum in Novec 649 with Fluorinated Surfactant ~1 hour after preparation; and (Right) 0.01vol% Aluminum in Novec 649 w/o surfactant ~40 minutes after preparation. Note that both samples appear relatively well-dispersed.

7. WIRE BOILING TESTS IN DIELECTRIC FLUIDS

Pool boiling data were obtained for 0.01" nickel wires in pure $C_2F_5C(O)CF(CF_3)_2$, pure FC-72, $SiO_2/C_2F_5C(O)CF(CF_3)_2$ dispersions, and $Al/C_2F_5C(O)CF(CF_3)_2$ dispersions at saturation and atmospheric pressure. Unlike for the boiling in water in Section I, the dimensionless radius, R^*, in the Novec 649 and FC-72 was within the required limits for Lienhard's CHF prediction for horizontal cylinders (see section 8.2), and the measured CHF data for the pure fluids agreed well with the predictions. Additionally, the scatter in the CHF data for the pure fluids was surprisingly small, and can likely be attributed to the dielectric nature of the fluids tested. That is, since the fluids have high dielectric strengths, electrolysis becomes a non-issue, thereby preserving the surface conditions to a better degree than boiling in water using DC resistive heating. However, material compatibility issues with the fluids became a cause for concern, as deleterious interactions with plasticizers or other materials could affect the boiling curves. Therefore, every step was taken to ensure compatibility with materials in the boiling apparatus, as discussed in the following section.

7.1. Experimental Apparatus

A wire boiling facility separate from that used for the water tests was assembled due to materials concerns and fluid volume requirements. The compatibility of $C_2F_5C(O)CF(CF_3)_2$ with polycarbonate has not been explored, so a glass vessel was used instead to hold the test fluids. Additionally, given the much higher expense of FC-72 and Novec 649 compared to de-ionized water, the boiling apparatus was downsized so that less fluid would be used in each test. Figure 43 shows a schematic of the boiling apparatus used for the boiling tests of the dielectric fluids. Instead of an isothermal bath, a temperature controlled hotplate was used to maintain the fluids at their saturation temperatures. The power supply, data acquisition system, and other components, along with the measurement techniques, were the same as those described in section 3.1.

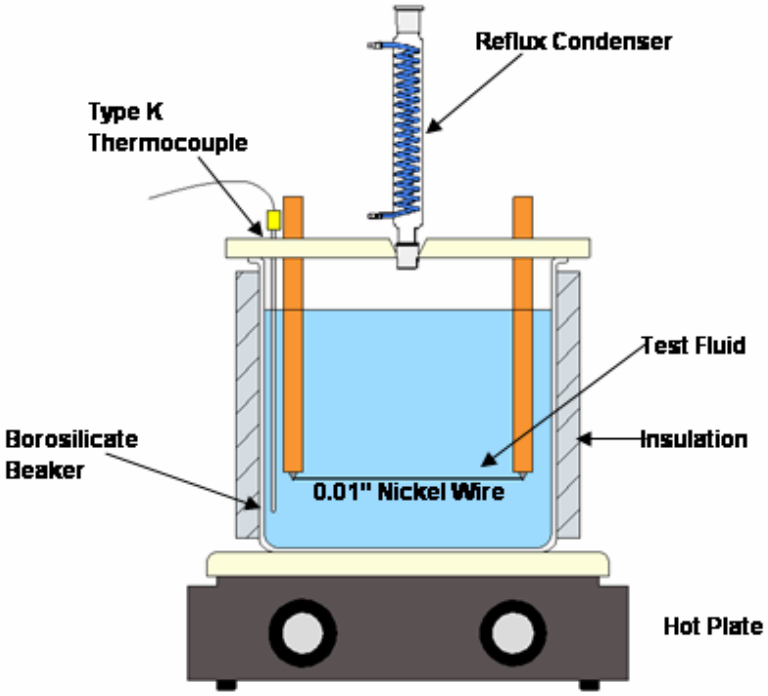

Figure 43: Schematic of the Wire Boiling Setup Used for Boiling Tests of FC-72 and Novec 649.

Since the saturation temperatures of the dielectric fluids investigated in this portion of the study were, on average, 47 K lower than the saturation temperature of water, the temperature coefficient of resistance for nickel was recalculated in the interval of 25 ºC to 75 ºC. A similar analysis was done for this temperature range as was performed in section 3.1.1, with a least squares linear regression being applied to the data and the uncertainty calculated in the slope. The new temperature coefficient of resistance was calculated as $\alpha=0.005628 \pm 0.0006\ K^{-1}$, only $0.0003\ K^{-1}$ more that the temperature coefficient used for boiling in saturated water. The Biot number was once again calculated for these tests, and using a bounding maximum value of 25,000 W/m^2-K for the heat transfer coefficient, determined to be Bi=0.018, which is less than 0.1. Therefore, the lumped capacitance model is highly appropriate for the radial temperature distribution in the boiling tests with dielectric fluids, and the surface temperature of the nickel wire may be assumed equal to the average radial temperature.

Since the wires used in the FC-72 and Novec 649 boiling experiments were shorter than those used in the water tests, there was a slightly larger fractional uncertainty in the length measurements. This in turn led to typical measurement uncertainties of 3.7% or less for the heat flux, 12% or less for the wall superheat, and 13% or less for the heat transfer coefficient.

7.2. Property Measurements of Pure $C_2F_5C(O)CF(CF_3)_2$

Various properties of the fluorinated ketone Novec 649 were measured at room temperature to predict boiling properties and compare against reported values from researchers at 3M [79]. Table 8 summarizes measured properties of Novec 649 at room temperature. Liquid density was measured using a 50 ± 0.05 mL flask and precision balance. The kinematic viscosity of the liquid was measured using a glass tube capillary viscometer and stopwatch. Surface tension was measured using the Wilhelmy Plate method with a Sigma 703 Tensiometer, and was validated by first measuring the surface tension of water, which at 23 ºC was measured as 72.3 mN/m, with an expected value of 72.58 mN/m. The thermal conductivity was measured using a KD2 Pro Thermal Properties Analyzer with the KS-1 sensor probe. All measured values agreed well with those reported by 3M (see Table 7). Although the stated uncertainty of the KD2 Pro with KS-1 in the 0.02-0.2 W/m-K range is 0.01 W/m-K [87], convection effects could have interfered with the measurement, artificially increasing the thermal conductivity value.

Contact angle was measured for the fluorinated ketone on aluminum and stainless steel plates. Due to the low surface tension, the fluid was nearly perfectly wetting on both surfaces, making measurement of contact angles difficult. Figure 44 shows contact angles captured 100 ms after droplet contact with the surface. From these contact angles, one may conclude that the fluorinated ketone is very well wetting, as expected from the low surface tension.

Table 8: Summary of Measured Properties of $C_2F_5C(O)CF(CF_3)_2$ at Room Temperature

Property	Apparatus	Value
Liquid Density (at 21º C)	Volumetric Flask and Precision Balance	1607 ± 2 kg/m^3
Liquid Kinematic Viscosity (at 21ºC)	Capillary Viscometer	0.4243 ± 0.0048 cSt
Surface Tension (at 23º C)	Sigma 703 Tensiometer	11.47 ± 0.23 mN/m
Liquid Thermal Conductivity (at 23º C)	KD2 Pro Thermal Property Analyzer	0.092 ± 0.01 W/m-K

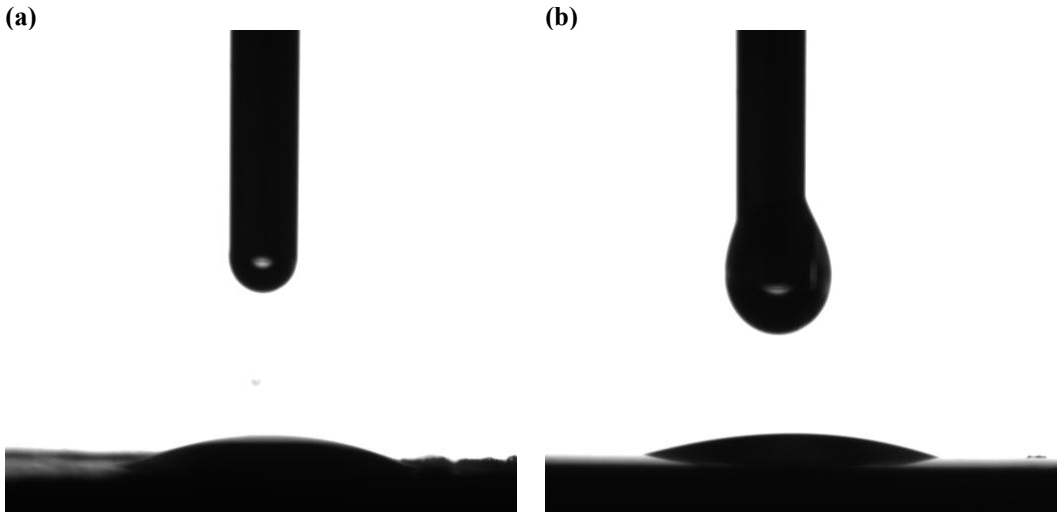

Figure 44: Contact Angles for Novec 649 100 ms After Droplet Contact on (a) smooth stainless steel and (b) smooth aluminum.

7.3. Results of Wire Boiling Experiments

For all boiling tests, nickel wires were tested in as-received surface condition, though they were thoroughly cleaned prior to each test. The wires were cleaned by sonicating in acetone, rinsing with ethanol, and sitting to dry completely. Tests were conducted by increasing the heat flux in small steps (~10 kW/m^2) in order to observe the incipience of boiling. Unlike in the water boiling tests, many wires survived CHF, allowing for acquisition of film boiling data and the minimum heat flux (MHF). Some post-CHF data will be presented, but not covered in detail, as that analysis is beyond the topic and scope of these studies.

Table 9 summarizes average CHF values obtained for saturated boiling of the dielectric fluids. As seen in the table, boiling in colloidal dispersions enhances the CHF of the fluorinated ketone, whereas boiling with the dispersant tends to degrade the CHF slightly. Nonetheless, the net effect from boiling in the SiO_2 dispersion is still to enhance CHF, despite the presence of the surfactant. Boiling in the aluminum dispersion, with no surfactant, yields the greatest enhancement in CHF. Detailed results for all cases are provided in section 7.3.1 through section 7.3.5.

Table 9: Summary of CHF Results for Pool Boiling of 0.01" Nickel Wires in Saturated Dielectric Fluids.

Test Case	Average CHF	CHF Std. Dev.†	CHF 90% Conf. Interval‡	CHF Enhancement
Pure Novec 649	200 kW/m^2	0.52%	[198 kW/m^2, 202 kW/m^2]	-
Novec 649 w/0.001wt% surfactant	170 kW/m^2	9.2%	[152 kW/m^2, 188 kW/m^2]	-15%
Novec 649 w/0.01wt% surfactant	189 kW/m^2	5.6%	[163 kW/m^2, 215 kW/m^2]	-5.4%
0.001vol% SiO_2 in Novec 649 w/0.001wt% surfactant	205 kW/m^2	1.5%	[200 kW/m^2, 210 kW/m^2]	2.6%
0.01vol% SiO_2 in Novec 649 w/0.01wt% surfactant	274 kW/m^2	1.4%	[267 kW/m^2, 281 kW/m^2]	37%
0.01vol% Aluminum in Novec 649 (no surfactant)	280 kW/m^2	6.0%	[252 kW/m^2, 308 kW/m^2]	40%
Pure FC-72	220 kW/m^2	8.3%	[189 kW/m^2, 251 kW/m^2]	N/A

†Standard deviation (% of average) over three nominally identical tests (four tests for the bare wire case).
‡Calculated from the t-distribution.

7.3.1. Nickel Wire in Pure FC-72

Boiling tests were conducted for 0.01" nickel wires in FC-72 (perfluorohexane) at atmospheric pressure and its saturation temperature of 57 ºC. Figure 45 shows boiling curves for the FC-72 tests, with an average CHF of 220. ± 18.3 kW/m^2. In Figure 45, one can see a significant increase in the temperature in the natural convection regime, with a substantial drop in temperature at the incipience of boiling. This temperature overshoot was marked by rapid activation of nucleation sites across the surface. Figure 46 shows boiling in various regimes, including nucleate boiling, high heat flux film boiling, low heat flux film boiling, and an interesting steady-state phenomenon where the sides of the wire have quenched with the middle remains in the film boiling regime.

Results of the FC-72 boiling tests compared well with data found in the literature, though direct comparisons are cursory when geometries and surface materials differ. Kim et al. obtained a CHF of 170 kW/m^2 at a superheat of ~30 ºC for the pool boiling of saturated FC-72 from a 390 μm (0.15") platinum wire at atmospheric pressure [8]. Liu et al. obtained a CHF of 232 kW/m^2 at a superheat of ~15 ºC for the pool boiling of saturated FC-72 from a flat surface at atmospheric pressure [88].

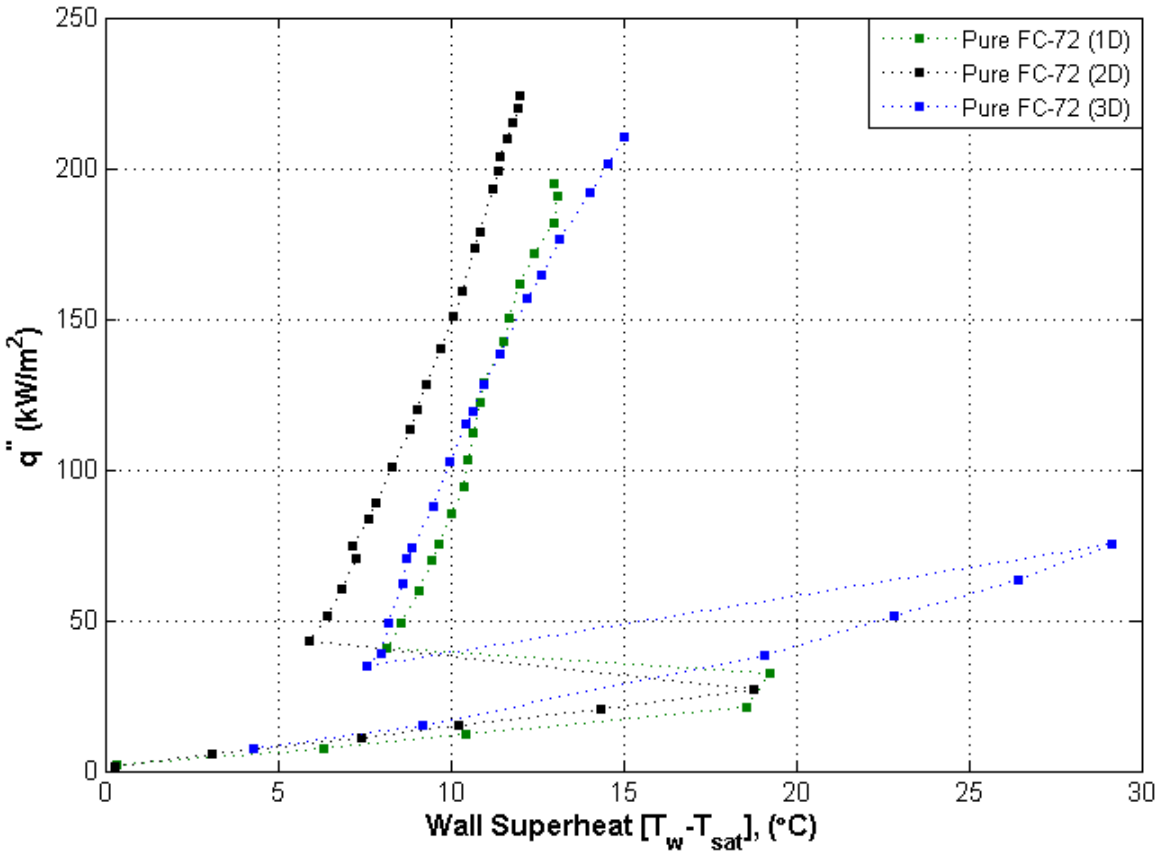

Figure 45: Boiling Curves for 0.01" Nickel Wires in Pure FC-72. Note the significant temperature overshoot prior to the incipience of boiling.

(a)

(b)

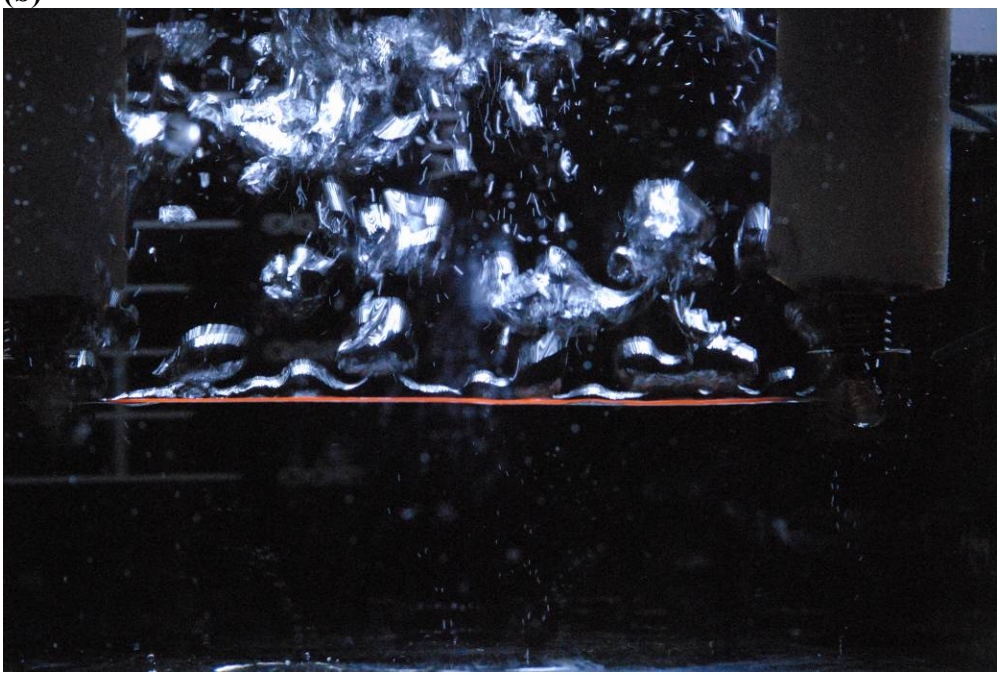

(c)

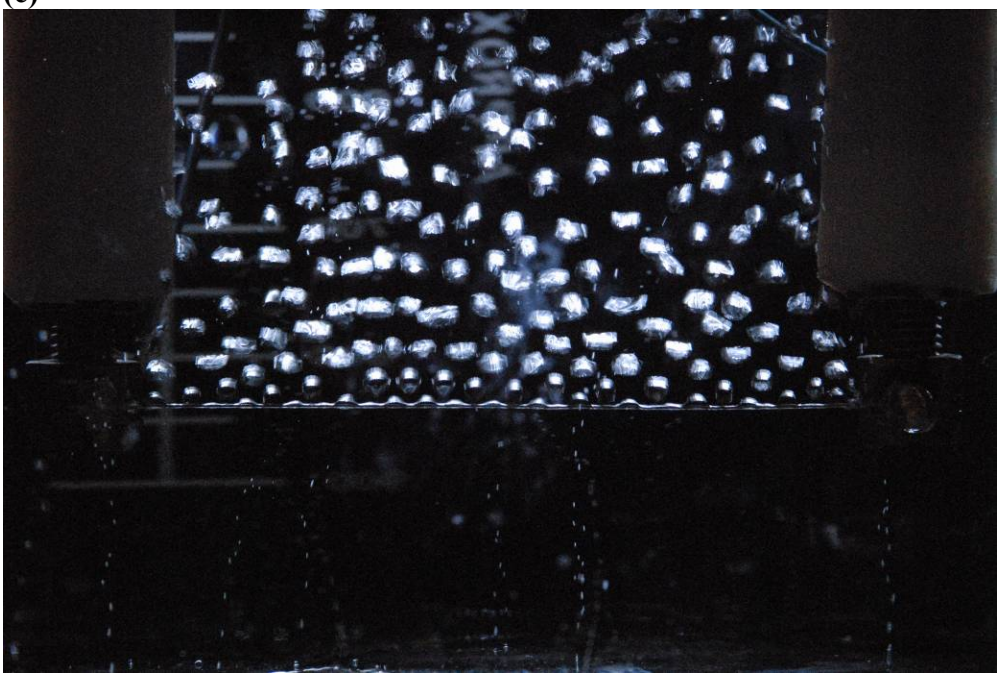

(d)

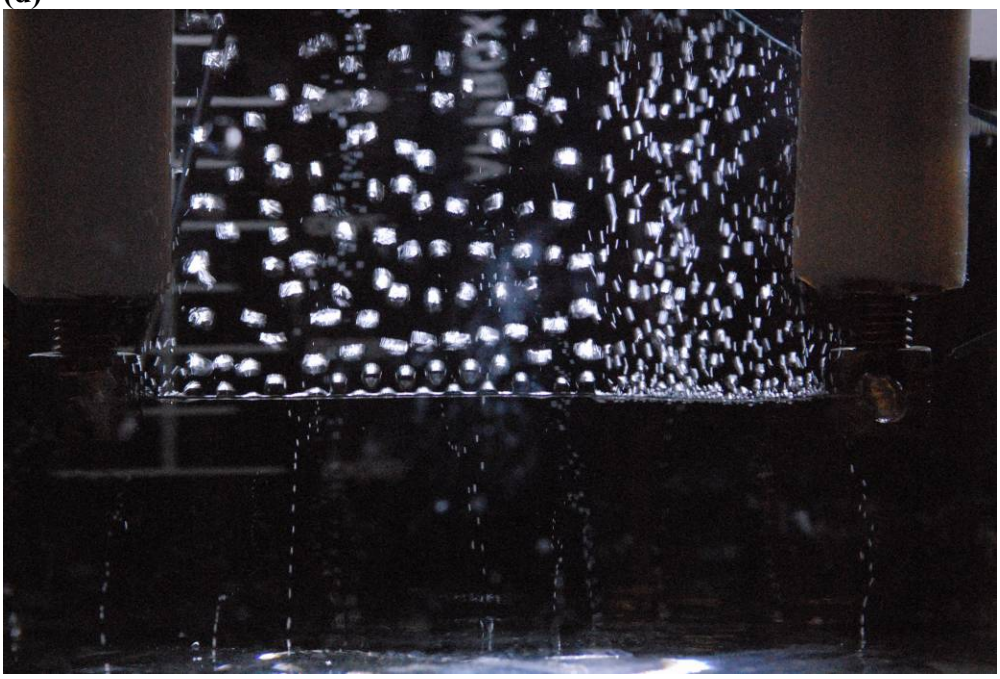

Figure 46: Photos of Boiling from a 0.01" Nickel Wire in Saturated FC-72 at Atmospheric Pressure. (a) Nucleate boiling at q''=125 kW/m^2, (b) film boiling immediately following CHF, (c) film boiling prior to the Leidenfrost point, (d) steady-state film and nucleate boiling, where the sides of the wire have quenched.

7.3.2. Nickel Wire in Pure $C_2F_5C(O)CF(CF_3)_2$

Boiling tests were conducted for 0.01" nickel wires at atmospheric pressure in pure Novec 649 at its saturation temperature of 49 ºC. The results of these tests were compared against the results of the FC-72 boiling tests to gauge the two-phase heat transfer performance of the new fluorinated ketone. As seen in Figure 47, the fluorinated ketone performed comparably in both nucleate boiling heat transfer coefficient and critical heat flux. Photographs were also taken to visualize boiling in the fluorinated ketone, with nucleation parameters resembling those seen in boiling of perfluorohexane. As with the FC-72, the temperature overshoot was observed when boiling in the Novec 649. Figure 48 shows several boiling regimes, including the rapid activation of nucleation sites at boiling incipience, high heat flux film boiling immediately following CHF, and the same steady-state phenomenon observed with the FC-72 where a portion of the wire has quenched. Overall, results indicate that from a heat transfer perspective, Novec 649 and FC-72 behave similarly, and thus the former may be a viable alternative to the latter in the direct and indirect cooling of high power density electronic devices.

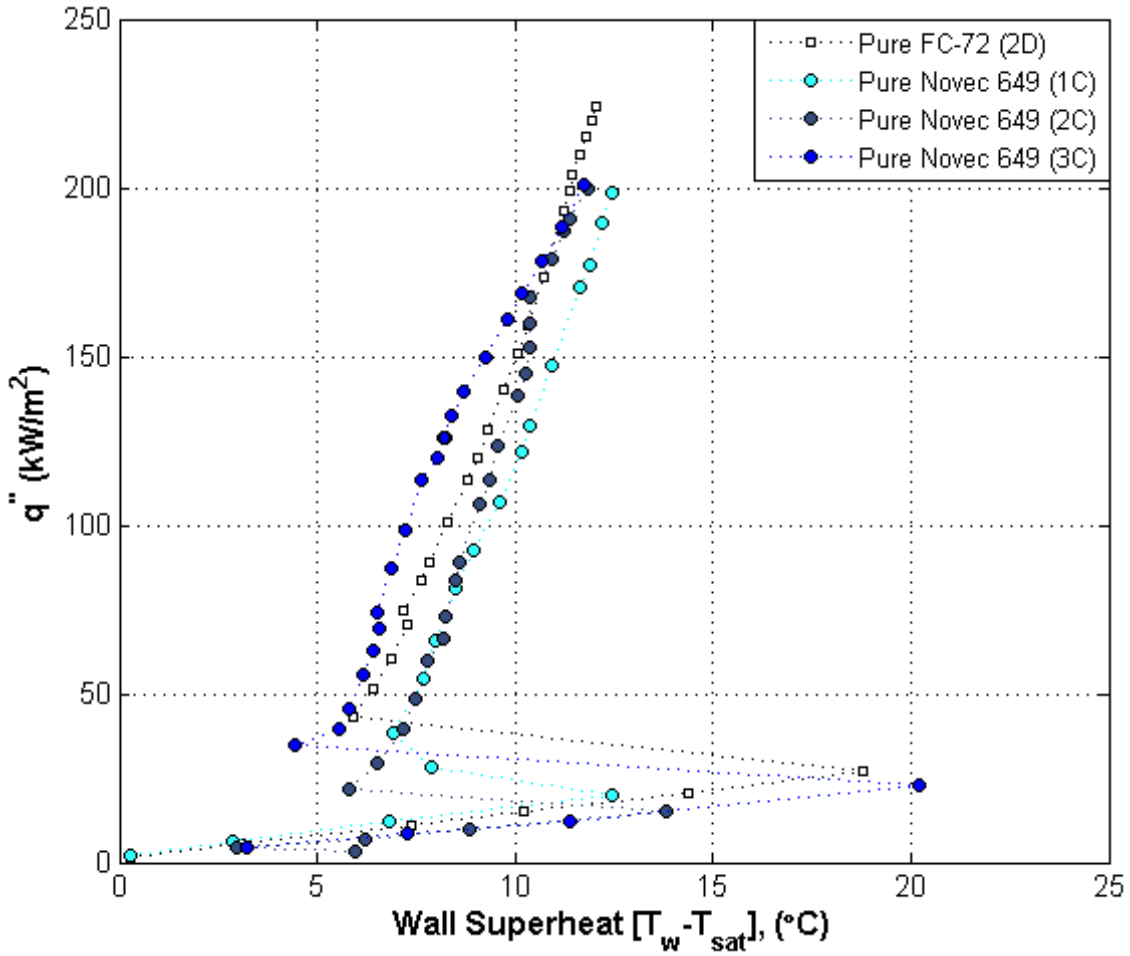

Figure 47: Boiling Curves for 0.01" Nickel Wires in Pure Novec 649 at Saturation and Atmospheric Pressure. A boiling curve for FC-72 is plotted as a reference. Note that the temperature overshoot also occurs in this fluorinated ketone.

(a)

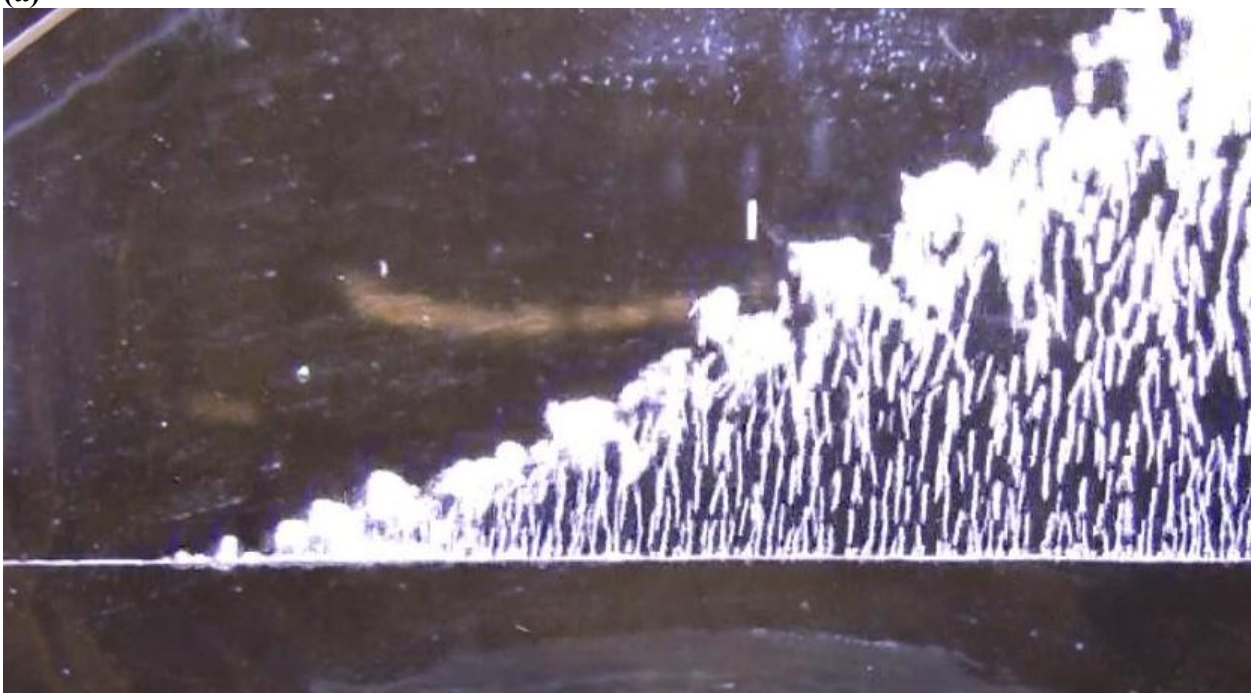

(b)

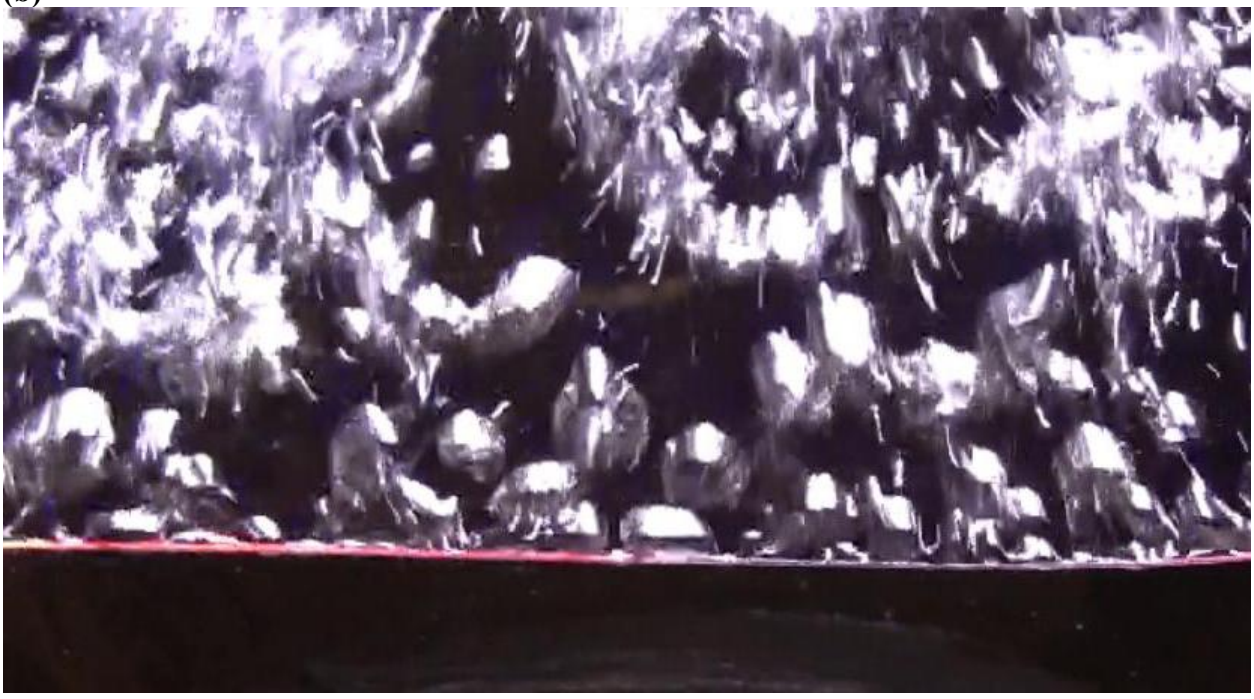

(c)

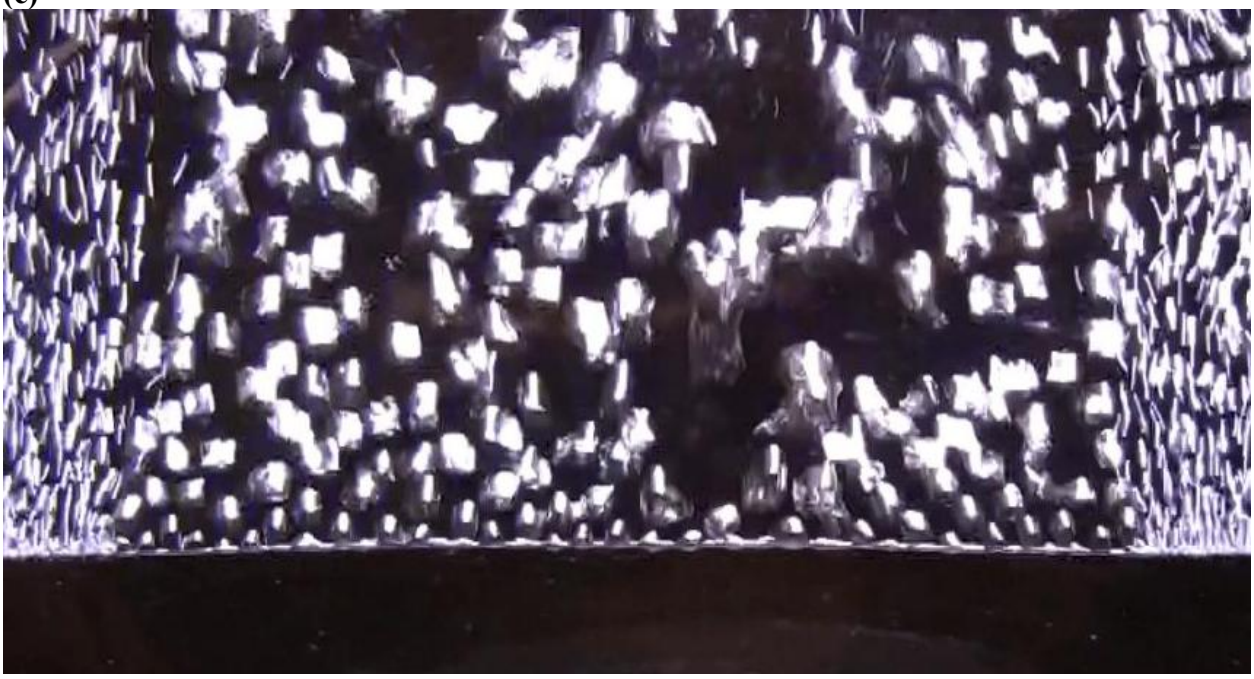

Figure 48: Photographs of Boiling from a 0.01" Nickel Wire in Novec 649. (a) The onset of nucleate boiling, at which nucleation sites activated rapidly across the wire, (b) film boiling on the wire immediately following CHF, (c) simultaneous film and nucleate boiling where the ends of the wire have quenched.

7.3.3. Effect of Dispersant on Boiling Heat Transfer

Small concentrations of a fluorinated surfactant were used to help disperse silica particles in the fluorinated ketone. Therefore, it was important to assess the effects of the surfactant on two-phase heat transfer. Surfactants alone have been added to fluids to alter boiling properties. Wu et al. observed enhancement in the pool boiling heat transfer coefficient in water [89] and others have demonstrated that CHF enhancement is possible with soluble surface active agents, even in flow boiling [90]. Since surfactants can change surface tension and wettability, they can have a significant effect on wettability and bubble nucleation, even at low concentrations. Figure 49 shows boiling curves for 0.01wt% and 0.001wt% fluorinated surfactant in Novec 649, and Figure 50 shows the effective heat transfer coefficient. As seen in the figures, the addition of the fluorinated surfactant has a deleterious effect on nucleate boiling heat transfer and degrades the CHF slightly. Since fluorinated surfactants in water can alter the surface tension by 58% or more [91], the change in surface tension achieved by adding the fluorinated surfactant to the fluorinated ketone was measured. As seen in Table 10, the fluorinated surfactant had no effect

on the surface tension of the fluorinated ketone. However, the fluorinated surfactant may have altered the interfacial tensions at the surface between the solid-liquid and solid-vapor interfaces, thereby altering boiling properties. Another possibility is that boiling distilled the fluorinated surfactant on the surface, resulting in a thick enough film to insulate the wire. These hypotheses were not explored further, though. Nonetheless, one must consider the deleterious effect of the fluorinated surfactant when looking at boiling results for the silica test case, which utilized the surfactant to disperse the particles.

Table 10: Surface Tension Measurements for Pure Novec 649 and Novec 649 with 0.01wt% Fluorinated Surfactant. Note that the surfactant had a negligible effect on the surface tension of the fluid.

	Pure Novec 649	Novec 649 + 0.01wt% Fluorosurfactant
Run 1	11.4 mN/m	11.7 mN/m
Run 2	11.6 mN/m	11.8 mN/m
Run 3	11.5 mN/m	11.7 mN/m
Average:	**11.5 ± 0.1 mN/m**	**11.7 ± 0.1 mN/m**

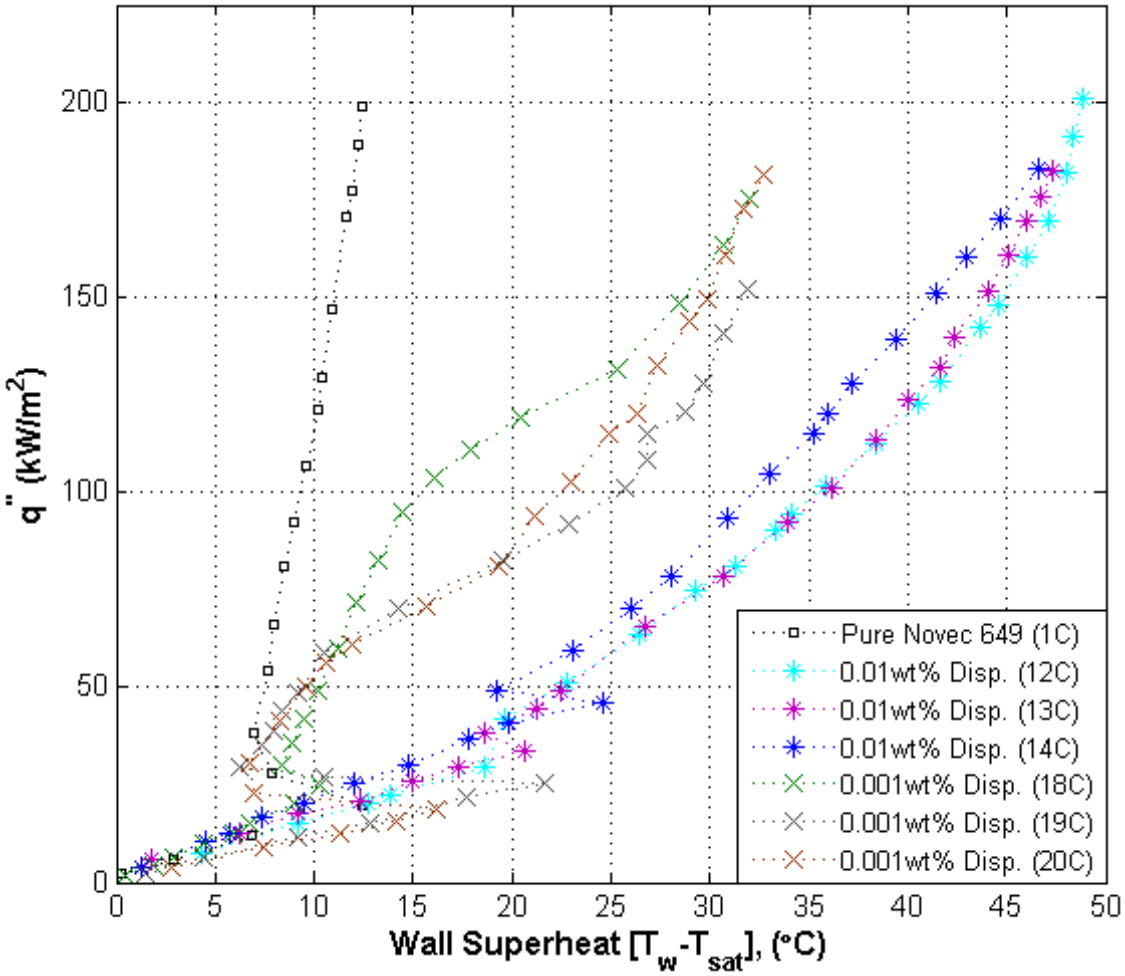

Figure 49: Boiling Curves for 0.01" Nickel Wires in Novec 649 with Different Concentrations of a Fluorinated Surfactant.

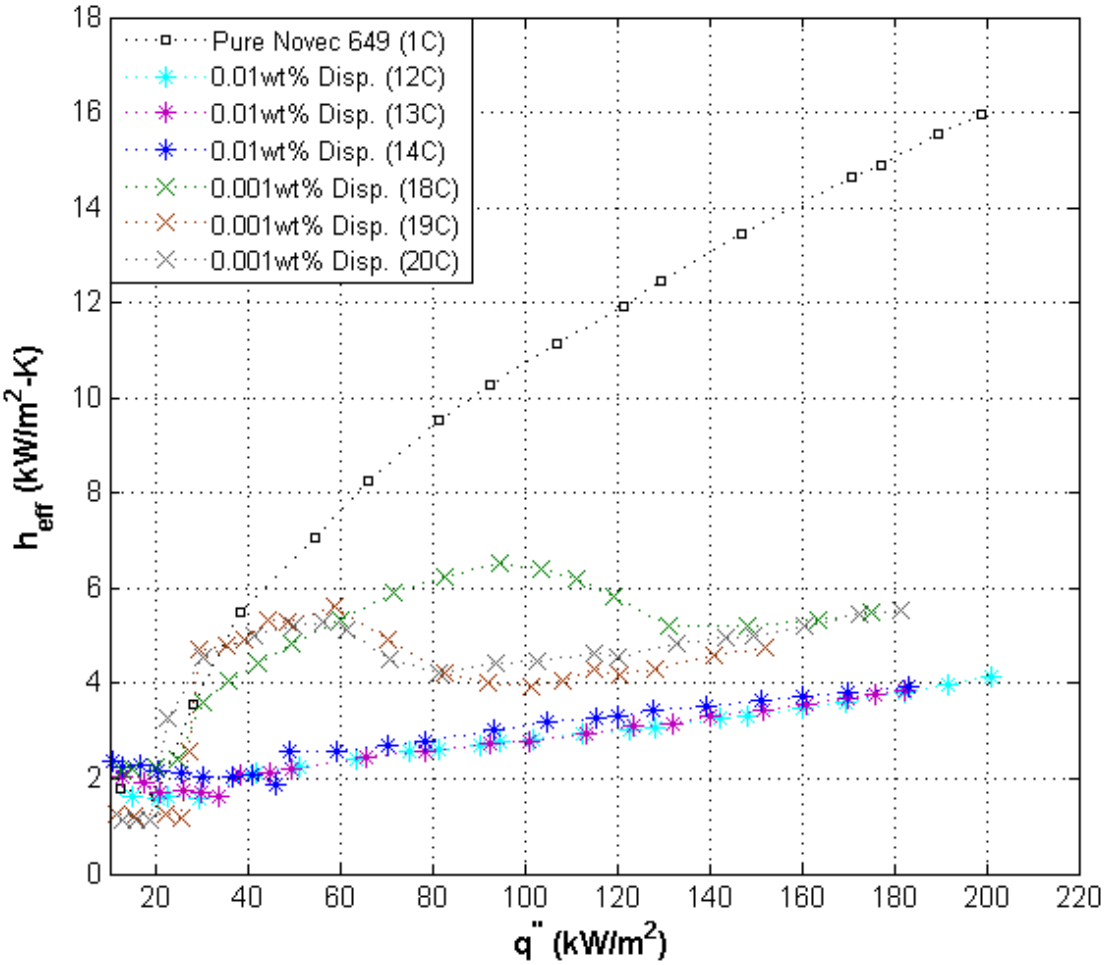

Figure 50: Effect of the Dispersant on the Nucleate Boiling Heat Transfer Coefficient for Novec 649.

7.3.4. Nickel Wire in $SiO_2/C_2F_5C(O)CF(CF_3)_2$ Colloid with Dispersant

Boiling tests were conducted with 0.01" nickel wires in SiO_2/Novec 649 dispersions (see section 6.2.1). Figure 51 shows boiling curves for 0.001vol% concentrations of SiO_2 nanoparticles, and Figure 53 shows curves for 0.01vol% concentrations. For the lower concentration, there is essentially no net effect on CHF or the nucleate boiling heat transfer coefficient (except for test 17C, in which considerable enhancement was observed). For the higher concentrations, the curves displayed unusual shifts, and the heat transfer coefficient data was widely scattered, as seen in Figure 53. However, the CHF in this case was noticeably enhanced, on average 37% over the pure fluid value. Following boiling tests in the SiO_2 colloidal dispersion, a white deposition was visible on the surface. This deposition was expected to consist of SiO_2 nanoparticles. Although the particles stayed on the surface with gentle handling, they could easily be wiped off.

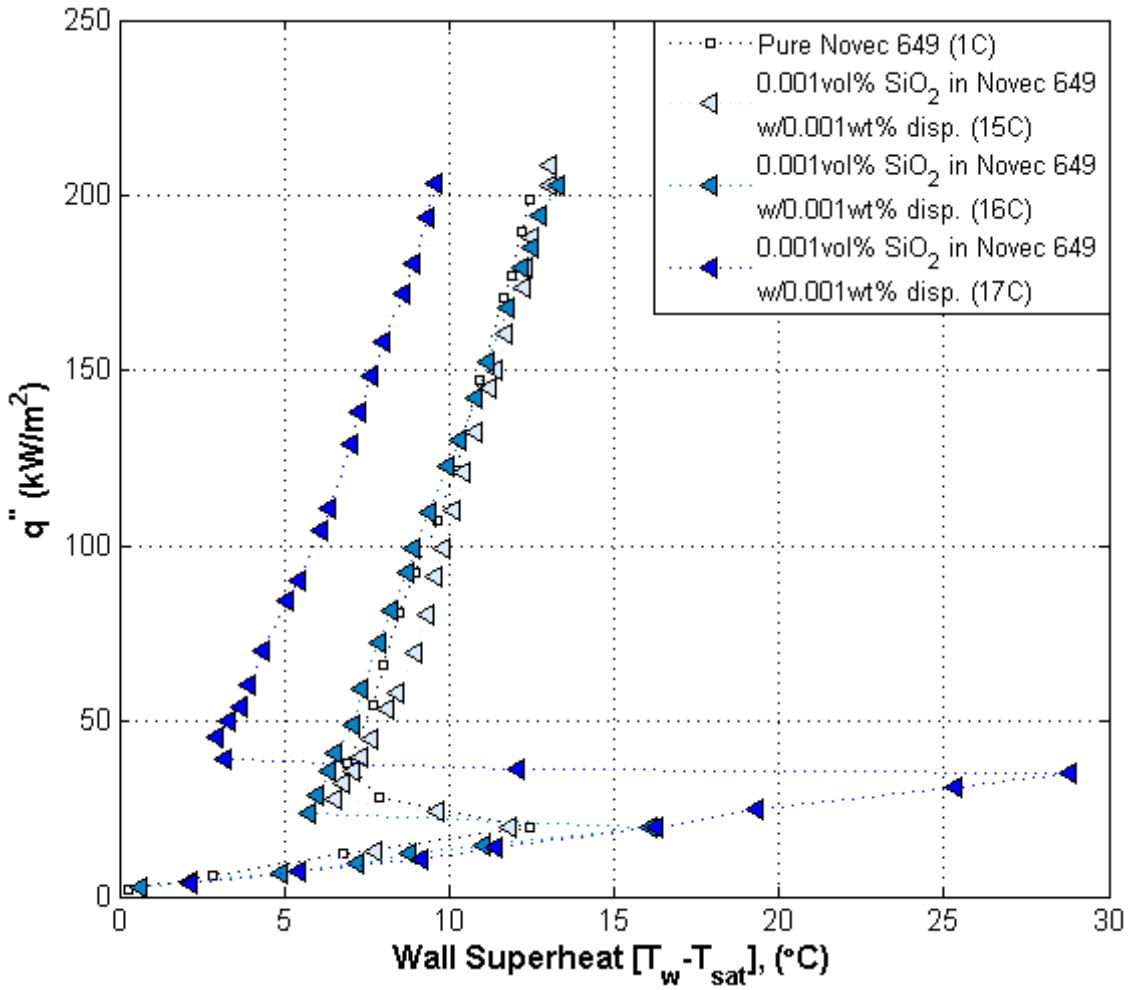

Figure 51: Boiling Curves for 0.01" Nickel Wires in 0.001vol% SiO_2/Novec 649 Dispersion with 0.001wt% Fluorinated Surfactant.

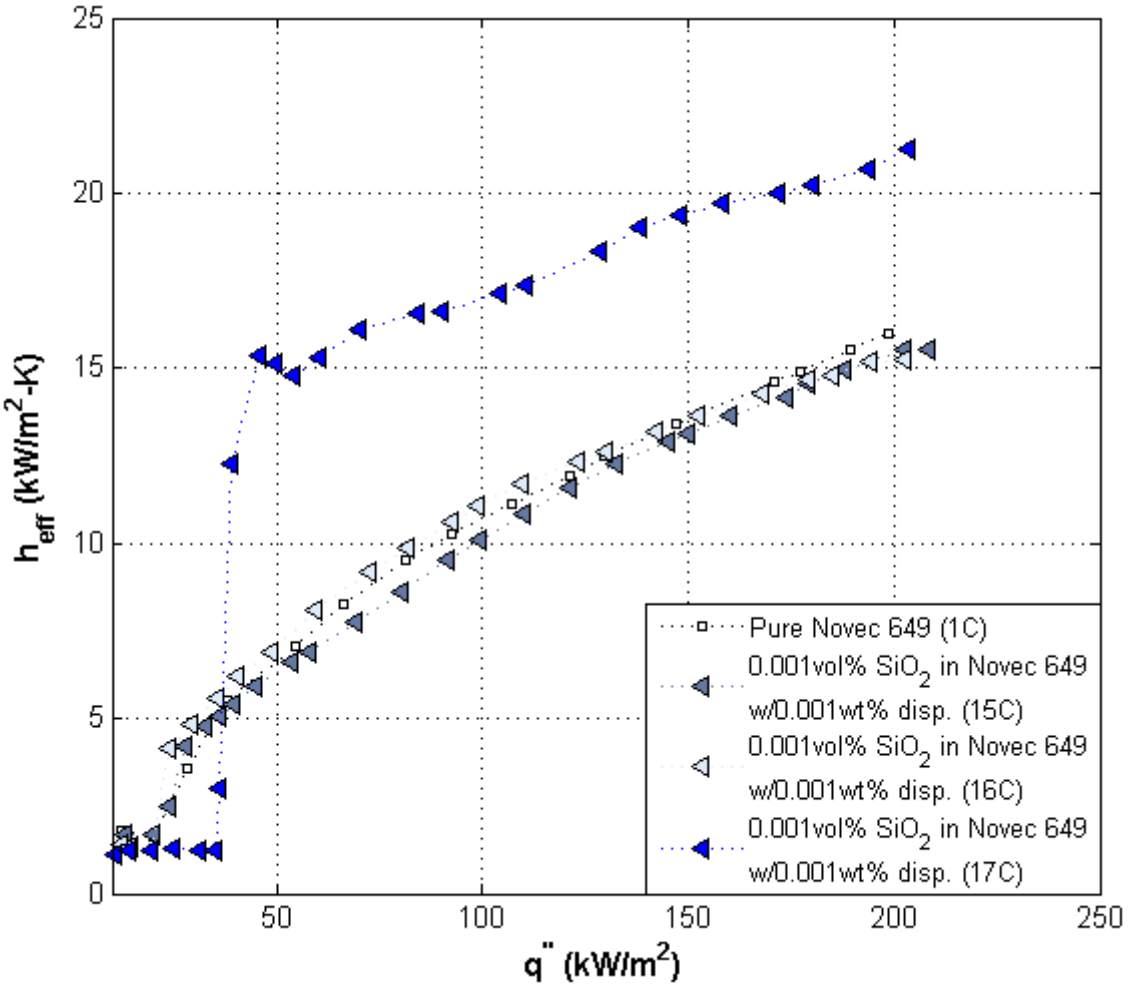

Figure 52: Effective Heat Transfer Coefficient versus Heat Flux for the Boiling Curves Plotted in Figure 51. Note that the 0.001vol% SiO_2 dispersions have the same heat transfer coefficient as the pure fluid case, except in one test where up to 50% enhancement was observed.

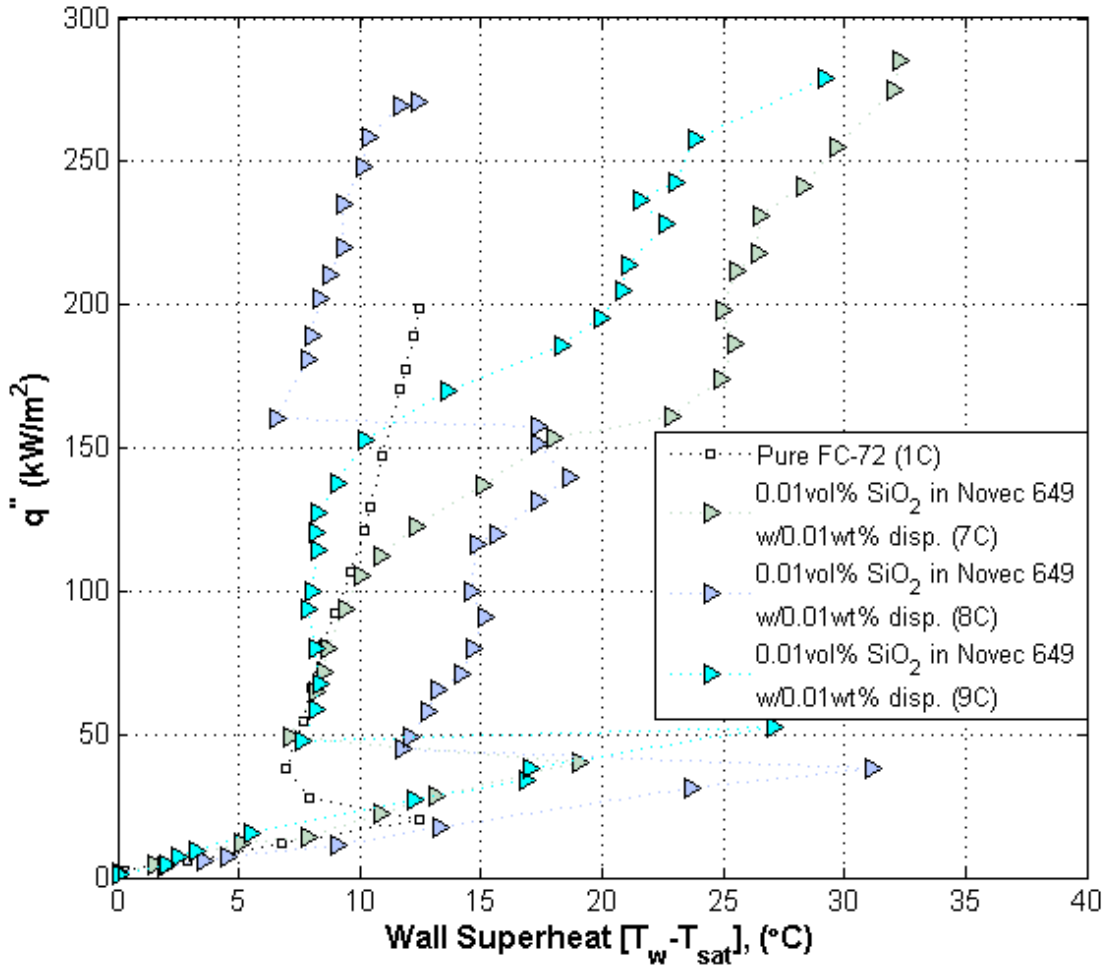

Figure 53: Boiling Curves for 0.01" Nickel Wires in 0.01vol% SiO_2/Novec 649 Dispersion with 0.01wt% Fluorinated Surfactant. There was significant scatter in the wall superheat (although the CHF value was consistent), with curves displaying unusual trends. In one case, the wall superheat falls rapidly at 150 kW/m^2, although this is likely an artificial occurrence.

7.3.5. Nickel Wire in Al/$C_2F_5C(O)CF(CF_3)_2$ Colloid

Boiling tests were conducted with 0.01" nickel wires in a 0.01vol% aluminum/Novec 649 dispersion (see section 6.2.2). No surfactant was added, considering that the particles dispersed well without it, and that the surfactant was found to degrade boiling heat transfer. Figure 54 shows boiling curves for this test case, and Figure 55 shows the effective heat transfer coefficient. As seen in the results, the aluminum nanoparticles have only a slight effect on the heat transfer coefficient, but enhance the CHF by over 40%. After boiling wires in the Al/Novec 649 dispersions, a dark gray deposit was visible on the wire, which could be easily wiped off. It is suspected that this deposit consists of the Al nanoparticles.

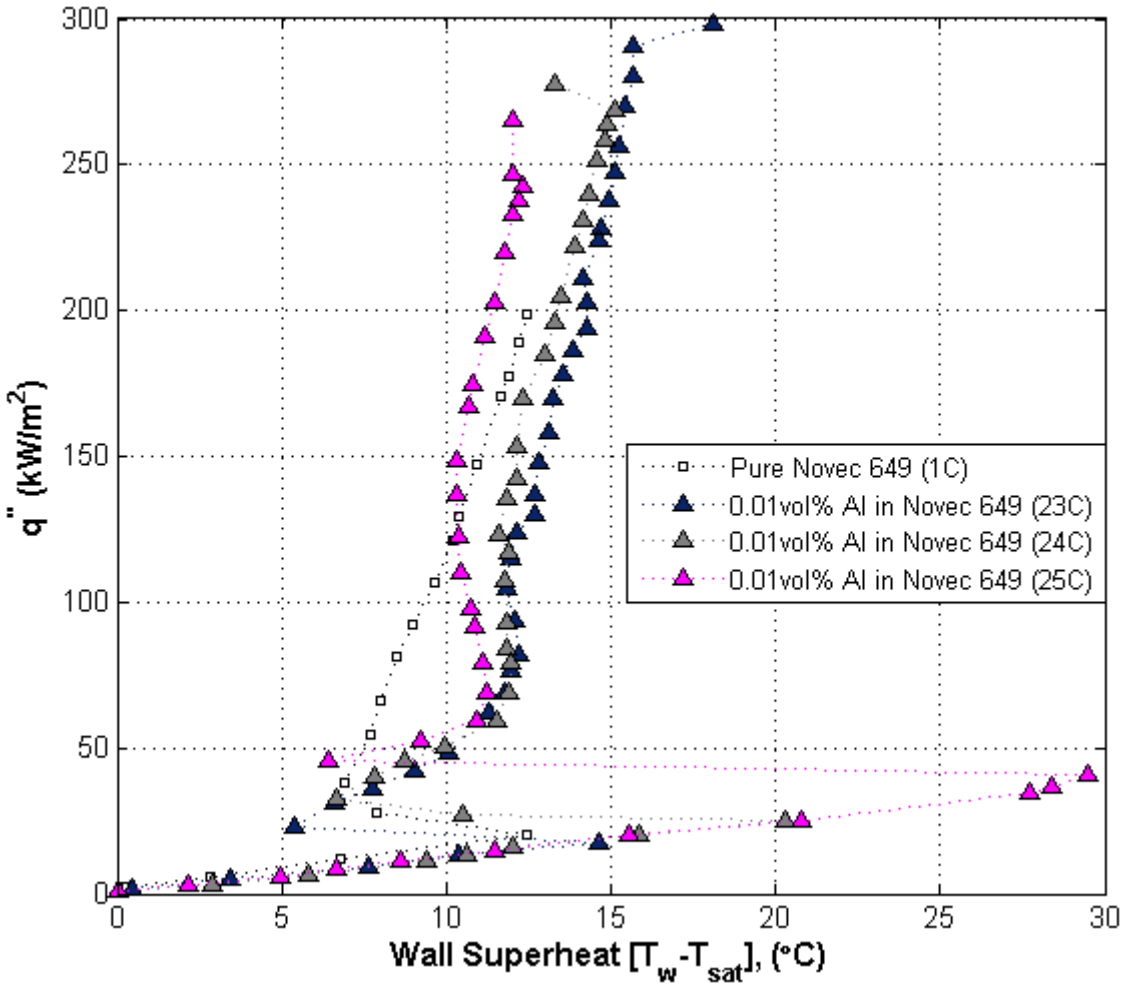

Figure 54: Boiling Curves for 0.01" Nickel Wires in a Al/Novec 649 Dispersion.

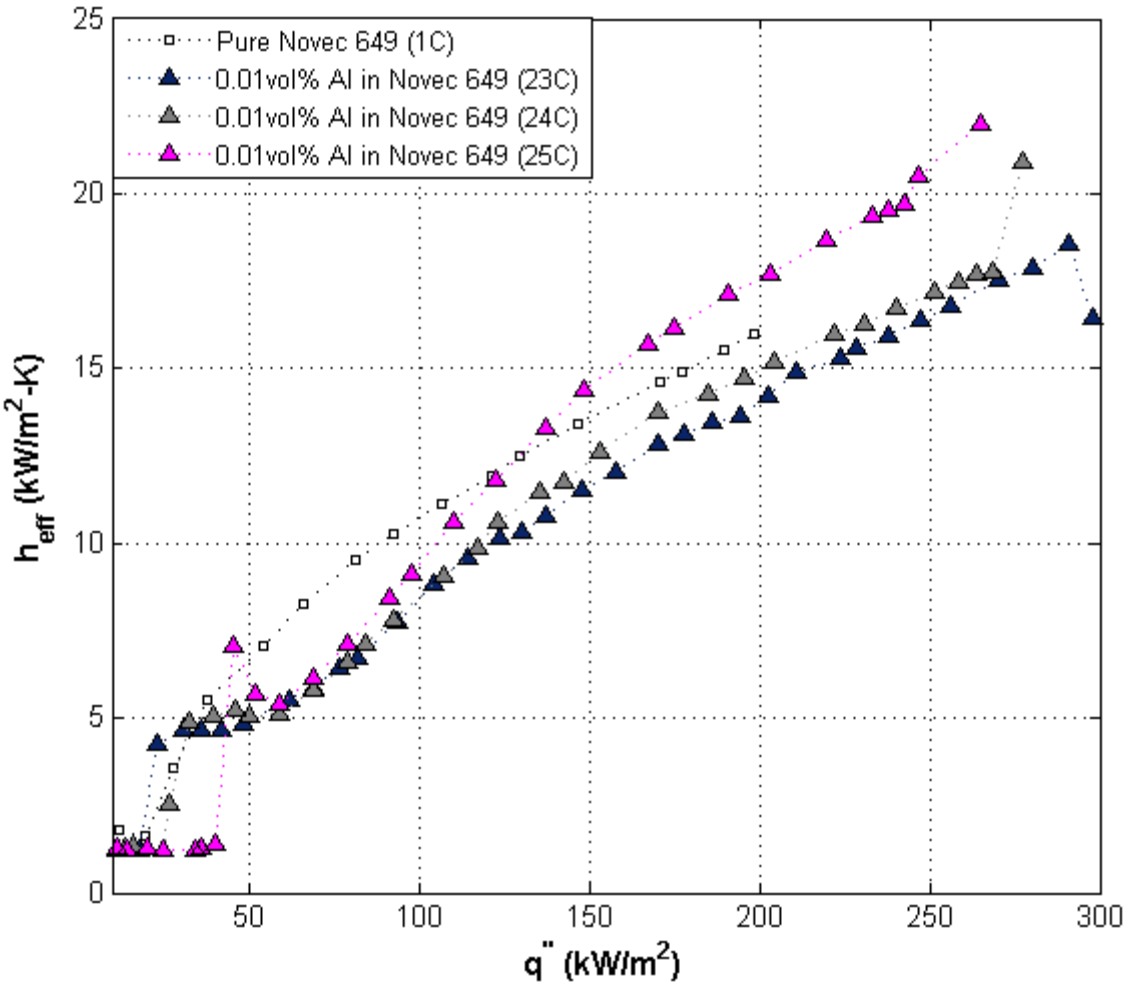

Figure 55: Effective Heat Transfer Coefficient Plotted Against Heat Flux for the Al/Novec 649 Dispersions.

8. THEORETICAL ASPECTS OF BOILING IN WELL-WETTING DIELECTRIC FLUIDS

8.1. Incipience of Boiling

The incipience of boiling for both Novec 649 and FC-72 occurs after a large temperature increase in the natural convection region, followed by a considerable drop upon activation of nucleation sites. This onset of nucleate boiling temperature overshoot is contrary to the classic wall superheat requirement calculated using the Young-Laplace and Clausius-Clapeyron equations,

$$T_w - T_{sat} = \frac{2\sigma T_{sat} v_{fg}}{h_{fg} r_c} \qquad (23)$$

if r_c is taken to be the radius of a typical microcavity on the surface. For low surface tension liquids, one would expect the superheat for activation to be lower than for high surface tension liquids such as water based on equation (23). Carey explains the importance of the radius of the vapor nucleus for the incipience of boiling, and that the radius of the vapor nucleus is not necessarily equivalent to the cavity radius, but rather strongly dependent on the contact angle [55]. For low contact angle (well-wetting) fluids, one may not assume that the radius of the vapor nucleus equals that of the cavity. The fluorinated ketone and perfluorocarbon investigated in this study are very well-wetting, resulting in partial or complete flooding of cavities. Anderson and Mudawar discuss this phenomenon for perfluorocarbons, noting that small heaters are even more susceptible to large incipience excursions. They explain that rapid activation patterns are more significant on small heaters since the surface area fraction of the heater affected by a single nucleation site is larger [92]. Marto and Lepere [93], among others, have observed similar trends for boiling incipience in fluorocarbons. Yin and Abdelmessih [94] observe the temperature overshoot phenomenon in the flow boiling of a fluorocarbon liquid. Bar-Cohen addresses the superheat excursion phenomenon in detail, also pointing out that enhanced surfaces typically do not alleviate the effect [95]. The temperature overshoot is cause for concern in two-phase electronics cooling systems, as it may result in device temperatures significantly exceeding steady-state operational temperatures.

Although not shown in the boiling curves, a hysteresis in the boiling curve was observed for both Novec 649 and FC-72 when the heat flux was reduced after operating in the nucleate boiling regime. As the heat flux was reduced below the level at which boiling incipience occurred, nucleation sites deactivated gradually, skipping the temperature overshoot seen initially. This is likely due to the entrapment of vapor in the nucleating cavities, leading to lower wall superheat requirements to maintain nucleation.

8.2. Critical Heat Flux

A review of relevant theories governing the critical heat flux is discussed in section 4.3.1. Unlike the case of boiling from the 0.01" nickel wires in de-ionized water, the hydrodynamic instability factor with the appropriate correction factor for a horizontal cylinder in the fluorinated ketone and FC-72 is applicable, since the critical bubble radius is much smaller than that for water. Using equation (9), one can determine that for saturated conditions at atmospheric pressure, the critical bubble radius is R_c=7.22x10^{-4} m for FC-72 and R_c=7.92x10^{-4} m for $C_2F_5C(O)CF(CF_3)_2$. From this, one determines that the characteristic length is R^*=0.18 for FC-72 and R^*=0.16 for the fluorinated ketone. This allows for application of Lienhard's prediction for small, horizontal cylinders, which is applicable for $0.15 \leq R^* < 1.2$. Therefore, we may apply Lienhard's finite body correction factor to the hydrodynamic instability theory, which, for small horizontal cylinders, is the following [96]:

$$\frac{q''_{CHF}}{q''_{CHF\ Zuber}} = \frac{0.94}{(R^*)^{1/4}} \qquad (24)$$

Using equation (17), and the saturated properties of each respective fluid, one finds that $q''_{CHF,Zuber}$=152 kW/m^2 for FC-72, and $q''_{CHF,Zuber}$=140 kW/m^2 for the fluorinated ketone. Therefore, the predicted CHF values using the correction factor are 224 kW/m^2 for FC-72, and 208 kW/m^2 for the fluorinated ketone, remarkably close to the experimental values obtained for the pure fluids.

However, the hydrodynamic model is unable to predict the 40% enhancement achieved by boiling in the dilute SiO_2 and aluminum Novec 649 dispersions. The more recent models,

covered in section 4.3.1, rely on the contact angle with the surface. However, the fluorinated ketone is essentially perfectly wetting, with a equilibrium contact angle of 0º on unaltered surfaces. Therefore, it is likely that another surface parameter is affecting CHF. Although effects of nanoparticles on fluid properties are expected to be negligible due to the dilute concentrations tested, they cannot be ruled out since fluid properties were not measured for every test case. Tuma has demonstrated enhancement in both the heat transfer coefficient and critical heat flux through the use of metallic microparticle coatings for both hydrofluoroethers [97] and Novec 649 [79]. Kim, Rainey, et al. have demonstrated that a microporous diamond coating significantly enhances the pool boiling heat transfer coefficient and the critical heat flux for FC-72 [8], attributing the increase in the nucleate boiling heat transfer coefficient to a higher nucleation site density imparted by the microporous coating. However, one must consider that these are microparticle coatings, and can be fairly thick. The diamond coating used by Kim consisted of 8-12 μm particles, and was about 18 μm thick. In addition, the coating used a binder agent, which could have, by itself, an effect on boiling heat transfer. Kim et al. claim that the enhancement is not due to an increase in surface area, but rather higher nucleation site density and bubble frequency, and that the postponement of CHF is due an increase in the convective heat transfer contribution or an increase in bubble vapor inertia [8].

The thicknesses of the SiO_2 and aluminum deposits on the 0.01" nickel wires investigated in this study were not measured. In a similar study in the same laboratory, Truong measured thicknesses of anywhere between 3 μm and 15 μm for SiO_2 nanoparticle deposits on a 0.381 mm stainless steel wire boiled in a 0.01vol% SiO_2 water-based nanofluid [98]. It is not unreasonable to expect coating thicknesses in this vicinity for deposits of SiO_2 on wires boiled in 0.01vol% SiO_2/Novec 649 dispersions. The advantage of thinner coatings is the ability to minimize the thermal resistance added by the particle layer. The thermal conductivity of a porous coating can be calculated by [99]:

$$\frac{k_{eff}}{k_f} = \left(\frac{k_s}{k_f} \right)^{0.280 - 0.757 \log(\varepsilon) - 0.057 \log(k_s / k_f)} \quad \textbf{; } \mathbf{0.2 < \varepsilon \leq 0.6} \qquad (25)$$

In boiling from our coatings, we would expect both liquid and vapor to be present. Figure 56 shows the expected thermal conductivity for porous coatings of SiO_2 and aluminum nanoparticles as a function of porosity, assuming that the void space is filled either entirely with vapor or entirely with liquid. Were the distribution of particle size accurately known, the porosity, ε, could be estimated in the same manner as it was for the thin-film coatings (see section 3.3.5). In Figure 57, the thermal resistance of the coating is estimated as a function of thickness, simply assuming the porosity to be ε=0.40.

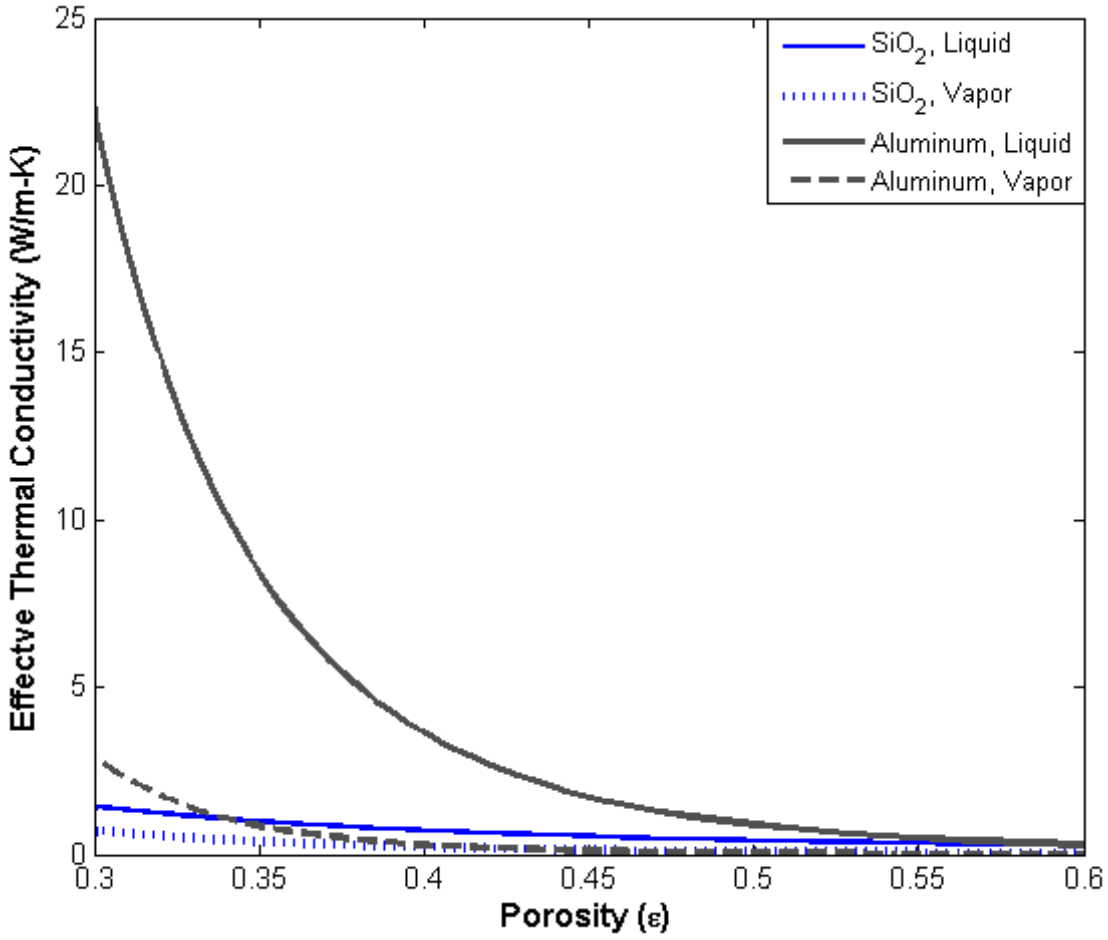

Figure 56: Effective Thermal Conductivity as a Function of Porosity for Aluminum and SiO_2 Coatings in Novec 649. Cases where the fluid is either in its liquid or vapor state are included. The aluminum is assumed to be unoxidized, and the silica is assumed to be in amorphous form.

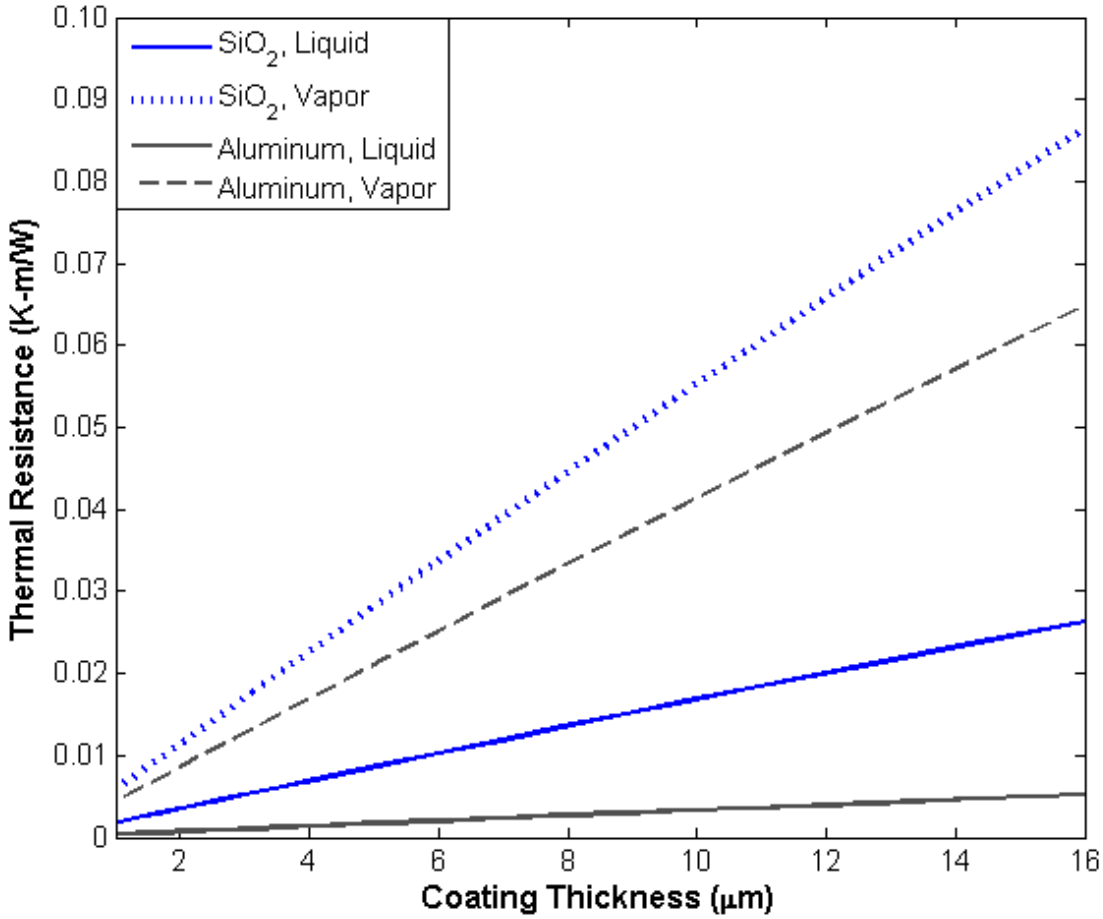

Figure 57: Predicted Thermal Resistance per Unit Length as a Function of Coating Thickness for Porous Coatings of Aluminum and SiO_2 on a 0.01" Nickel Wire in Novec 649. The porosity is assumed to be ε=0.4. Cases where the fluid is either in its liquid state or vapor state are provided. The aluminum is assumed to be unoxidized, and the silica is assumed to be in amorphous form.

It would appear that porosity effects are important, and in the case of well-wetting fluids, the likely explanation for enhancement in CHF. Polezhaev and Kovalev proposed the following semi-empirical formula for boiling from a uniform porous coating [100]:

$$q''_{CHF} = 0.52\varepsilon^{2.28} h_{fg} \left[\frac{2\sigma\rho_f\rho_g}{(\rho_f + \rho_g)d_{br}} \right]^{1/2} \quad (26)$$

where ε is the porosity of the coatings and d_{br} is the diameter of the bubble as it breaks through the coating. Hwang and Kaviany fit their experimental data to Polezhaev's prediction, and

determined that the breakthrough bubble diameter, d_{br}, does not change with particle size or other coating characteristics [7]. Therefore, Polezhaev's semi-empirical prediction would seem to indicate that coating thickness does not impact CHF, which does not agree with results in this work. Additionally, equation (26) cannot be applied to our reference cases, since the porosity for the bare surfaces is essentially zero. According to Liter and Kaviany, enhancement obtained with porous coatings is commonly attributed to effects of increased surface area, capillary induced assistance to liquid flow, creation of more nucleation sites, and/or influence on vapor escape paths created by the porous structures. Liter and Kaviany go on to say, "These effects are dependent on the fluid and solid thermophysical properties and geometrical coating parameters, such as coating thickness δ and pore size distribution. The exact relational dependence is not well understood and the extent of possible enhancement is not known" [101]. The data obtained in this study, both for thin-film coatings in water and porous deposits of nanoparticles in well-wetting fluids, appear to support this statement, with variations in thickness and other parameters appearing to have an effect. However, the study of porous coatings in the literature have primarily focused on *microporous* coatings and surfaces, whereas the thin-film coatings investigated in Section I and nanoparticle deposits investigated in this Section are *nanoporous* in nature, with pore sizes in the vicinity of 100 nm or less for thin film coatings (see section 3.3.4 and section 3.3.5). Pore sizes are likely similar for deposits of SiO_2 and aluminum particles from boiling deposition based off the original particle size. Nanoparticle coatings with pore sizes an order of magnitude smaller than microparticle coatings are likely to have different effects on bubble interaction and other mechanisms, so data and correlations developed for microporous coatings should be applied to nanoporous coatings with caution.

>>>>>>>>>>>>>>>>>>>>>>>>>>>>>>>>>>>>>>><<<<<<<<<<<<<<<<<<<<<<<<<<<<<<<<<<<<<<<

9. CONCLUSION

This work has explored two general approaches to nanoparticle-based surface modification in two separate classes of fluids, and shown that enhancement in the pool boiling critical heat flux and nucleate boiling heat transfer coefficient is possible with both methods. Nanoscale modification of surface features for boiling heat transfer allows for precise control over parameters which affect nucleate boiling and CHF, such as wettability. These surfaces, which have been carefully engineered using nanoparticles, are optimized to enhance two-phase heat transfer and CHF.

Although the two methods for depositing nanoparticles on surfaces are not directly comparable, each method offers certain advantages over the other. Constructing nanoparticle coatings on boiling surfaces using the layer-by-layer assembly method allows for precise control of coating thickness, and to some degree control over porosity and surface texture. Additionally, the layer-by-layer assembly method allows for additional treatments, such as chemical vapor deposition of fluorosilane, which can drastically alter surface wettability without affecting other parameters. Lastly, the layer-by-layer assembly method provides a means of applying nanoparticle coatings to surfaces which are quite durable. Through boiling deposition of nanoparticles, on the other hand, it is more difficult to control coating thickness and ensure adequate durability and uniformity.

Nonetheless, boiling deposition offers distinct practical advantages over the LbL method for applications in many engineering systems, including direct in situ deposition of nanoparticles. In many systems, additional treatments associated with the LbL method, such as calcination at 550 ºC, may not be practical, thereby giving advantage to boiling deposition methods. For applications involving immersion cooling of electronic devices, immersing dies in low pH aqueous solutions and calcinating at high temperatures would likely result in damage, making boiling deposition of nanoparticles a more practical method. Additionally, continuous boiling in nanofluids provides a regenerative coating should particles scale off.

The primary findings of the experimental studies included in this work are summarized as follows:

Nanoparticle Thin-film Coatings for Pool Boiling Heat Transfer Enhancement

- Nanoparticle thin-film coatings, applied using the layer-by-layer deposition method, display up to 100% enhancement in the pool boiling critical heat flux.
- Nanoparticle thin-film coatings treated with fluorosilane display over 100% enhancement in the nucleate boiling heat transfer coefficient.
- Film thickness affects CHF, with thicker films (up to 40-bilayers) leading to greater enhancement.
- Both surface texture and chemical constituency can be altered drastically with the application of nanoparticle thin-films, influencing wettability, and in turn, nucleate boiling heat transfer and CHF.
- The advancing contact angle appears to be the primary parameter affecting the nucleate boiling heat transfer coefficient, with higher advancing contact angles leading to improved nucleate boiling heat transfer due to its impact on the size of the vapor nucleus in boiling cavities.
- The receding contact angle appears to be an important parameter influencing CHF, with low receding contact angles leading to higher CHF values.
- The optimal surface for pool boiling heat transfer is one which displays a large contact angle hysteresis, with high advancing contact angle to enhance nucleate boiling heat transfer and low receding contact angle to enhance CHF.

Nanoparticle-Based Enhancement of Pool Boiling Heat Transfer in Low Global Warming Potential Dielectric Fluids

- The fluorinated ketone $C_2F_5C(O)CF(CF_3)_2$, sold commercially as Novec 649, has comparable pool boiling heat transfer performance to that of perfluorohexane (FC-72), and may be a viable environmentally friendly alternative in two-phase electronics cooling applications.
- The effect of dispersants on boiling heat transfer can be significant, even when used at low concentrations. Therefore, the effect of dispersants must be considered when preparing colloidal dispersions for two-phase heat transfer applications.
- Dilute dispersions of SiO_2 or aluminum nanoparticles display up to 40% enhancement in the critical heat flux for well-wetting dielectric fluids. The enhancement mechanism likely relates to the boiling deposition of particles on the heater surface, as has been shown previously in other water-based nanofluid experiments.
- The effective thermal conductivity of porous coatings is typically much less than that of the bulk material. Thick coatings of porous particles can lead to high thermal resistances on heater surfaces, so it is therefore desirable to reduce coating thickness.
- The nucleate boiling heat transfer coefficient for well-wetting dielectric fluids may either be degraded, enhanced, or unchanged with the addition of small amounts of SiO_2 or aluminum nanoparticles, depending on the concentration of particles and dispersant.

General Implications for Pool Boiling Heat Transfer

Although wettability appears to be an important parameter influencing CHF, it is not entirely adequate in predicting or describing CHF enhancement, especially with complex surfaces or with well-wetting fluids. Specifically, wettability alone fails in explaining CHF enhancement achieved in an already perfectly wetting fluid, or CHF enhancement achieved with increases in the thickness of a porous film where no surface wettability change is observed. Although surface structure and chemical constituency are closely related to wettability, there may be additional effects that wettability does not account for. In particular, nanoporous coatings need to be studied further, with an emphasis on the role of porosity and pore size in boiling heat transfer.

REFERENCES

[1] Buongiorno, J., L.W. Hu, S.J. Kim, R. Hannink, B. Truong, and E. Forrest. "Nanofluids for Enhanced Economics and Safety of Nuclear Reactors: An Evaluation of the Potential Features, Issues, and Research Gaps." *Nuclear Technology*, 162 (2008): 80-91.

[2] Choi, S. "Enhancing Thermal Conductivity of Fluids with Nanoparticles." In: D.A. Signiner, D.A. and H.P. Wang (Eds.). *Developments and Applications of Non-Newtonian Flows*. ASME, FED-Vol. 231/MD-Vol. 66, 1995, pp. 99-105.

[3] Kim, S.J., I.C. Bang, J. Buongiorno, and L.W. Hu. "Surface Wettability Change During Pool Boiling of Nanofluids and Its Effect on Critical Heat Flux." *International Journal of Heat and Mass Transfer* 50 (2007): 4105-116.

[4] Kim, S.J., I.C. Bang, J. Buongiorno, and L.W. Hu. "Effects of Nanoparticle Deposition on Surface Wettability Influencing Boiling Heat Transfer in Nanofluids." *Applied Physics Letters*, 89 (2006).

[5] Berenson, P.J. "Experiments on Pool-Boiling Heat Transfer." *International Journal of Heat and Mass Transfer*, 5 (1962): 985-999.

[6] Webb, R.L. "The Evolution of Enhanced Surface Geometries for Nucleate Boiling." *Heat Transfer Engineering*, 2.3-4 (1981).

[7] Hwang, G.S. and M. Kaviany. "Critical Heat Flux in Thin, Uniform Particle Coatings." *International Journal of Heat and Mass Transfer*, 49 (2006): 844-849.

[8] Kim, J.H., K.N. Rainey, S.M. You, and J.Y. Pak. "Mechanism of Nucleate Boiling Heat Transfer Enhancement From Microporous Surfaces in Saturated FC-72." *Journal of Heat Transfer*, Transactions of the ASME, 124 (2002).

[9] Iler, R.K. "Multilayers of Colloidal Particles." *Journal of Colloid and Interface Science*, 21 (1966): 569-594.

[10] Decher, G. and J.D. Hong. *Makromol. Chem. Macromol. Symp.*, 46, (1991): 321.

[11] Lee, D., M.F. Rubner, and R.E. Cohen. "All-Nanoparticle Thin-Film Coatings." *Nano Letters*, 6 (2006): 2305-312.

[12] Lee, D., D. Omolade, R.E. Cohen, and M.F. Rubner. "pH-Dependent Structure and Properties of TiO2/SiO2 Nanoparticle Multilayer Thin Films." *Chemical Materials*, 19 (2007): 1427-433.

[13] Lee, D., Z. Gemici, M.F. Rubner, and R.E. Cohen. "Multilayers of Oppositely Charged SiO2 Nanoparticles: Effect of Surface Charge on Multilayer Assembly." *Langmuir*, 23 (2007): 8833-837.

[14] Cebeci, F., Z. Wu, L. Zhai, R.E. Cohen, and M.F. Rubner. "Nanoporosity-Driven Superhydrophilicity: A Means to Create Multifunctional Antifogging Coatings." *Langmuir*, 22 (2006): 2856-862.

[15] Bravo, J., L. Zhai, Z. Wu, R.E. Cohen, and M.F. Rubner. "Transparent Superhydrophobic Films Based on Silica Nanoparticles." *Langmuir*, 23 (2007): 7293-7298.

[16] Zhai, L., M. Berg, F. Cebeci, Y. Kim, J.M. Milwid, M.F. Rubner, and R.E. Cohen. "Patterned Superhydrophobic Surfaces: Toward a Synthetic Mimic of the Namib Desert Beetle." *Nano Letters*, 6 (2006): 1213-1217.

[17] Zhai, L., F. Cebeci, R.E. Cohen, and M.F. Rubner. "Stable Superhydrophobic Coatings from Polyelectrolyte Multilayers." *Nano Letters*, 4 (2004): 1349-1353.

[18] Material Safetey Data Sheet, "1H,1H,2H,2H-PerfluorodecyltriethoxysilaneFluorosilane." CAS# 101947-16-4. Updated June, 2008.

[19] Nukiyama, S. "The Maximum and Minimum Values of the Heat Q Transmitted From Metal to Boiling Water Under Atmospheric Pressure." *Journal Japan Soc. Engrs*, 37 (1934): 367-374. Reprinted *International Journal of Heat and Mass Transfer*, 9 (1966): 1419-1433.

[20] Kwang, T.H., H. Imadojemu, R.L. Webb. "Effects of Oxidation and Surface Roughness on Contact Angle." *Experimental Thermal and Fluid Science*, 8 (1994): 279-285.

[21] Theofanous, T.G., T.N. Dinh, J.P. Tu, and A.T. Dinh. "The Boiling Crisis Phenomenon Part II: Dryout Dynamics and Burnout." *Experimental Thermal and Fluid Science*, 26 (2002): 793-810.

[22] Westwater, J.W. "Boiling of Liquids." *Advances in Chemical Engineering Volume 1*, Thomas B. Drew and John W. Hoopes, Jr. Eds. Academic Press, 1963. p.64.

[23] Van Stralen, S.J.D and W.M. Sluyter. "Investigations on the Critical Heat Flux of Pure Liquids and Mixtures Under Various Conditions." *International Journal of Heat and Mass Transfer*, 12 (1969): 1353-1384.

[24] Davis, J.R. *ASM Specialty Handbook: Nickel, Cobalt, and Their Alloys*. ASM International, 2000. p.127.

[25] Kutz, M. *Handbook of Materials Selection*, 7th Ed. John Wiley and Sons, 2002. p.248.

[26] Schweitzer, P.A. *Corrosion Engineering Handbook: Atmospheric and Media Corrosion of Metals*, 2nd Ed. CRC Press, 2007. pp.237-242.

[27] Stansbury, E.E. and R.A. Buchanan. *Fundamentals of Electrochemical Corrosion*. ASM International, 2000. p.72.

[28] Holman, J.P. *Experimental Methods for Engineers*. McGraw-Hill, 2001. pp.48-62

[29] Lide, D.R., Ed. "Thermal and Physical Properties of Pure Metals." *Handbook of Chemistry and Physics*, 89th Edition. Section 12, p. 12-196.

[30] Incropera, F.P., D.P. DeWitt, T.L. Bergman, and A.S. Lavine. *Fundamentals of Heat and Mass Transfer*, 6th Ed. John Wiley & Sons, 2007. p.261.

[31] Buch, A. *Pure Metals Properties: A Scientific Technical Handbook*. ASM Intl., 1999. p.16.

[32] Coleman, H.W. and W.G. Steele. *Experimentation and Uncertainty Analysis for Engineers*, 2nd Ed. John Wiley & Sons, 1999. pp.210-212.

[33] Peirce, B. "Criterion for the Rejection of Doubtful Observations." *The Astronomical Journal*, No. 45, Vol. 2 (1852): 161-163.

[34] Ross, S.M. "Peirce's Criterion for the Elimination of Suspect Experimental Data." *Journal of Engineering* Technology (Fall 2003).

[35] Kandlikar, S.G. "Critical Heat Flux in Subcooled Flow Boiling- An Assessment of Current Understanding and Future Directions for Research." *Multiphase Science and Technology*, 13 (2001): 207-232.

[36] Crowe, C.T. *Multiphase Flow Handbook*. CRC Press, 2006. p.3-27.

[37] Lienhard IV, J.H. and J.H. Lienhard V. *A Heat Transfer Textbook*. Phlogiston Press, 2006. pp.481-485.

[38] Sun, K.H. and J.H. Lienhard. "The Peak Pool Boiling Heat Flux on Horizontal Wires." *International Journal of Heat and Mass Transfer*, 13 (1970): 1425-1439.

[39] Bakhru, N. and J.H. Lienhard. "Boiling from Small Cylinders." *International Journal of Heat and Mass Transfer*, 15 (1972): 2011-2025.

[40] Hong, Y.S., S.M. You, and J.P. O'connor. "Critical Heat Flux Mechanism on Small Cylinders." 6th International Symposium on Transport Phenomena in Thermal Engineering, Seoul, South Korea, 1993.

[41] Morrison, I.D. and S. Ross. *Colloidal Dispersions*. John Wiley and Sons, 2002. p.7

[42] "Uniform Silica Microspheres." Technical Data Sheet 635. Polysciences, Inc., 2008.

[43] "Ludox TM-40 Colloidal Silica Specification Sheet." Sigma Aldrich. Available: http://www.sigmaaldrich.com/catalog/DataSheetPage.do?brandKey=ALDRICH&symbol=420786.

[44] "Dynamic Contact Angles." KSV Instruments, Available: http://www.ksvltd.com/content/index/keydca. KSV Instruments Ltd., 2009.

[45] Starov, V.M., M.G. Velarde, and C.J. Radke. Wetting and Spreading Dynamics. Surfactant Science Series, Vol. 138. CRC Press, 2007.

[46] Tadmor, Rafael. "Line Energy and the Relation Between Advancing, Receding, and Young Contact Angles." *Langmuir*, 20 (2004): 7659-7664.

[47] Wang, Ying, Y. Mo, M. Zhu, and M. Bai. "Wettability of Metal Coatings with Biomimic Textures." *Surface and Coatings Technology*, 203 (2008): 137-141.

[48] Wang, R., L. Cong, and M. Kido. "Effect of the Wettability of Metal Surfaces by Micro-Pure Water by Means of Atomic Force Microscopy." *Applied Surface Science* 191 (2002): 74-84.

[49] Tompkins, H.G. and E.A. Irene, Eds. *Hanbook of Ellipsometry*. William Andrew Publishing, 2005. p.569.

[50] Scott, G.D. "Packing of Spheres." *Nature*, 188 (1960): 908-909.

[51] Bezrukov, A., D. Stoyan, and M. Bargieł. "Spatial Statistics for Simulated Packings of Spheres." *Image Anal Stereol*, 20 (2001): 203-206.

[52] Wenzel, R.N. "Resistance of Solid Surfaces to Wetting by Water." *Industrial and Engineering Chemistry* 28 (1936): 988-94.

[53] Aronov, D., G. Roseman, and Z. Barkay. "Wettability of Modified Silicon Dioxide Surface Using Environmental Scanning Electron Microscopy." *Journal of Applied Physics*, 101 (2007).

[54] Bernardin, J.D., I. Mudawar, Christopher B. Walsh, and Elias I. Franses. "Contact Angle Temperature Dependence for Water Droplets on Practical Aluminum Surfaces." *International Journal of Heat and Mass Transfer*, 40 (1997): 1017-1033.

[55] Carey, V.P. Liquid-Vapor Phase-Change Phenomena. Taylor & Francis Group, 2007. pp.210-226.

[56] Young, R.K. and R.L. Hummel. "Improved Nucleate Boiling Heat Transfer." *Chemical Engineering Progress*, 60 (1964): 53–58.

[57] Bankoff, S.G. "Entrapment of a Gas in the Spreading of a Liquid Over a Rough Surface." *A.I.Ch.E. Journal*, 4 (1958): 24-26.

[58] Jones, S.F., G.M. Evans, and K.P. Galvin. "Bubble Nucleation from Gas Cavities- A Review." *Advances in Colloid and Interface Science*, 80 (1999): 27-50.

[59] Eddington, R.I. and D.B.R. Kenning. "The Effect of Contact Angle on Bubble Nucleation." *International Journal of Heat and Mass Transfer*, 22 (1979): 1231-1236.

[60] Wang, C.H., and V.K. Dhir. "Effect of Surface Wettability on Active Nucleation Site Density During Pool Boiling of Water on a Vertical Surface." *Journal of Heat Transfer*, 115 (1993): 659-69.

[61] Zuber, N. "Hydrodynamic Aspects of Boiling Heat Transfer." AECU-4439, 1959.

[62] Kutateladze, S.S. "On the Transition to Film Boiling Under Natural Convection." *Kotloturbostroenie*, No. 3 (1948): 10-12.

[63] Haramura, Y., Y. Katto. "A New Hydrodynamic Model of CHF Applicable Widely to Both Pool and Forced Convection Boiling on Submerged Bodies in Saturated Liquids." *International Journal of Heat and Mass Transfer*, 26 (1983) 389-399.

[64] Sadasivan, P., P.R. Chappidi, C. Unal, R.A. Nelson. "Possible Mechanisms of Macrolayer Formation." *Pool and External Flow Boiling*, ASME (1992): 135.

[65] Theofanous, T.G., T.N. Dinh. "High Heat Flux Boiling and Burnout as Microphysical Phenomena: Mounting Evidence and Opportunities." *Multiphase Science and Technology*, 18 (2006): 1-26.

[66] Kandlikar, S.G., 2001, "A Theoretical Model to Predict Pool Boiling CHF Incorporating Effects of Contact Angle and Orientation." *Journal of Heat Transfer*, 123, (2001): 1071-1079.

[67] Kandlikar, S.G. and Mark E. Steinke. "Contact Angles and Interface Behavior During Rapid Evaporation of Liquid on a Heated Surface." *International Journal of Heat and Mass Transfer*, 45 (2002): 3771-3780.

[68] Valenzuela, J., T. Jasinski, and Z. Sheikh. "Liquid Cooling for High-Power Electronics." *Power Electronics Technology*, February 2005: 50-56.

[69] Bergles, A.E., N. Bakhru, and J.W. Shires, Jr. "Cooling of High-Power-Density Computer Components." MIT Heat Transfer Laboratory Report No. DSR 70712-60. Cambridge, Massachusetts, Nov. 1968.

[70] Chu, R.C. "The Challenges of Electronic Cooling: Past, Current and Future." *Journal of Electronic Packaging*, 126 (2004): 491-500.

[71] Nayar, C.V., S.M Islam, and H. Sharma. "Power Electronics for Renewable Energy Sources." *Power Electronics Handbook*. M. H. Rashid, Ed. Academic Press, 2001. pp.812-813. pp.539-562.

[72] Perreault, D.J., K.K. Afridi, and I.A. Khan. "Automotive Application of Power Electronics." *Power Electronics Handbook*. M. H. Rashid, Ed. Academic Press, 2001. pp.812-813.

[73] Ozone Secretariat, United Nations Environment Programme. *The Montreal Protocol on Substances that Deplete the Ozone Layer- As adjusted or amended in: London 1990, Copenhagen 1992, Vienna 1995, Montreal 1997, Beijing 1999*. UNON, 2000.

[74] Campbell, J.B., L.M. Tolbert, C.W. Ayers, B. Ozpineci, and K.T. Lowe. "Two-Phase Cooling Method Using R134a Refrigerant to Cool Power Electronic Devices." Applied Power Electronics Conference and Exposition 2005 (APEC 2005). *Proceedings of 20th Annual IEEE*, 1 (2005): 141-147.

[75] Committee on Radiative Forcing Effects on Climate. *Radiative Forcing of Climate Change: Expanding the Concept and Addressing Uncertainties*. National Academies Press, 2005. pp.12-27.

[76] Houghton, J.T., N.B. Harris, and L.G. Filho, Eds. *Climate Change 1995: Contribution of Working Group I to the Second Assessment Report of the Intergovernmental Panel on Climate Change*. Cambridge University Press, 1996. pp. 21-23

[77] Ravishankara, A.R., S. Solomon, A.A. Turnipseed, and R.F. Warren. "Atmospheric Lifetimes of Long-Lived Halogenated Species." *Science*, 259 (1993): 194-199.

[78] Climate Change Secretariat, United Nations Framework Convention on Climate Change (UNFCCC). *Kyoto Protocol Reference Manual: On Accounting of Emissions and Assigned Amount*. UNFCC, 2008.

[79] Tuma, P.E. "Fluoroketone $C_2F_5C(O)CF(CF_3)_2$ as a Heat Transfer Fluid for Passive and Pumped 2-Phase Applications." *Proceedings of the 24th SEMI-THERM Symposium* (2008): 173-179.

[80] Dobiáš, B., X. Qiu, and W. von Rybinski. *Solid-Liquid Dispersions*. Marcel Dekker, 1999. pp. 209-227.

[81] Morrison, I.D. and S. Ross. *Colloidal Dispersions*. John Wiley and Sons, 2002. p.396.

[82] Dobiáš, B., X. Qiu, and W. von Rybinski. *Solid-Liquid Dispersions*. Marcel Dekker, 1999. pp.246-254.

[83] Morrison, I.D. and S. Ross. *Colloidal Dispersions*. John Wiley and Sons, 2002. p.398-400.

[84] Nelson, R.D. "Dispersing Powders in Liquids." *Handbook of Powder Technology*, 7. J.C. Willuiams and T. Allen, Eds. Elsevier, 1988. pp.211-214.

[85] Kissa, E. *Fluorinated Surfactants and Repellants*. Marcel Dekker, 2001. p.358.

[86] "Nano Aluminum / Aluminum Powder." NanoTechnology Base. Available: http://eng.ntbase.net/eng/business/11_aluminium_03.asp. NTbase, 2009.

[87] "KD2 Pro Thermal Properties Analyzer- Operator's Manual Version 6." Decagon Devices Inc., 2008.

[88] Liu, Z.W., W.W. Lin, and D.J. Lee. "Pool Boiling of FC-72 and HFE-7100." *Journal of Heat Transfer*, 123 (2001): 399-400.

[89] Wu, W.T., Y.M. Yang, and J.R. Maa. "Nucleate Pool Boiling Enhancement by Means of Surfactant Additives." *Experimental Thermal and Fluid Science*, 18 (1998): 195-209.

[90] Jeong, H. Jeong, M.D. Sarwar, and S.H. Chang. "Flow Boiling CHF Enhancement with Surfactant Dolutions Under Atmospheric Pressure." *International Journal of Heat and Mass Transfer*, 51 (2008): 1913-1919.

[91] Kissa, E. *Fluorinated Surfactants and Repellants*. Marcel Dekker, 2001. p.111.

[92] Anderson, T.M. and I. Mudawar. "Microelectronic Cooling by Enhanced Pool Boiling of a Dielectric Fluorocarbon Liquid." *Journal of Heat Transfer*, 111 (1989): 752-759.

[93] Marto, P.J. and L.V.J. Lepere. "Pool Boiling Heat Transfer from Enhanced Surfaces to Dielectric Fluids." *Journal of Heat Transfer*, 104 (1982): 292-299.

[94] Yin, S.T. and A.H. Abdelmessih. "Prediction of Incipient Flow Boiling from a Uniformly Heated Surface." *A.I.Ch.E. Symp.*, Ser. 164, 73 (1977): 236-243.

[95] Bar-Cohen, A. "Fundamentals of Nucleate Pool Boiling of Highly-Wetting Dielectric Liquids." *Cooling of Electronic Systems*. S. Kakaç, H. Yüncü, and K. Hijikata, Eds. Kluwer Academic Publishers, 1994. pp.415-455.

[96] Collier, J.G. and J.R. Thome. *Convective Boiling and Condensation*, 3rd Ed. Clarendon Press, 1994. p.165.

[97] Tuma, P.E. "Evaporator/Boiler Design for Thermosyphons Utilizing Segregated Hydrofluoroether Working Fluids." *Proceedings of the 22nd IEEE SEMI-THERM Symposium* (2006): 69-77.

[98] Truong, B. "Determination of Pool Boiling Critical Heat Flux Enhancement in Nanofluids." *Proceedings of the ASME International Mechanical Engineering Congress and Exposition* (2007).

[99] Kaviany, M. *Principles of Heat Transfer in Porous Media*, 2nd Ed. Springer, 1995. p.144.

[100] Polezhaev, Y.V. and S.A. Kovalev. "Modelling Heat Transfer with Boiling on Porous Structures." *Thermal Engineering*, 37 (1990): 617-620.

[101] Liter, S.G. and Massoud Kaviany. "Pool Boiling CHF Enhancement by Modulated Porous Layer Coating." *International Journal of Heat and Mass Transfer*, 44 (2001): 4287-4311.